

Optical Effects and Applications Associated with Photonic Crystal Materials

Alex Lonergan¹ and Colm O'Dwyer^{1,2,3,4*}

¹*School of Chemistry, University College Cork, Cork, T12 YN60, Ireland*

²*Micro-Nano Systems Centre, Tyndall National Institute, Lee Maltings, Cork, T12 R5CP, Ireland*

³*AMBER@CRANN, Trinity College Dublin, Dublin 2, Ireland*

⁴*Environmental Research Institute, University College Cork, Lee Road, Cork T23 XE10, Ireland*

Abstract

The ability to selectively redirect specific wavelengths of light has attracted a lot attention for photonic crystal materials. Presently, there is a wealth of research relating to the fabrication and application of photonic crystal materials. There a number of structures which fall into the category of a photonic crystal; 1D, 2D and 3D ordered structures can qualify as a photonic crystal, provided there exists ordered repeating lattices of dielectric material with a sufficient refractive index contrast. The optical responses of these structures, namely the associated photonic bandgap or stopband, are of particular interest for any application involving light. The sensitivity of the photonic bandgap to changes in lattice size or refractive index composition creates the possibility for accurate optical sensors. Optical phenomena involving reduced group velocity at wavelengths on the edge of the photonic bandgap are commonly exploited for photocatalytic applications. The inherent reflectivity of the photonic bandgap has created applications in optical waveguides or as solar cell reflector layers. There are countless examples of research attempting to exploit these facets of photonic crystal behavior for improved material design. Here, the role of photonic crystals is reviewed across a wide a variety of disciplines; cataloguing the ways in which these structures have enhanced specific applications. Particular emphasis is placed on providing an understanding of the specific function of the tunable optical response in photonic crystals in relation to their application.

1 Introduction: Nanostructure, Biomimetics and Structural Coloration

Nanostructures are widely used in materials research to optimise the performance or functional characteristics associated with a particular material in a system. Nanostructures used in microelectronics led to the development of nanoelectronics with more components per chip, improved performances, lower costs and power consumption¹. Many other fields of research have also exploited the structural properties of nanomaterials for enhanced material performances in areas such as photocatalysis², energy storage³ and biomedicine⁴. A common advantage of nanomaterial structures is often the increased specific surface of the material compared to bulk counterparts, creating favourable geometries or increased surface reactions in many systems^{2 5 6}. Precise control over nanostructure feature sizes and geometries allows certain material responses to surface plasmon, electrical and optical properties to be governed to some extent by the existence of the nanoscale order^{7 8 9}.

The optical properties of a structure are particularly susceptible to variation based on the particular ordering involved in the composition of the nanostructure. The symmetry, spacing and type of repeating structure are all important considerations for the optical appearance of the material. Nature provides many different and vivid examples of nanostructured materials and the interesting optical phenomena associated with structural order. Structural color is present throughout the natural world, where the colors associated with bird feathers, butterfly wings and beetle shells arise from nanostructured materials as opposed to varying material composition or dyes^{10 11 12}. Studying the lattices and finer structure of these materials provides an insight into the appearance and striking coloration associated with naturally occurring nanostructured materials which can exist as one-, two- or three- dimensional repeating structures¹³. The variation in structural color, even between similar species, can be understood from the different types of nanostructured order present in the material¹⁴. Iridescence observations, where certain viewpoints or angles appear to influence a material's color appearance, can also be explained for materials featuring structural coloration through consideration of the light interaction and diffraction effects in these ordered materials^{15 16}.

In addition to structural color, certain naturally occurring phenomena can be understood by direct observation of the nanostructure associated with the material. One prominent example is the lotus effect¹⁷.

The specific spacing of the material nanostructure heavily influences the wettability of many types of plant leaves¹⁸ and other biological structures^{19 20}. In the case of lotus leaves, a strong structural hydrophobicity is achieved through the nanostructure of the leaf in combination with the hydrophobic properties of the waxes on the surface of the leaf²¹. Figure 1 displays several examples of prominent nanostructured materials present in the natural world. The hydrophobicity of the lotus leaf is shown from the high water contact angle of a droplet sitting atop a lotus leaf surface in Fig. 1 (b). Structural coloration is demonstrated via the vibrant colors and iridescence effects shown for butterfly wings, peacock feathers, beetle shells, sea mouse spines, opal gemstones and begonia plant leaves. Microscopy examples of the fine structure of materials are displayed alongside images showing natural structural order. Figure 1 showcases just a sampling of the many instances of structural color occurring in the natural world.

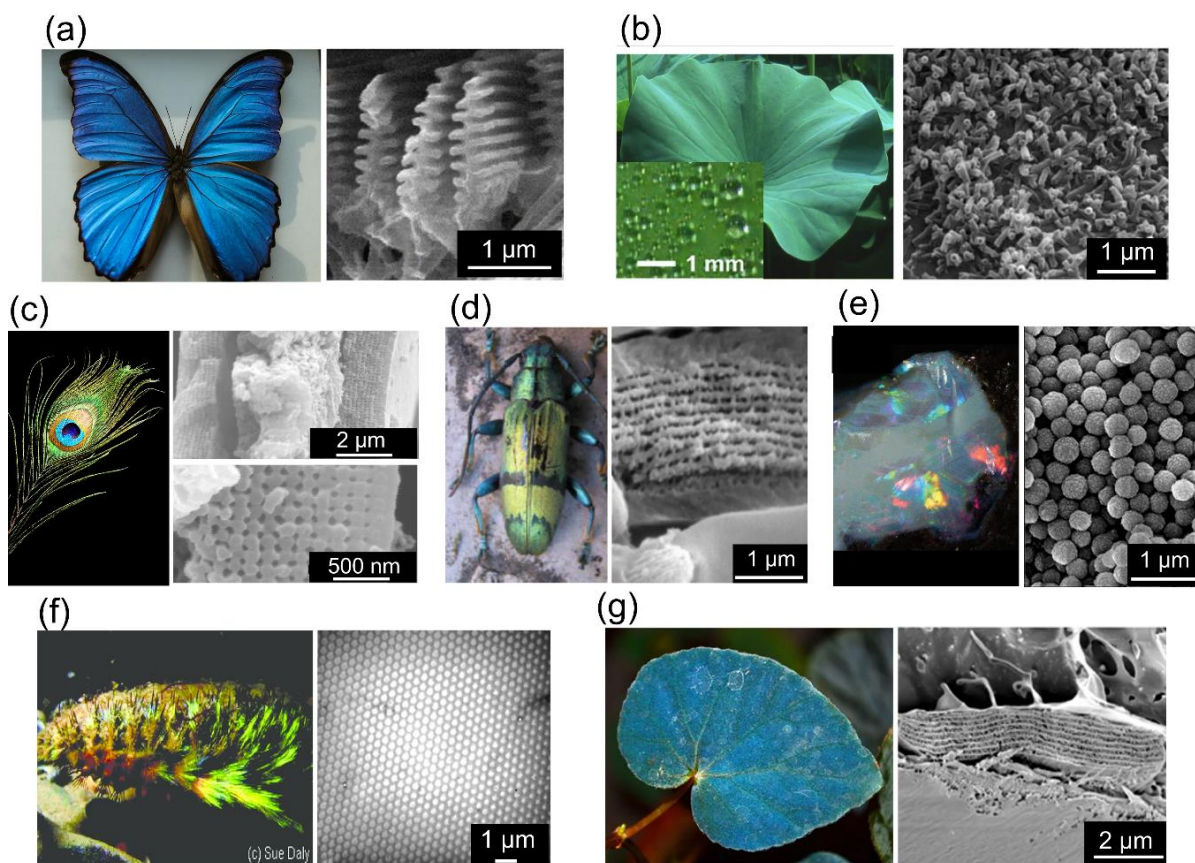


Fig. 1 Structural colors and phenomena arising in nature are attributed to micro and nanoscale features of the surface. (a) Blue wings of the morpho didius butterfly wing²² with a ridged structural order²³. Reproduced from ref.²². Copyright 2018, Nature. Adapted from ref.²³. Copyright IOP Publishing. (b) Hydrophobic properties of the lotus leaf²⁴ attributed to the waxy tubule structures on the upper leaf surface²⁵. Adapted from ref.²⁴. Copyright 2014, MDPI. Adapted from ref.²⁵. Copyright 2011, Beilstein Institute for the Advancement of Chemical Sciences. (c) Bright colors of the eye of peacock feathers are associated with mealmn rods connected by keratin²⁶. Adapted from ref.²⁶. Copyright 2003, United States National Academy of Sciences. (d) Green shell of the Tmesisternus isabellae beetle composed of scales with alternating dielectric layers²⁷. Adapted from ref.²⁷. Copyright 2009, OPTICA. (e) Bright iridescent colors of the opal gemstone²⁸ with

ordered spheres of silica creating the effect²⁹. Reproduced from ref.²⁸. Copyright 2018, Mineralogical Society of America. Adapted from ref.²⁹. Copyright 2008, Mineralogical Society of America. (f) Colorful hairs of the seamouse³⁰ arise from structural holes filled with sea water³¹. Reproduced from ref.³⁰. Copyright 2001, CSIRO Publishing. Adapted from ref.³¹. Copyright 2003, Elsevier. (g) Blue iridescence of begonia plant leaves is created from stacked layered structures in iridoplasts³². Adapted from ref.³². Copyright 2016, Nature.

Material designs or applications with inspirations from naturally occurring phenomena or structures can be classified as biomimetic systems. The field of biomimetics is concerned with understanding and emulating systems found in nature for the purposes of establishing biologically inspired designs, adaptations or derivations³³. There are many examples of practical applications of natural biological structures. Biomimetic inspirations can be found in biological engineering³⁴, photonics³⁵, surface science³⁶, medical tissue engineering³⁷ and functional material designs³⁸. Through a combination of surface morphology, nano/micro structural design and the chemical composition of materials, many different effects can be imitated from biological constructs. Controlled hydrophilicity, surface adhesion, mechanical strength, anti-reflection, thermal insulation, aerodynamic lift and fluid drag reduction are among some of the biomimetic properties of commercial interest³³.

For a specific mechanical structural application of biomimicry, nacre layers composed of calcium carbonate and nanostructurally integrated biomolecules (proteins and polysaccharides) create ceramic materials with high mechanical strength in bivalves such as molluscs^{34 39} and are inspiring designs for biomedical implants due to their strong integration with bone tissue and excellent mechanical properties⁴⁰. Many emerging super hydrophobic or self-cleaning material surfaces feature structural design morphologies with prominent biomimicry of the lotus leaf effect^{24 41 42}. The fine nanostructure patterns found in moth eyes, a series of patterns and sub-wavelength bumps on the outer corneal lens, inspired the biomimetic development of anti-reflective coatings used to reduce reflections in surfaces such as those for solar cells^{43 44 45}. Figure 2 demonstrates the close relation between the natural structure of materials and the biomimetic nanostructured materials they have inspired for some of the effects discussed here. Many more examples of biomimetic designs exist in the literature with nanostructure designs in the natural world providing a blueprint for imitation and application of specific effects in emerging technologies.

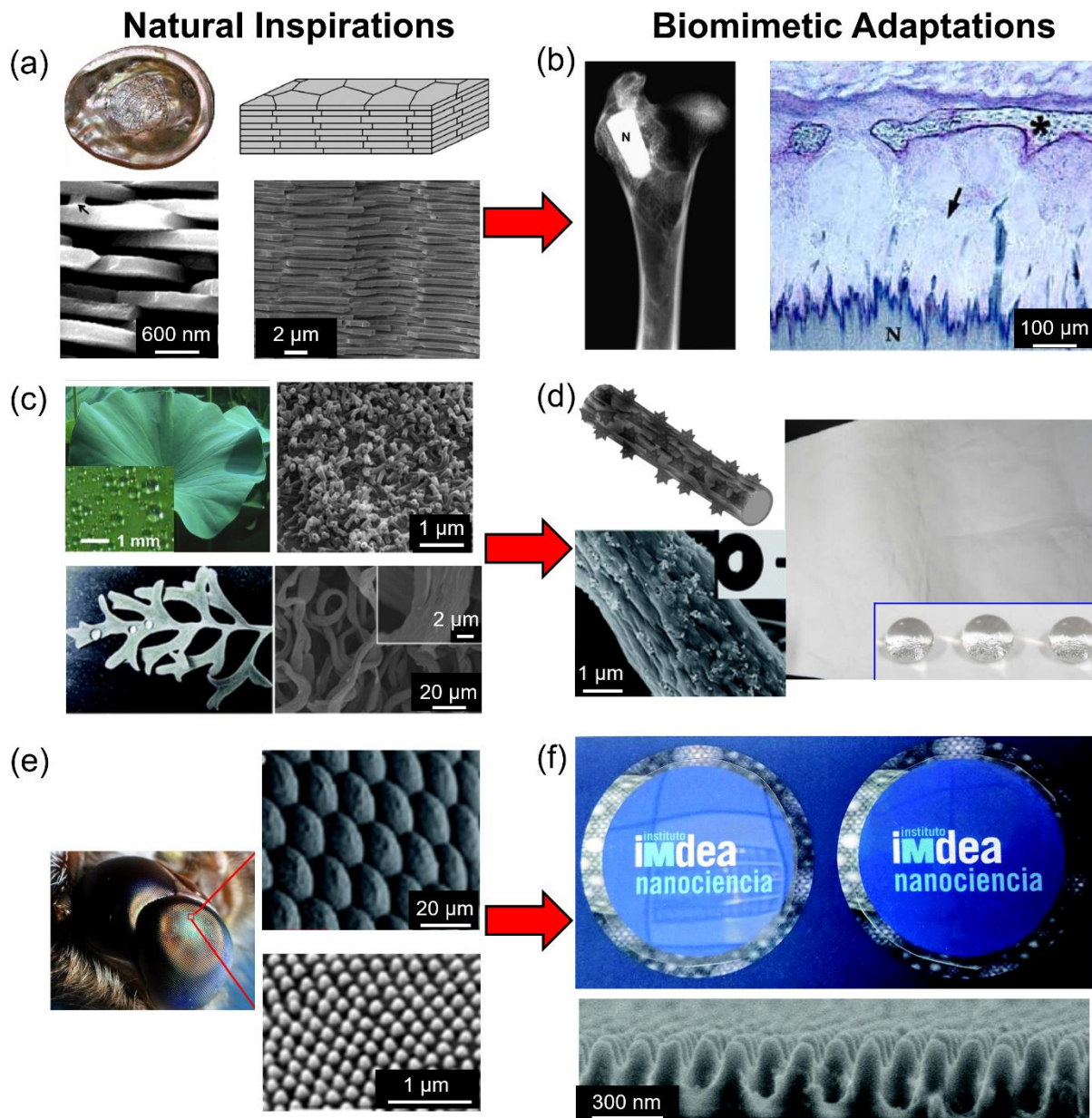


Fig. 2 Examples of natural structural biomimetic applications. (a) The stacked structure of nacre, shown in a schematic and from SEM images^{46 47}, found in the red abalone. Adapted from ref⁴⁶. Copyright 2007, Elsevier. Adapted from ref⁴⁷. Copyright 2004, the American Chemical Society. (b) Biomimetic inspired and durable bone implant in sheep based on nacre structures, nacre is marked as N in the radiograph⁴⁸ and optical microscope image⁴⁹. Reproduced from ref⁴⁸. Copyright 1999, Elsevier. Adapted from ref⁴⁹. Copyright 2005, Elsevier. (c) Nano-sized bumps on the lotus leaf²⁵ and the curved fibrous microstructure of the silver ragwort leaf⁴¹. Adapted from ref²⁵. Copyright 2011, Beilstein Institute for the Advancement of Chemical Sciences. Adapted from ref⁴¹. Copyright 2011, Royal Society of Chemistry. (d) Leaf-inspired polystyrene fibers coated with silica nanoparticles to create a polystyrene fiber mat with excellent hydrophobic properties⁴¹. Adapted from ref⁴¹. Copyright 2011, Royal Society of Chemistry. (e) Cone-shaped micro and nanostructures found on moth eyes^{50 51} create an anti-reflective effect. Adapted from ref⁵⁰. Copyright 2008, SPIE. Adapted from ref⁵¹. Copyright 2018, Nature. (f) Moth eye inspired TiO₂-PMMA nanocomposite structural film⁵² showing improved anti-reflective properties (right disc) versus a non-structured PMMA film (left disc). Adapted from ref⁵². Copyright 2018, Royal Society of Chemistry.

The concept of ordered structures and associated optical properties, such as structural color, are found in materials classified as photonic crystals (PhCs). From the first suggestions of alternating dielectric slabs and their applications to light manipulation^{53 54}, PhCs have been explored for their inherent optical abilities. The periodic structural order present in PhCs acts to attenuate specific photon frequencies from propagating through the structure. This control over photon frequencies is known as the photonic bandgap or photonic stopband of the structure. Depending on the degree of frequency depletion, complete photon inhibition is most commonly described by a complete or omnidirectional photonic bandgap⁵⁵ whereas partial or incomplete photon depletions are described by pseudo-photonic bandgaps or photonic stopbands^{56 57}. The photonic bandgap is often presented as an optical analogue to the electronic bandgap associated with allowed electron energy levels in semiconductor materials⁵⁸. The placement of atoms or molecules in semiconductor materials form a crystal lattice with a periodic potential which dictates the energy of electrons allowed to propagate through the semiconductor. Gaps in the energy band structure of the crystal lattice create forbidden electron energies in the material. For PhCs, the system of a periodic potential of atoms or molecules is replaced by a periodic dielectric function where different dielectric contrasts of larger ordered structures create similar effects for photons as seen with electrons. Much like in the case of semiconductor materials with band structures used to predict the electronic bandgaps of materials, the photonic bandgap can be predicted for materials through solutions of Maxwell's equations with specific knowledge of the lattice structure^{58 59}.

In addition to those occurring naturally, artificially structured PhCs are often manufactured and explored in relation to their ability to modulate certain frequency ranges of light. Artificial PhCs are architected in a variety of different structural forms depending on the application. In terms of the repeating nanostructure lattice, it is possible to form 1D (e.g. stacked dielectric slabs⁶⁰), 2D (e.g. arrays of dielectric rods with an ordered arrangement or patterned dielectric slabs with air perforations^{61 62}) and 3D PhC structures. Fully 3D PhCs can be designed as dielectric spheres in an air background (often called opals based on the arrangement of silica particles in an opal gemstone⁶³), inverse opal⁶⁴ (IO) air spheres in a high dielectric background, a dielectric slab with holes drilled through at specific angles called a Yablonovite structure⁶⁵ or layered stacks of dielectric rods forming a woodpile structure⁶⁶. Some of these common PhC constructs and designs are seen depicted in Fig. 3. All structures display a periodic dielectric contrast in their composition,

an essential component for establishing the photonic bandgap property of the material. Similarities between some of the natural nanostructure designs seen in Fig. 1 can be seen for many of the artificially designed PhC structures.

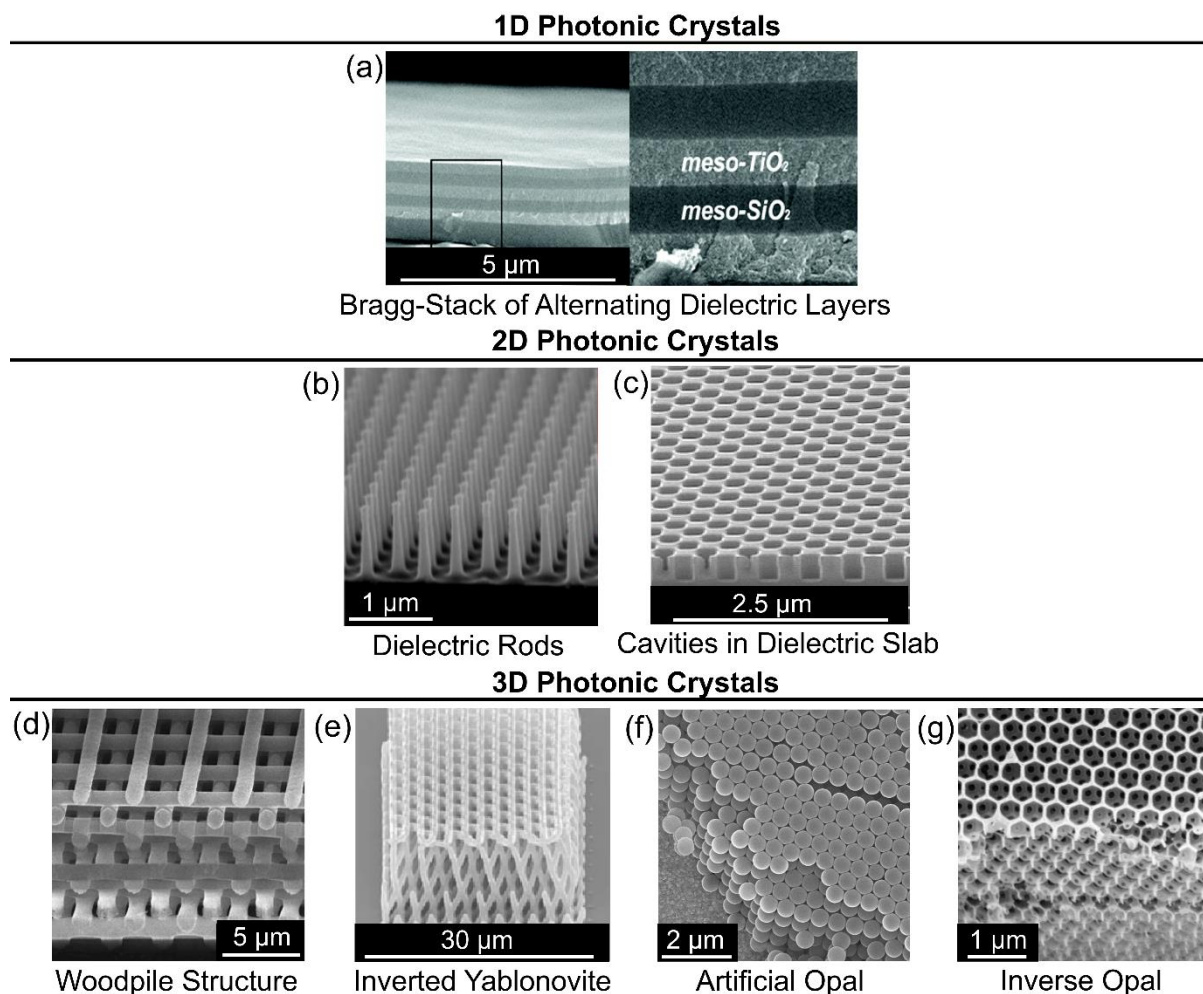


Fig. 3 Examples of artificial PhC structures. (a) 1D PhC with alternating TiO_2 and SiO_2 layers prepared via spin coating⁶⁷. Adapted from ref⁶⁷. Copyright 2006, American Chemical Society. (b) 2D PhC of dielectric rods of silicon in air background⁶⁸. Adapted from ref.⁶⁸ Copyright 2010, OPTICA. (c) 2D PhC consisting of ordered air cavities in a silicon background⁶⁹. Adapted from ref⁶⁹. Copyright 2006, Nature. (d) 3D PhC of a stacked woodpile configuration of a polymer mixture of poly(acrylic acid) and poly(ethylenimine)⁷⁰. Adapted from ref⁷⁰. Copyright 2006, Wiley-VCH. (e) 3D PhC of an inverted Yablonovite structure of silica⁷¹. Adapted from ref⁷¹. Copyright 2012, Springer. 3D PhCs showing ordered stacks in an FCC configuration for (f) artificial polystyrene opals and (g) a TiO_2 IO structure.

Light interactions with specific and ordered PhC planes can be predicted based on light diffraction, using the Bragg-Snell model to project diffracted wavelengths from the photonic stopbands of structures. Using this model as a basis, maximum wavelengths of reflection from the structure are predicted for the maximum constructive interference condition in the reflected wave. The Bragg-Snell treatment combines Bragg's law of diffraction for x-ray diffraction in crystal lattices with Snell's law of refraction for light incident

on media with different refractive indices. The Bragg-Snell law used for PhC structures with alternating dielectrics of refractive indices n_1 and n_2 , a light incidence angle on the entire structure of θ_1 , an interplanar spacing of d , a resonance order of m and wavelength of maximum diffraction λ can be stated as follows:

$$m \lambda = 2 d \sqrt{n_{eff}^2 - n_1^2 \sin^2 \theta_1} \quad (1)$$

A more detailed explanation of the origins of certain parameters and the derivation of this equation can be found in Appendix I. Looking at the Bragg-Snell equation, the maximum wavelength of diffraction is dependent on many factors associated with the structural composition of the PhC. The interplanar spacing (d), factors in the periodicity of the material and the overall geometry of the crystalline structure. The refractive indices (n_1 & n_2) incorporate the optical properties of the alternating dielectric materials and control the magnitude of n_{eff} , the effective refractive index. By this relation, changes to any of these parameters should result in changes to the wavelength of maximum diffraction from the PhC structure. This is important for both interpreting and understanding the optical properties of the nanostructured materials and also design and development of an optical application using PhCs. Control over the size or constituent materials of the structure enables the optical response of the material to be tuned over specific wavelength ranges^{72 73}, if desired. The tuning of the optical response of the material is an important consideration in the development of many artificial PhC structures for use in high sensitivity systems such as PhC display screens^{74 75} or sensors^{76 77}. Knowledge of the relation between nanostructure and optical behavior has furthered the understanding of many natural observations such as material iridescence or color changes associated with liquid infiltration^{20 78}. Figure 4 displays some of the changes observed to structural coloration for both natural and artificial PhCs which can be understood through changes to the wavelength of maximum diffraction of the Bragg-Snell relation.

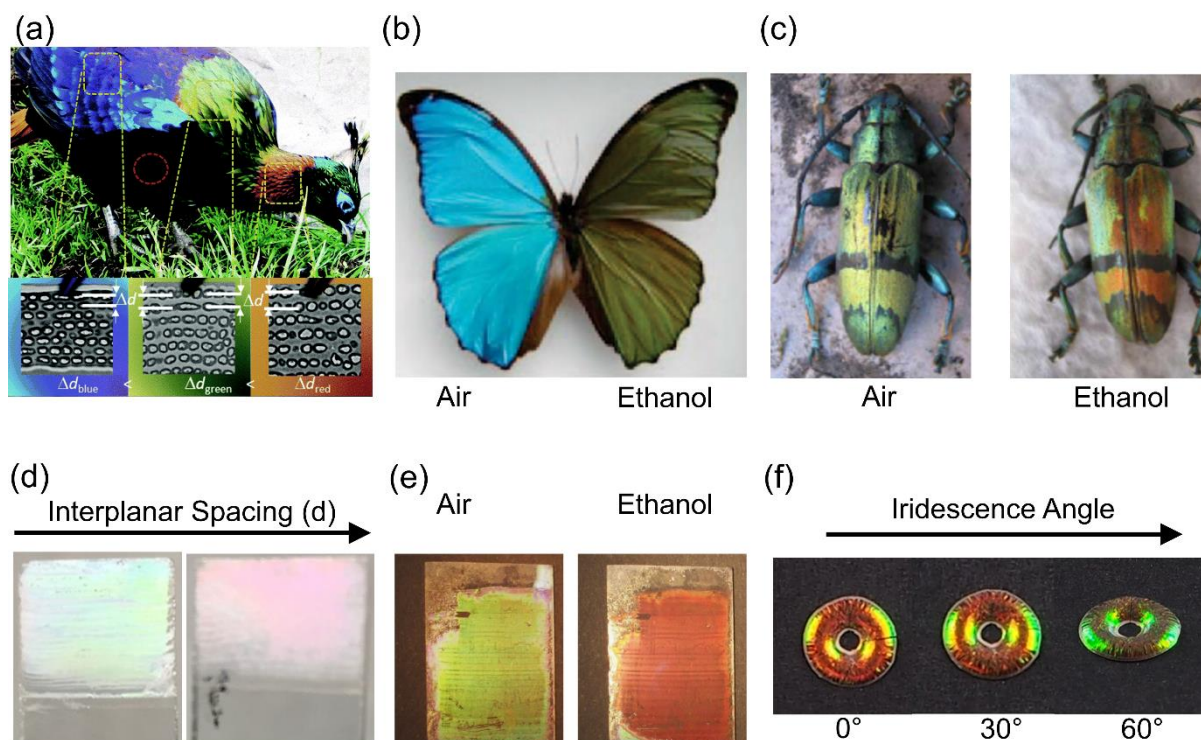


Fig. 4 Changes to structural coloration associated with periodicity, material composition and viewing angle for several PhC structures. Shorter structural color wavelengths are reflected for smaller interplanar spacing periods shown for (a) the red, green and blue feathers of the Himalayan monal⁷⁹ and (d) TiO₂ IOs of diameters 384 nm (pink/red) and 278 nm (green). Adapted from ref.⁷⁹. Copyright 2020, Royal Society of Chemistry. Shifts to longer wavelength structural colors are displayed for the replacement of air with ethanol in (b) *Morpho menelaus* butterfly wings⁸⁰ changing from blue to green. Adapted from ref.⁸⁰. Copyright 2009, Nature. (c) *Tmesisternus isabellae* shells²⁷ changing from yellow/green to orange. Adapted from ref.²⁷. Copyright 2009, OPTICA. (e) ZrO₂ IOs (287 nm diameter coated with 5 wt% Au) shifting from a green to orange color⁸¹. Adapted from ref.⁸¹. Copyright 2018 American Chemical Society. (f) Iridescence is observed for 285 nm diameter polystyrene spheres coated with thin (2.5 nm) polydopamine shells⁷⁸, showing a shift to shorter wavelengths with increasing incidence angle. Adapted from ref.⁷⁸. Copyright 2016, Nature.

In terms of the optical response of these materials, understanding and predicting the light interaction process is critical when developing applications centred around the structural color of the material. Advancements in the construction of colloidal particle templates has allowed for greater order and flexibility in the design of PhCs based on colloidal particle templating, such as opals and IOs⁸²⁻⁸³. Feature sizes, defects and material choice all act to influence the signature optical response of these materials. Tuning the optical response of prepared PhCs post-production has also been studied extensively, showing that factors such as stretching deformation⁸⁴ or solvent infiltration⁸⁵ among many others have important considerations for the structural color of the material.

Knowledge of the flexibility of the photonic stopband and the associated structural color of the material creates specialised applications involving the wavelength of light reflected from the structure. Electrical tuning of an opal template with infiltration of a metallo-polymer substance has been demonstrated to tune the wavelength reflected from the structure and create a tunable photonic response, with potential applications in PhC color displays⁸⁶ for substances dubbed photonic inks⁸⁷. This wavelength shift is attributed to expansion and contraction of layer spaces in the material due to the swelling of the infiltrated material with an applied voltage. The magnetic response of the photonic bandgap of superparamagnetic colloidal nanoparticles has been exploited to develop anti-counterfeit PhC labels where the structural color of the anti-counterfeit strip is dependent on the applied magnetic field^{88 89}. Figure 5 illustrates the electrical and magnetic tuning effects of the structure utilised in these applications. In these examples, the application of the PhC is directly linked to the structural color and the visual appearance of the material emphasising the importance of understanding the effect of the photonic stopband and the factors which affect wavelengths reflected from the film surface.

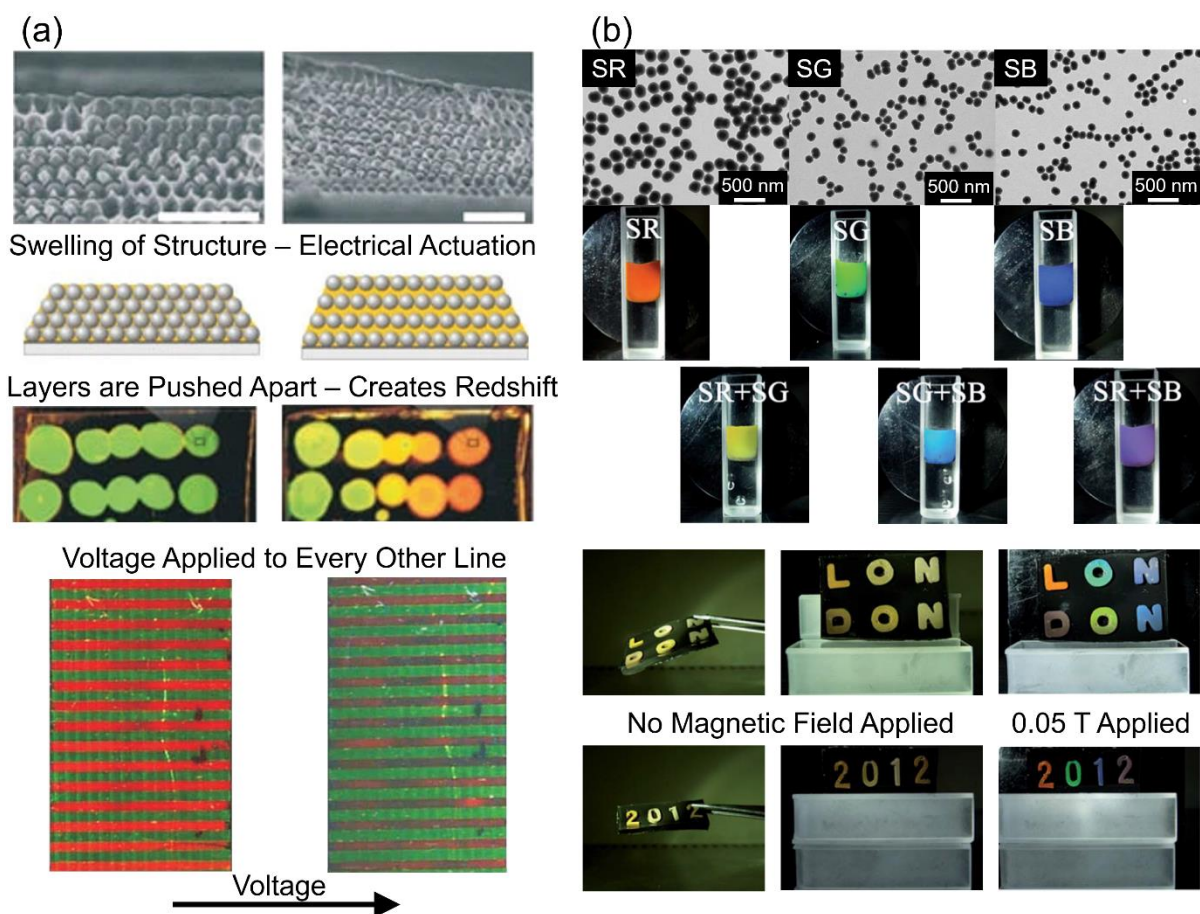


Fig. 5 Applications of PhCs centred around the visual appearance of structural color. (a) Electrical actuation of silica spheres in a cross-linked network of polyferrocenylsilane is shown to induce a redshift for structural swelling and the application of this technique to color display screens is demonstrated via a voltage induced redshift to the structural color of the PhC composite on indium tin oxide layers⁸⁶. Adapted from ref.⁸⁶.

Copyright 2007, Nature. (b) Magnetic structural color tuning of superparamagnetic colloidal nanoparticles, achieved through magnetic field particle ordering, is shown for an applied magnetic field of 0.1 T for particles sizes $SR = 200$ nm, $SG = 140$ nm and $SB = 125$ nm with structural color tuning demonstrated for anti-counterfeiting purposes where an applied magnetic field is a requisite for a visible color display⁸⁸. Adapted from ref.⁸⁸. Copyright 2012, Royal Society of Chemistry.

Research into applications involving the structural color of PhC films is continually innovating with new advancements steadily emerging from the literature. The concept of tuning the light reflected from the film surface creates a fascinating application where the structural color detected visually can selectively be altered for an observer. Figure 6 details some of the recent studies which utilise the structural color effect of PhC films in their primary application. The work shown in Fig. 6 (a) is a prime example of biomimicry where the dermal layers of a gecko inspired the design for a temperature dependent PhC film with tunable color and transmittance intensity by incorporating thermochromic and electrochromic pigments into the film. The environmental temperature was found to affect the color of the film and an applied voltage affected the transmittance of the film to light, with a suggested application to smart windows with a variable degree transmittance linked to an applied voltage⁹⁰. Controllable PhC film iridescence, where structural color appears to vary with viewing angle, has been explored for images printed with colloidal photonic inks, as depicted in Fig. 6 (b). For SiO_2 particles dispersed in acrylate-based resins, the relative degree of viscosity of the dispersion resin was found to impact the vibrancy and iridescence of structural color for the printed images with broader reflection peaks and less iridescent images found to arise from higher viscosity resins⁹¹.

Automotive paint coatings based on SiO_2 photonic crystals in a solvent medium spray coated onto surfaces and re-coated with a commercial clear coat are shown in Fig. 6 (c). The resultant PhC films displayed vibrant colors which could be tuned by the SiO_2 particle size or by using combinations of different sizes to achieve films of mixed colors. Films were resistant to mechanical and chemical stress tests and exhibited high structural color iridescence making them attractive candidates for automobile paint⁹². Figure 6 (d) illustrates the design for a finger motion-sensing device based on a 1-D PhC design of an interpenetrated hydrogel network block copolymer with alternating water absorbable and non-absorbable lamellae which was found to be sensitive to relative humidity⁹³. The expansion of the hydrogel network in response to relative humidity caused a red-shift in the structural color of the film and the natural humidity of the human finger was capable

of being detected by the PhC film depending on the relative degree of proximity and motion. Arrays of these PhC films could even be used to detect the motion of a human hand using the same principle, creating a motion sensor based on the visual structural color appearance of the PhC film.

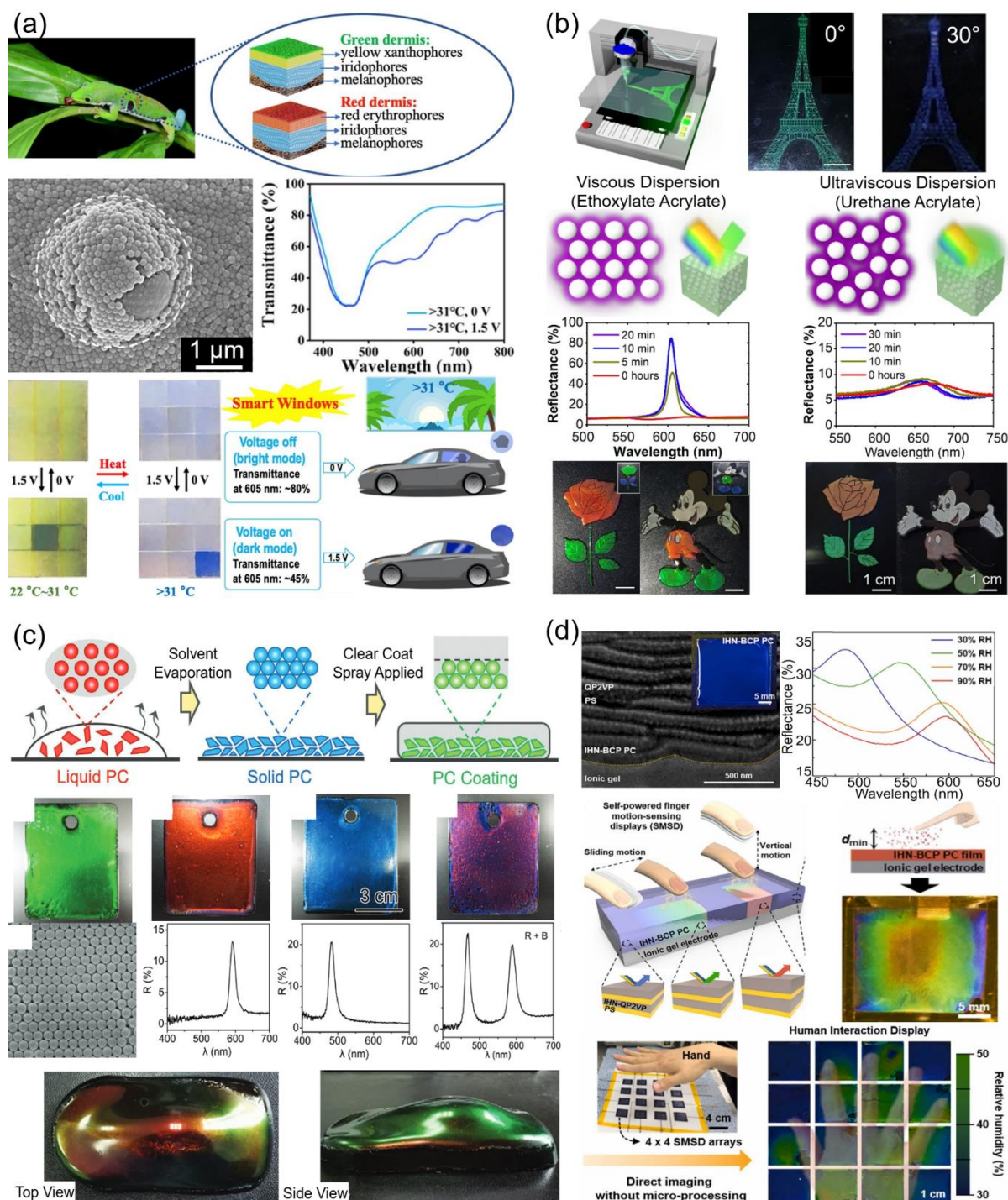


Fig. 6 Emerging applications of PhCs with a dependence on their structural color. (a) Temperature-dependent thermochromic microcapsules incorporated into a PhC film inspired by layers in gecko dermis⁹⁰. Structural color was dependent on temperature and film transmittance was affected by applied voltage, with a proposed application for smart windows. Adapted from ref⁹⁰. Copyright 2022, Elsevier. (b) Colloidal photonic inks used to print images with controllable degrees of iridescence depending on the relative viscosity of the particle dispersion medium⁹¹. Adapted from ref⁹¹. Copyright 2021, American Association for the Advancement of Science. (c) Easily spreadable and durable PhC films deposited by spray coating SiO₂ particles dispersed in solvent with a proposed application for automotive coatings⁹². Adapted from ref⁹². Copyright 2021, Wiley-

VCH. (d) A 1-D PhC film of a block copolymer with an interpenetrated hydrogel network showing structural color sensitivity to relative humidity for use as a finger motion-sensing display by utilising the natural humidity of a finger⁹³. Adapted from ref⁹³. Copyright 2022, Elsevier.

There are, of course, other emerging applications involving PhC films which hinge on the observation of a structural color. The vivid colors and iridescence associated with PhC films makes them particularly appealing for decorative designs for textiles^{94 95 96 97}, photonic glasses^{98 99 100} and even wood surfaces^{101 102}. The freedom to tune the photonic response and structural color in PhCs also makes them suitable for encoding information, often through controlled wettability^{103 104 105 106} using a solvent, for applications involving anti-counterfeiting measures^{107 108 109}. Aside from the applications involving direct observation of a change to the structural color of a PhC, many research fields have specifically adopted PhCs for their ability to direct and alter the optical properties of structured materials. Nanostructures designed and applied to materials have been exploited for the photonic effects induced on the structure.

The proceeding sections will detail and review the mechanism of operation and application of PhC structures as applied to common research interests which specifically exploit and utilise the optical properties of the photonic bandgap or stopband in their application. Of course, other physical properties of these structures are often cited for their uptake and application to certain research areas and these will be discussed also. These would include an increased exposed surface area for improved electrochemical performance^{110 111} or photocatalysis reactions^{112 113} and the advantages of the scaffold architecture of these ordered structures to biomedical research areas such as tissue engineering or regenerative medicine^{114 115}. For this work, emphasis is placed on the importance of the optical response of these ordered photonic materials by selectively examining applications with fundamental relations to the optical performance of the structured material. More specifically, the optical properties of PhCs will be examined in relation to their implementation in material sensor devices, solar cell technology, photocatalytic materials and waveguides in optical fibers. Principally, the design, understanding and valid interpretation of the optical response of these materials will be shown to be crucial for the incorporation of PhCs in these areas of research.

2 Photonic Crystal Materials as Optical Diagnostic Sensors

One of the most prevalent applications of the optical behavior of PhC materials involves their ability to act as optical sensors, assessing a range of different material properties using the signature optical response of the ordered structure. The Bragg-Snell relation, as seen in eqn 1, allows wavelength shifts in the maximum wavelength position of diffracted light from the material to be predicted and interpreted. Optical sensors exploit the wavelength shift of the photonic bandgap or stopband to identify and assess changes to the material or material environment using the optical response of the structure. Typically, wavelength shifts in these structures are brought about by changes to the effective refractive index (n_{eff}) or the interplanar spacing (d) of the structure. In alternating dielectric materials of refractive indices n_1 and n_2 occupying volume fractions φ_1 and φ_2 , the effective refractive index n_{eff} of the structure is commonly estimated by^{73 81 116 117}:

$$n_{\text{eff}} = n_1 \varphi_1 + n_2 \varphi_2 \quad (2)$$

Combining this relation with eqn 1, an expression for all the factors influencing the maximum wavelength position of the photonic stopband is given by:

$$m \lambda = 2 d \sqrt{(n_1 \varphi_1 + n_2 \varphi_2)^2 - n_1^2 \sin^2 \theta_1} \quad (3)$$

From eqn 3, the position of the photonic stopband is dependent on the interplanar spacing between layers, the angle of incidence and both of the refractive indices of the alternating dielectric materials. Porous materials, where the alternating dielectric consists of a high index material in a low index air background, are particularly suited to exploit this wavelength dependence on both the high index material (n_2) and the low index background voids (n_1) for optical sensor applications. Wavelength shifts associated with the photonic stopband can be used to identify materials which can freely occupy void space in the structure, effectively changing the refractive index contrast of the PhC. Likewise, engineered changes to the interplanar spacing or refractive index of the high index material can also be used to diagnostically assess changes to the material system.

In terms of acting as an optical sensor, perhaps the simplest application of this analysis arises from material characterisation for artificial opal and IO structures. For a known material, the wavelength position of the photonic stopband can be used to determine the size dimensions of the ordered structure from the interplanar spacing. This optical dimensional analysis has been frequently shown to accurately determine the size of the repeating structure, as compared with microscopy measurements^{73 118 119}. The appearance of the photonic stopband can also be used as an indicator of the degree of monodispersity present in the sample, with stronger scattering and lower optical transmittance associated with higher disorder and lower monodispersity^{120 121}.

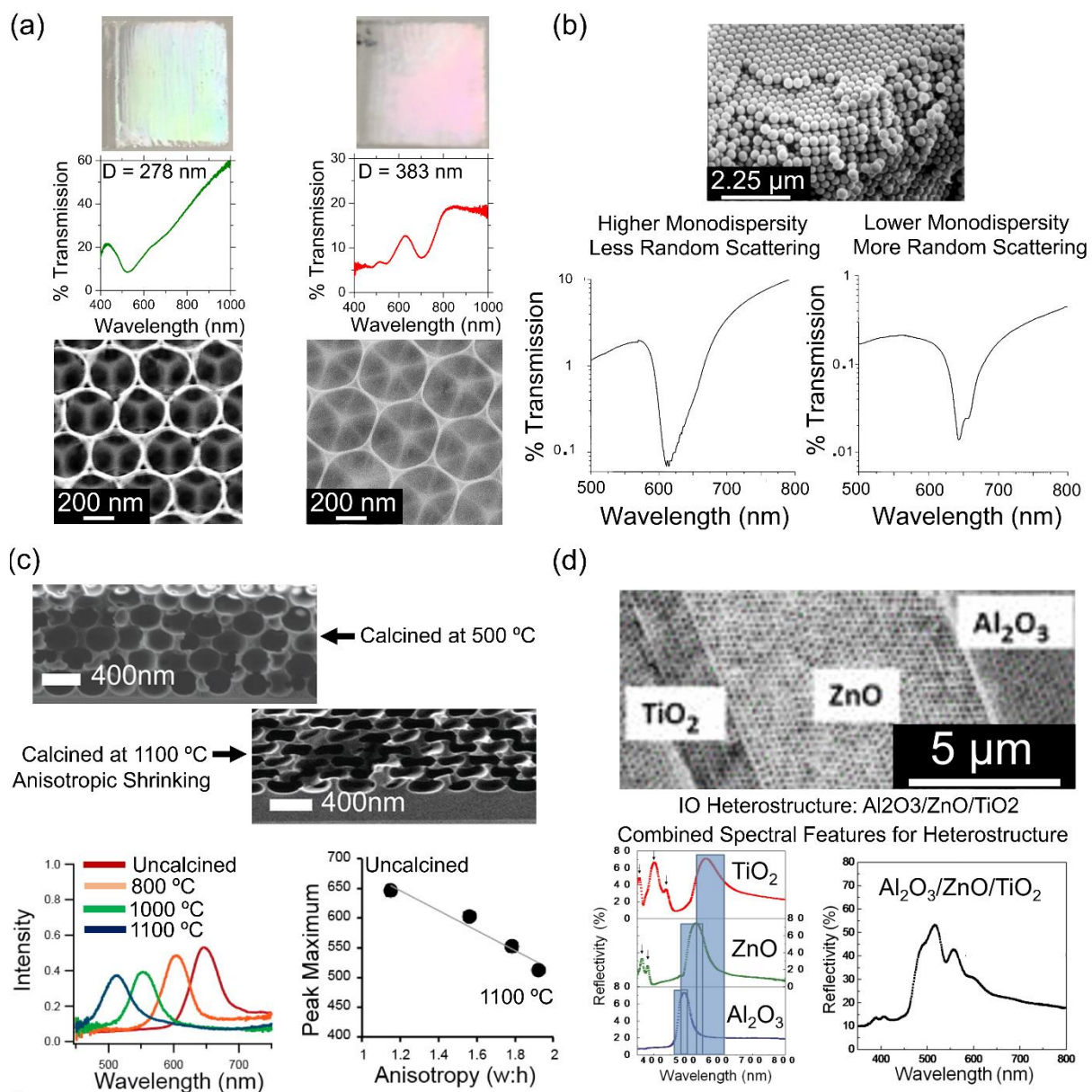


Fig. 7 Examples of material characterisation and assessment of PhCs using the optical stopband. (a) Two TiO₂ IOs with measured centre-to-centre pore distances of 278 nm (green) and 383 nm (red) can be distinguished by the different positions of the optical stopband¹²². Adapted from ref¹²². Copyright 2018, American Institute

of Physics. (b) The degree of scattering and transmittance intensity of the optical spectrum of two identically thick SiO₂ opals are shown to indicate relative monodispersity in the sample¹²¹. Adapted from ref¹²¹. Copyright 2001, Wiley-VCH. (c) The optical stopband position indicates anisotropic shrinking of an SiO₂ IO related to the calcination temperature upon inversion¹²³. Adapted from ref¹²³. Copyright 2014, American Chemical Society. (d) The optical spectrum of an Al₂O₃/ZnO/TiO₂ IO heterostructure is shown with identifying features of the optical stopband arising from each individual IO structure¹²⁴. Adapted from ref¹²⁴. Copyright 2009, American Institute of Physics.

IOs prepared using sol-gel methods from artificial opal templates, are known to feature reduced lattice constants upon heating and inversion relative to the initial opal template^{117 125 126}. An optical assessment of the IO dimensions can provide a quick means to quantify any shrinking upon inversion. For 3D PhC structures, the information from the photonic stopband is relevant for the entire 3D surface interacting with incident light, whereas scanning electron microscopy assessment is largely limited to surface information. The photonic stopband is therefore ideal for non-destructively assessing any 3D structural anisotropy which might be present in the material¹²³. For known size dimensions, the optical information of the photonic stopband can, in principle, be used to assist in identifying the material comprising the PhC network. The refractive indices of materials, as determined from the optical stopband analysis, have been frequently used, in conjunction with other analytical methods, to determine the crystalline material of IO structures, even for composite or heterostructure materials^{124 127 128}. Figure 7 provides an overview of some of the optical sensing and material characterisation related to photonic stopband analysis.

In a broader sense, the optical sensing ability of PhC materials extends far beyond simple material characterisation of the structures themselves. With proper calibration and knowledge of the optical spectrum, PhCs have been demonstrated to operate as excellent sensors for a range of different chemical substances. The photonic stopbands of SiO₂, ZrO₂, TiO₂, SnO₂, CeO₂ and Al₂O₃ IOs have exhibited a predictable and reversible shift of the principle diffraction peak upon addition of various solvents to occupy voids in the structures^{73 116 117 129 130}. The refractive index of the solvent and the Bragg-Snell relation proved to function as an excellent predictor of the wavelength shift observed for the photonic stopband. The transmission dips associated with the stopband red-shifted to longer wavelengths with increasing solvent refractive index. This spectral shift with solvent refractive index creates a sensing application, where the wavelength position of the photonic

stopband in a properly calibrated structure can be used to determine the refractive index of a liquid infiltrating the PhC.

The sensitivity of this type of approach is particularly appealing for identifying mixtures or solution concentrations. TiO₂ IOs have been developed that are sensitive to various concentrations of ethanol solutions¹³¹, with reported variations in refractive indices smaller than 0.002 yielding shifts in the stopband position greater than 1 nm¹³². Similar work for ethanol solutions in WO₃ IOs confirm the ability to optically sense the concentration of ethanol in binary ethanol/water solutions¹³³. Solvent/water mixtures and their concentrations are particularly well studied for photonic crystal detection systems^{131 134 135}. More recently, some works have focused on developing photonic crystal sensors which offer a visual structural color indicator for the presence and concentration of particular solvents^{136 137 138}, with even the optical image intensity and peak absorbance linked to ethanol concentrations for SiO₂ IOs¹³⁹. Similarly, carbon IOs have demonstrated promising oil sensing capabilities with excellent response times and reversibility of the photonic stopband¹⁴⁰. The visual structural color of oil/gasoline and ethanol/gasoline mixtures has been exploited to indicate mixture concentrations in SiO₂ IO coated with hydrophobic fluoroalkylchlorosilanes¹⁴¹. In this case, the appearance of the structural color is dependent on the wettability of the coated IO with respect to different concentrations of oil/gasoline or ethanol/gasoline.

Photonic stopband shifts are not limited to just liquid detection. Gas and vapor sensors have been developed using the principle of the spectral shift in PhC materials. Visual detection of volatile aromatic hydrocarbon vapors was achieved using a 1-D photonic crystal in which layers would swell, inducing a shift in structural color, when detecting compounds like benzene, toluene or xylene¹⁴². SiO₂ IOs coated with polyvinyl alcohol display a spectral red shift with respect to the relative humidity in water vapor¹⁴³. The polyvinyl alcohol acts to swell in the presence of water vapor, altering the space between SiO₂ layers and leading to the red-shift. A visual spectral red shift of the photonic stopband of over 50 nm was recorded for SiO₂ IOs infiltrated with tetraphenylethene polymer in the presence of organic vapors of tetrahydrofuran and acetone¹⁴⁴. This red shift is attributed to an increase in the effective refractive index of the structure caused by adsorption of the organic vapor by the polymer substance. Similar applications of polymer infiltrated SiO₂

IOs have been developed for detecting aromatic volatile organic compounds such as xylenes¹⁴⁵. Likewise, spectral red shifts are proposed to arise from increases to the effective refractive index of the structure caused by adsorption of organic vapor by the polymer. Figure 8 illustrates the stopband sensing capabilities for various IO structures to different analytes.

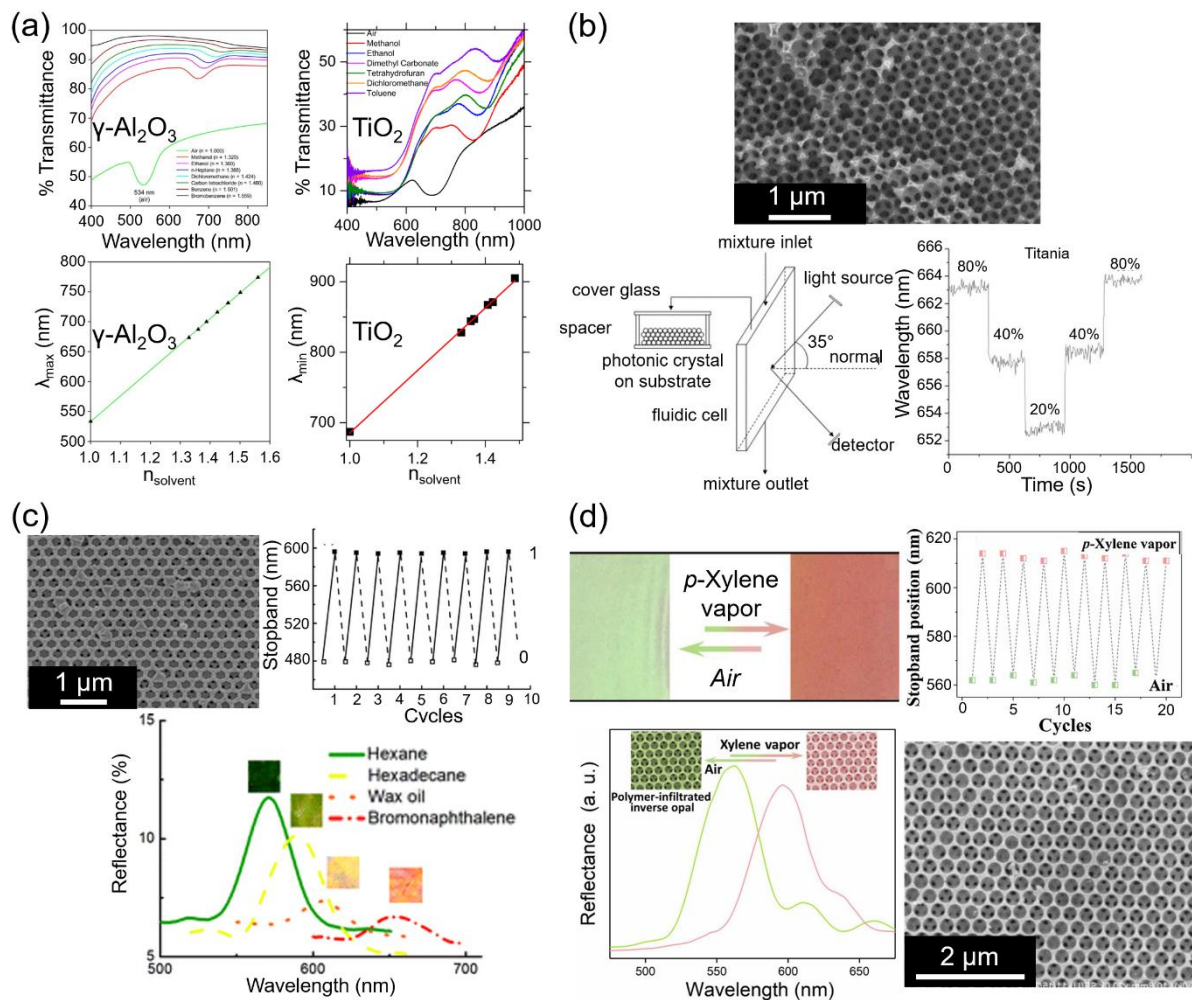


Fig. 8 Applications of the photonic bandgap in solvent and vapor sensing. (a) The optical stopbands for a $\gamma\text{-Al}_2\text{O}_3$ ¹¹⁷ and TiO_2 ¹²⁹ IO red-shift continually with the addition of higher refractive index solvents. Adapted from ref¹¹⁷. Copyright 2015, American Chemical Society. Adapted from ref¹²⁹. Copyright 2020, American Physical Society. (b) Design of a TiO_2 IO ethanol sensor where the shift in stopband can be related to ethanol concentration in ethanol/water mixtures¹³². Adapted from ref¹³². Copyright 2007, Elsevier. (c) A carbon IO using the photonic stopband position to distinguish between different oils with strong recyclability between test cycles¹⁴⁰. Adapted from ref¹⁴⁰. Copyright 2008, Royal Society of Chemistry. (d) A polymer infiltrated SiO_2 IO calibrated to display a visual colorimetric response of the photonic stopband in the presence of xylene vapor with promising recyclability of the sensor across detections¹⁴⁵. Adapted from ref¹⁴⁵. Copyright 2019, Elsevier.

Specialised applications of PhC structures are present in PhC optical fibers, commonly used as sensitive refractive index sensors. PhC optical fibers and waveguides will be covered in more detail in Section

5. For now, emphasis will be placed on their ability to distinguish between small variations in refractive index. 2D PhC slabs with air holes etched in a square or triangular lattice into a slab of dielectric material, such as seen depicted in Fig. 3 (c), are commonly used as the basis for a photonic waveguide. In simple terms, a waveguide is created when certain rows of the periodic structure are removed, e.g. air holes are selectively not-etched into specific row(s) of the dielectric material. Light propagating in this region is confined by the photonic bandgap of the surrounding periodic structure in the plane of the PhC and total internal reflection effects of the optical fiber out of the plane of the plane of the slab. Defects introduced to the PhC regions act to create allowed modes for photon propagation in the photonic bandgap region of the structure. Defects can be introduced by removing holes or changing their radii in the repeating structure. The newly allowed photon propagation frequencies create an optical cavity in the defect region, introducing an optical confinement effect. Spectrally, these optical cavities appear as resonances with sharp dips/peaks on the optical spectrum of the PhC fiber. The wavelength position of these spectral features is strongly linked to the refractive index of the surrounding medium, through evanescent waves of the optical cavity interacting with the neighbouring material of the fiber.

The sensitivity of the resonant mode frequencies to the surrounding material has been exploited in PhC fibers for refractive index sensing, as seen in Fig. 9. One or more of the air cavities in the PhC structure can be filled or continually pumped with an analyte which can be assessed via changes to the resonant mode wavelength. Calibration of a particular sensor design for multiple refractive indices should allow for accurate determination of analyte materials based on their refractive indices. The design of the optical cavity and waveguide will determine the spectral properties of the sensor. A seven-cavity (L7) wide defect in a silicon-on-insulator wafer has been demonstrated to feature a 12.65 nm shift in the resonant mode wavelength position when switching between water and ethanol, constituting a significant wavelength shift for a small refractive index difference of just 0.027¹⁴⁶. Salinity PhC fiber sensors, designed for detecting salt concentration in sea water, have been shown to detect salt concentrations in water via shifts in the resonant wavelength of confinement losses corresponding to minor shifts in the refractive index of salt water solutions ranging from 1.3326 to 1.3505 (0 – 100%)¹⁴⁷.

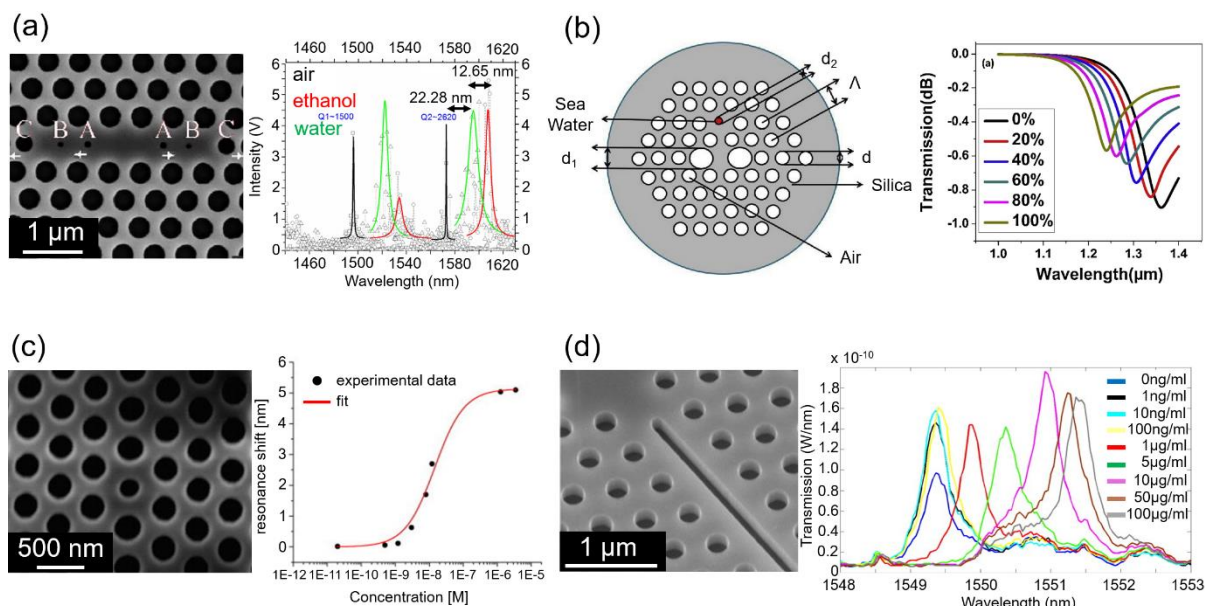


Fig. 9 PhC fiber sensor designs for detecting a range different substances. (a) A seven cavity wide microcavity in a silicon-on-insulator wafer displaying a wavelength shift of 12.65 nm for a refractive index difference of 0.027 between water and ethanol¹⁴⁶. Adapted from ref¹⁴⁶. Copyright 2012, OPTICA. (b) Air holes patterned into a silicon fiber sensor used to detect relative salinity in seawater¹⁴⁷. Blue-shifts in the confinement loss spectra correspond to higher salinity levels. Adapted from ref¹⁴⁷. Copyright 2018, Elsevier. (c) A silicon-on-insulator PhC fiber with a smaller central cavity for light confinement is used to monitor anti-biotin levels in bovine serum by measuring the shift in resonance position with concentration¹⁴⁸. Adapted from ref¹⁴⁸. Copyright 2009, Elsevier. (d) A slotted PhC cavity on a silicon-on-insulator substrate monitors dissolved avidin concentrations using the shift in cavity resonant wavelengths¹⁴⁹. Adapted from ref¹⁴⁹. Copyright 2011, Elsevier.

Biological processes such as protein binding can be monitored over time using this change in refractive index of the resonant modes. The binding of anti-biotin to biotinylated-bovine serum albumin was monitored over time using the shift in resonance wavelength of the PhC fiber as an indicator of the anti-biotin concentration with detection sensitivity estimated at just 20 pM of anti-biotin concentration¹⁴⁸. Similarly, PhC cavities functionalised with biotin were used to detect dissolved avidin concentrations by monitoring resonant wavelength shifts with distinct peaks shifts observed at concentrations of 1 $\mu\text{g}/\text{mL}$ ¹⁴⁹. PhC sensors can also be specifically designed to detect a plethora of other material parameters, including temperature, curvature, pressure, strain or electric field^{150 151}.

PhC hydrogels are increasingly common sensors designed to monitor and track changes to specific polymer infused PhC structures with a wide array of applications, particularly in biological and medical fields. Conceptually, the operation of these hydrogel systems is similar to the process of electrical actuation depicted in Fig. 5 (a), where applied voltages increased the separation between PhC layers. Hydrogel systems used for

optical sensing applications are typically designed such that the signature optical wavelength of the photonic stopband shifts in response to a swelling or contraction of the polymer medium upon exposure to certain chemicals or environmental conditions. Principally, it is the shift in the photonic stopband that allows a monitoring of the hydrogel material. The hydrogel polymer is selected to react with specific chemicals or biomolecules, creating a distinct optical response indicating the specific presence of reactant species.

Chemically, PhC hydrogels have been used as sensors to detect a number of different system properties. As previously discussed, humidity sensors were developed using polyvinyl alcohol embedded in SiO₂ layers¹⁴³. Polyvinyl alcohol hydrogel sensors have also been developed for pH detection, displaying a 350 nm wavelength shift of the photonic stopband position for pH values varying between 3.3 and 8.5¹⁵². The hydrogel responds to increasing pH with an increase in the osmotic pressure of the polymer created when carboxyl groups are ionised and counter ions become immobilised in the hydrogel. The increase in osmotic pressure acts to swell the hydrogel, increasing the separation between polystyrene sphere layers and red-shifting the photonic stopband. This method of pH sensing was also found to apply to polyacrylamide hydrogels, where the swelling and shrinking of the gel caused by osmotic pressure was indicative of the pH and ionic strength of the solution¹⁵³.

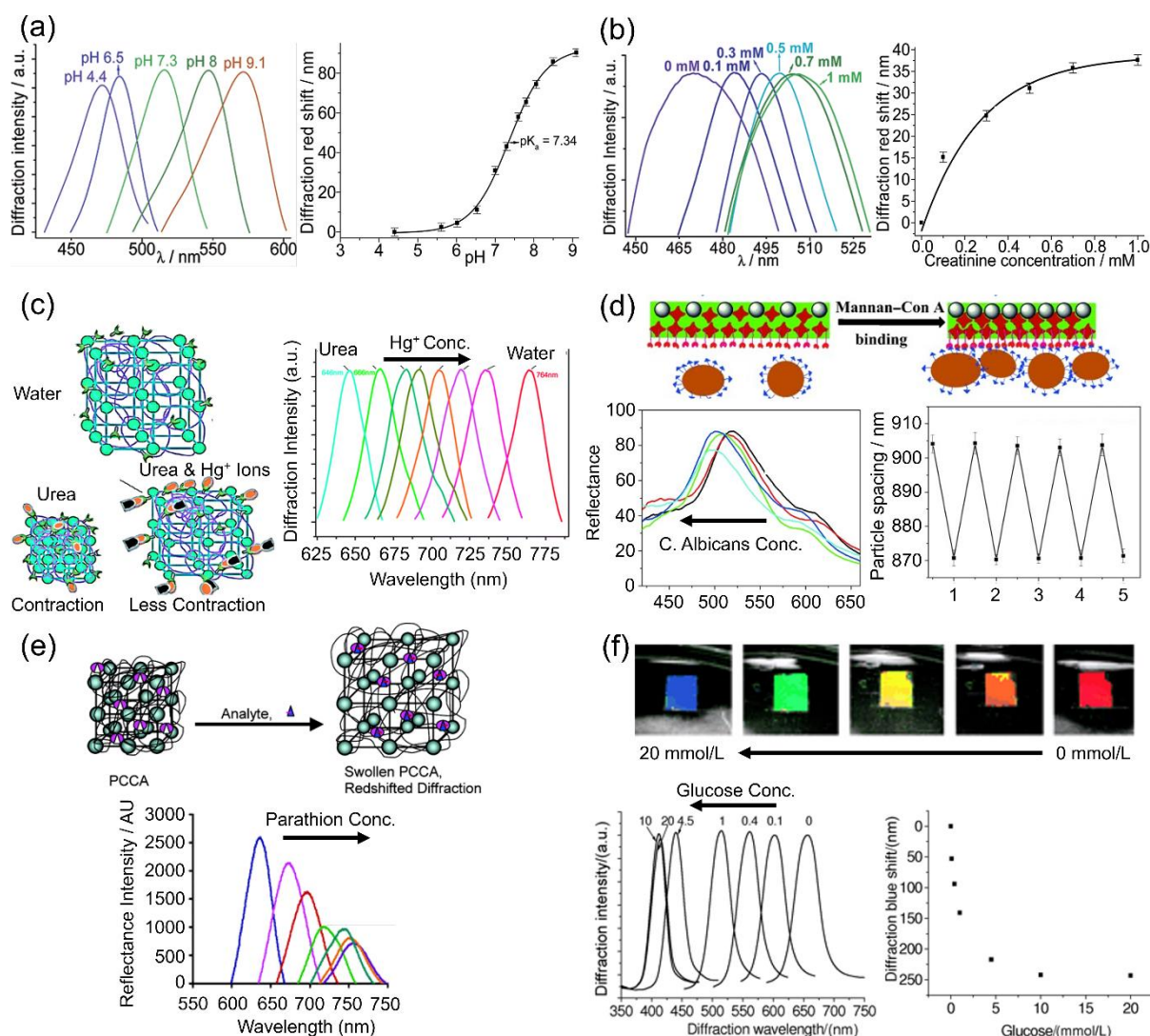


Fig. 10 Hydrogel PhC sensor applications. (a) The photonic stopband position of a polyacrylamide hydrogel functionalised with 2-nitrophenol surrounding a polystyrene PhC is demonstrated to be sensitive to pH¹⁵⁴. Adapted from ref¹⁵⁴. Copyright 2004, American Chemical Society. (b) The pH sensitivity of this hydrogel is further shown to act as an optical indicator for creatinine concentrations¹⁵⁴. Adapted from ref¹⁵⁴. Copyright 2004, American Chemical Society. (c) Mercury ions concentrations in water are shown to inhibit the contraction of urease hydrogel networks when exposed to urea, reducing the observed stopband blue-shift¹⁵⁵. Adapted from ref¹⁵⁵. Copyright 2011, Royal Society of Chemistry. (d) The presence of candida albicans in a Concanavalin A functionalised hydrogel is illustrated to contract the hydrogel network, creating a stopband blue-shift for optical monitoring¹⁵⁶. Adapted from ref¹⁵⁶. Copyright 2015, Wiley-VCH. (e) A red-shift in the photonic stopband position indicates the presence of parathion species, an organophosphate nerve agent, via an induced swelling of the hydrogel¹⁵⁷. Adapted from ref¹⁵⁷. Copyright 2005, American Chemical Society. (f) Glucose concentrations in polyacrylamide-polyethylene glycol hydrogel systems are detected via a blue-shift in the stopband position with increasing concentration¹⁵⁸. Adapted from ref¹⁵⁸. Copyright 2004, American Association for Clinical Chemistry.

Metal ions, such as Pb²⁺, Ba²⁺ and K⁺, could also be detected in similar systems by attaching crown ether molecules to the hydrogel networks which complexed with the metal cations and increasingly red-shifted the photonic stopband through increased osmotic pressure created with higher concentrations of metal ions binding to the crown ether¹⁵⁹. This hydrogel sensing method has been adapted for detecting various metal ions

in systems, e.g. toxic mercury ions in water¹⁵⁵ or toxic divalent beryllium (Be^{2+}) ions in seawater¹⁶⁰. Immobilised urease in a hydrogel system was found to react with urea to produce NH_4^+ and HCO_3^- ions which shrink the hydrogel, creating a blue-shift of the photonic stopband relative to the system in pure water. Hg^{2+} ions inhibit the urea reaction from proceeding inducing a relatively smaller blue-shift depending on the concentration of ions.

Outside of chemical applications, biomedical studies have adapted PhC hydrogels to respond to biomolecules, proteins and viruses for detection or monitoring of concentration levels. Polyacrylamide hydrogels functionalised with a creatinine deiminase enzyme and a 2-nitrophenol embedded in a polystyrene PhC structure have been demonstrated to function as a concentration sensor for creatinine levels in blood samples, a useful indicator in monitoring renal dysfunction¹⁵⁴. A red-shift in the photonic stopband was linked to higher concentrations of creatinine, explained as an increase in pH resulting from hydroxide released from creatinine metabolism and an osmotic swelling of the hydrogel. Fungal microbes have also been detected by hydrogel systems. *Candida albicans*, a fungal microbe in which overgrowth in humans can lead to illnesses like pneumonia, was detected via a blue-shift in the photonic stopband related to a shrinking of the Concanavalin A protein hydrogels in a 2D PhC arrangement¹⁵⁶.

Hydrogel designs for detecting harmful organophosphate nerve agents, such as parathion, have been shown to detect ultra-trace concentrations of organophosphorus compounds using the enzyme acetylcholinesterase¹⁵⁷. The magnitude of the photonic stopband red-shift was directly linked to parathion concentration in aqueous solutions arising from a swelling of the hydrogel network when the parathion molecules bind to the enzymes in the hydrogel. Glucose monitoring in polyacrylamide-polyethylene glycol hydrogel designs was achieved through a blue-shift in the photonic stopband arising from increased hydrogel crosslinking related to the formation of a supramolecular complex created by glucose molecules self-assembling boronic acid and polyethylene glycol function groups on the hydrogel surface¹⁶¹. Monitoring glucose levels is an important aspect of managing diabetes, with further works proposing non-invasive methods of monitoring of glucose in human tear fluid^{158 162} and urine^{163 164} or a minimally invasive methods

using a microneedle wearable patch^{165 166} utilising this colorimetric hydrogel detection method. Figure 10 contains examples of the optical sensing capabilities associated with hydrogel PhC sensors.

There are many other emerging hydrogel PhC detection systems being researched with consistent innovation in the literature for a wide array of different detectable substances. Hydrogel PhCs have been developed as mechanochromic sensors with a colorimetric response to stretching or mechanical for use in wearable devices¹⁶⁷ or as underwater motion detectors¹⁶⁸. The range of specific chemical compounds which can be detected by PhC hydrogel networks is always expanding with new reports of hydrogen peroxide¹⁶⁹, aldehydes¹⁷⁰, alcohol concentration in beverages¹⁷¹ or for drug delivery¹⁷², thiol biomolecules¹⁷³ and adenosine in DNA¹⁷⁴ detection among recent works. Health-monitoring PhC hydrogel systems continue to be developed for detecting harmful residual antibiotics present in livestock milk¹⁷⁵, gram negative bacteria such as *E.coli*¹⁷⁶ or *Pseudomonas aeruginosa*^{176 177} present in milk or drinking water, alkaline phosphatase enzyme levels as a marker for liver or endocrine diseases¹⁷⁸ and metabolites such as L-kynurenine in blood as markers for immune suppressant disorders¹⁷⁹. Notably, all of these applications emphasise the importance of sensitivity of the photonic stopband response and the presence of the structural color of the PhC as a visual indicator for changes to the ordered system.

3 Photonic Crystals in Slow Light Generation and Photocatalysis

The photonic bandgap or stopband associated with structured PhC materials can inhibit the transmission of certain frequencies of light, but we can also exploit the interesting optical phenomenon of slow light propagation occurring at frequencies close to the photonic band edges. Compared to bulk or non-structured films, it is the specific presence of the photonic bandgap/stopband that introduces slow photon effect. For a simple definition, the slow photon effect is a reduction in the group velocity of light as the light increasingly approaches the properties of a standing wave at energies close to the photonic stopband¹⁸⁰. This reduction in the group velocity (v_g) of light can be visualised by a decrease in slope when approaching the bandgap/stopband in the dispersion relation diagram. Photonic band structure diagrams can be modelled for

different types of PhC designs with various refractive indices or material filling fractions to predict the existence and energies of photonic bandgaps/stopbands^{181 182 183}.

Figure 11 (a) displays band structure diagram for a TiO₂ IO, showing the existence of photonic stopband in the $\Gamma - L$ direction, spanning the approximate wavelength range 380 – 450 nm¹¹². These band structure diagrams illustrate the allowed photon energies ($\omega(k)$) at different wavevectors (k). For light propagating through an isotropic, non-structured material, the dispersion relation can be written as¹⁸⁴;

$$\omega(k) = \frac{c_0}{n} |k| \quad (4)$$

The group velocity at any point on these band diagrams can be found as:

$$v_g = \frac{\partial \omega}{\partial k} \quad (5)$$

The bending of the photonic band structure to accommodate for the photonic bandgap/stopband frequency range creates frequencies where the magnitude of this derivative is reduced, introducing the slow photon effect. The changes to the dispersion relation bands arising from a simple 1D PhC slab are shown in Fig. 11 (b)¹⁸⁴.

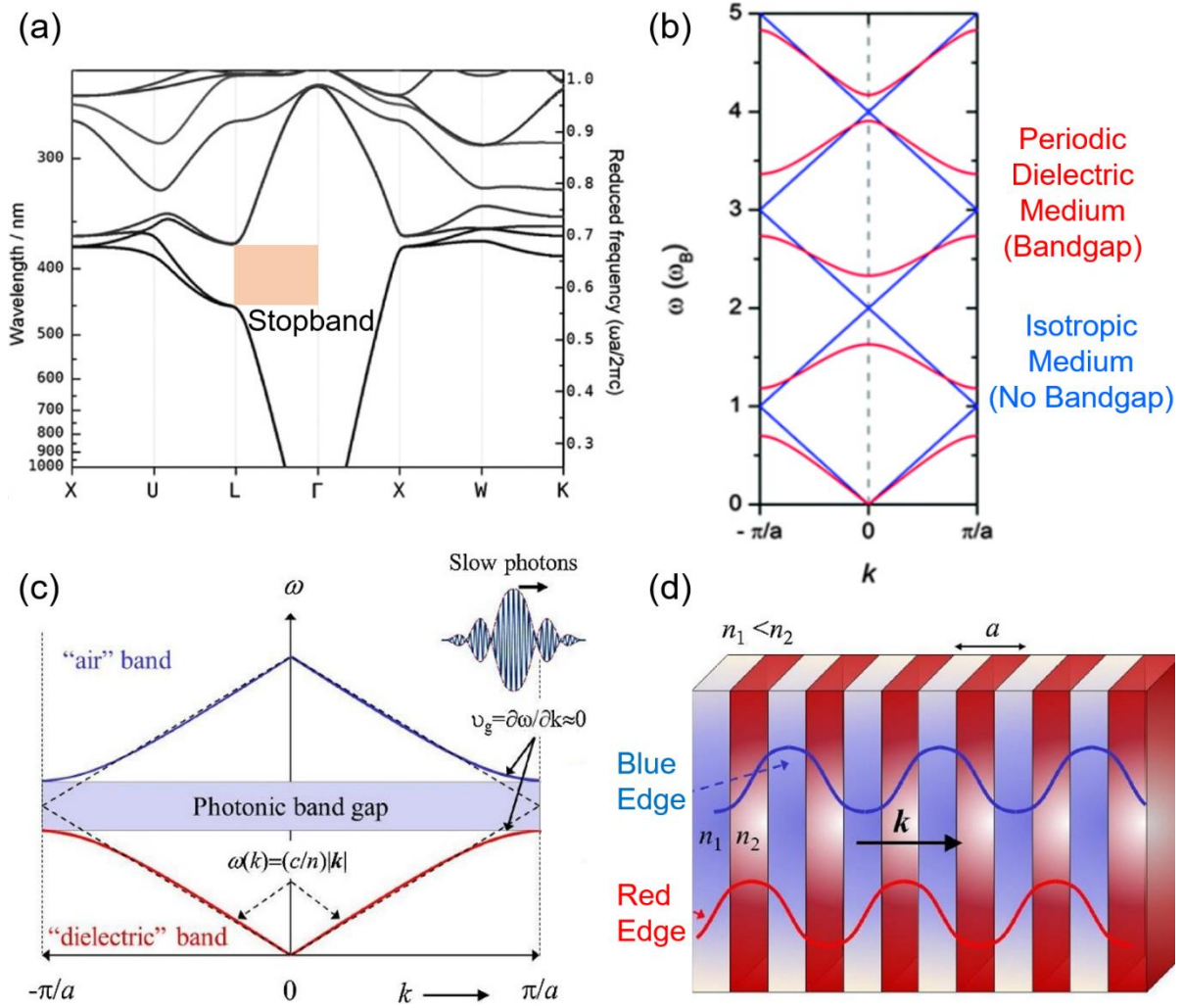


Fig. 11 (a) Photonic band structure for a TiO₂ IO in air¹¹² with spherical cavities of diameter 180 nm and $n = 2.5$ for TiO₂. The stopband in $\Gamma - L$ direction ([111] direction) is highlighted. Adapted from ref¹¹². Copyright 2015, American Chemical Society. (b) Simulated dispersion relation bands showing photonic bandgap formation in a 1D PhC with material slabs of thickness 200 nm and alternating refractive indices of 1 and 3.5 for a periodic dielectric (in red) compared to an isotropic slab with artificial periodicity (in blue)¹⁸⁴. Adapted from ref¹⁸⁴. Copyright 2013, Royal Society of Chemistry. (c) A photonic bandgap in the dispersion relation diagram for a 1D PhC illustrating the reduction to the group velocity at the band edges¹⁸⁵. Adapted from ref¹⁸⁵. Copyright 2018, Elsevier. (d) Schematic representation of light localisation in a 1D PhC slab ($n_2 > n_1$) showing a localisation in the higher index region at the red-edge and vice-versa¹⁸⁵. Adapted from ref¹⁸⁵. Copyright 2018, Elsevier.

The reduction in the group velocity, as shown in the dispersion diagram, creates a scenario where the light, which is quickly approaching a standing wave, becomes more strongly localised in different dielectric regions of the material¹⁸⁰. Slow light effects appear at either edge of the photonic bandgap/stopband region and the dispersion bands are often referred to as a dielectric (red edge) and an air (blue edge) band¹⁸⁵, as shown labelled in Fig. 11 (c). With the slow photon effect, it is thought that the maximal amplitudes of the standing wave become more localised in different dielectric media when approaching from the red edge compared to

the blue edge. Stronger localisation of the light in the higher dielectric material is anticipated for the red edge of the photonic bandgap/stopband^{180 185 186}. Conversely, light localisation for the lower dielectric material (air) is expected at the blue edge. A schematic representation of this effect can be seen in Fig. 11 (d).

For PhC materials, the group velocity attenuation is dependent on the magnitude of the contrast between the dielectric materials, the structural quality and thickness of the film¹⁸⁶. The slow photon effect in photon crystal materials has attracted much attention for applications where reduced group velocities and a targeted localisation of light in specific materials is beneficial, particularly in photocatalysis applications. The direct relationship between photonic bandgap/stopband position and the slow photon effect allows the frequencies of the slow photon region to be tuned alongside the photonic bandgap/stopband, as depicted in Fig. 12.

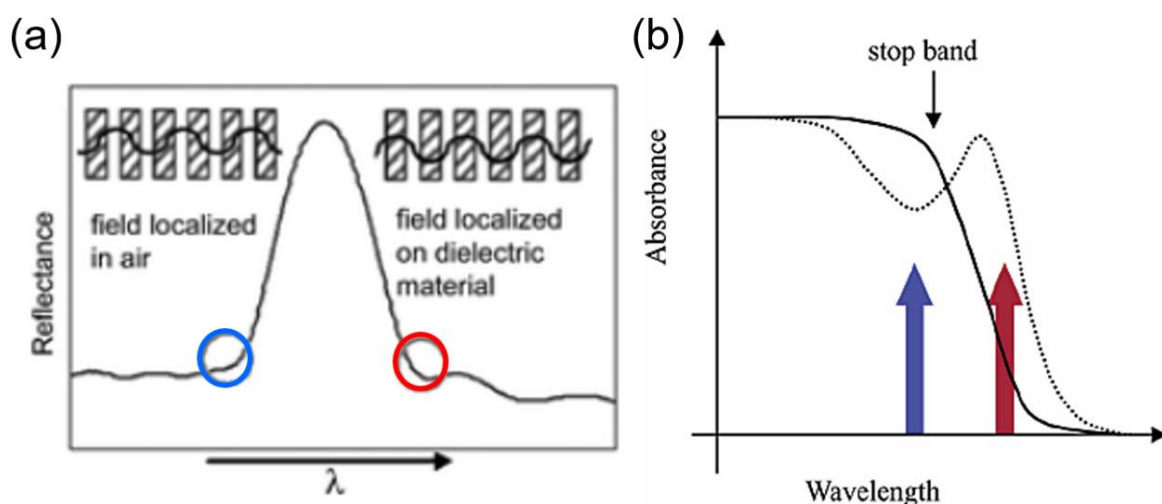


Fig. 12 (a) A schematic diagram showing the blue and red-edge slow photon regions surrounding a photonic bandgap region¹⁸⁶; slow photon frequency ranges are directly related to the photonic bandgap position. Adapted from ref¹⁸⁶. Copyright 2008, Royal Society of Chemistry. (b) Schematic representation illustrating the effect of blue and red-edge slow photon regions on the absorbance of a semiconductor photocatalyst¹⁸⁰. Standing wave localisation in the high index semiconductor material at the red-edge is shown to increase absorbance. Adapted from ref¹⁸⁰. Copyright 2003, American Chemical Society.

Photocatalysts are materials used in light-generated photochemical reactions where the photocatalyst (typically a semiconductor material) will generate reactive oxygen species stemming from electron-hole formation under light illumination. The photo-catalysed production of reactive oxygen species from the semiconductor acts to facilitate rapid reactions with other species in the reaction vessel¹⁸⁷. Major sectors where photocatalytic applications are explored are environmental waste/pollutant degradation^{188 189 190 191 192},

microbial disinfection^{193 194 195} and solar-fuelled energy production^{196 197 198 199 200}. A suitable electronic bandgap is a pre-requisite condition on the properties of semiconductors used as photocatalysts; redox potentials for the formation of reactive oxygen species and the evolution of hydrogen and oxygen from water should lie within the electronic bandgap of the semiconductor²⁰¹.

TiO₂ is one of the most prominently used semiconductors in photocatalysis owing to a combination of its suitable bandgap, relative abundance, low cost, stability, insolubility in water and nontoxicity^{190 201}. The basic operational principle for any photocatalytic material is the absorption of light at energies above the bandgap of the semiconductor, forming electrons and holes. Photo-excited electrons promoted to the conduction band can react with oxygen species to form superoxide/hydroperoxide radicals and photo-generated holes in the valence band can oxidise water or hydroxyl groups to create hydroxyl radicals²⁰². These reactive oxygen species act to degrade other species present in the vessel, such as environmental pollutants, through oxidation and decomposition. Figure 13 (a) displays a simple mechanism for photocatalysis oxidation and reduction reactions in a material such as TiO₂ with a bandgap below 390 nm²⁰³.

Although TiO₂ is widely used as photocatalyst on merit of its material properties, certain aspects of its semiconductor performance limit its ability for photocatalysis. Visible light-activated (VLA) photocatalysis relates to photocatalytic material designs which harvest the solar spectrum for catalytic reactions. The large bandgap of rutile TiO₂ (3.2 eV) and anatase TiO₂ (3.0 eV) requires UV light excitation for electron-hole generation; less than 5% of the solar flux incident on the earth's surface is located within this spectral range²⁰¹. Rapid charge recombination rates between photo-generated electron-hole pairs limits the quantum efficiency of photocatalytic processes in TiO₂²⁰². Several strategies have been utilised by researchers in an attempt to move towards VLA photocatalysis by tuning the bandgap of TiO₂ towards the visible range, enhancing the absorption of the semiconductor in the visible range or suppressing the electron-hole recombination rate which limits the quantum efficiency.

Dye-sensitised photocatalysis relates to organic dyes acting as sensitizer molecules on the surface of the semiconductor, enabling absorption of visible light wavelengths by the dye molecules and the transfer of electrons from the dye molecules to the conduction band of the semiconductor. Colored, toxic organic dyes in

wastewater, originating from industry sources like textile coloring²⁰⁴, can be self-sensitising by creating pathways for their own photocatalytic degradation under visible light²⁰⁵. To enhance the performance of TiO₂ as a photocatalyst, other semiconductors have been interfaced with TiO₂ forming heterojunctions²⁰⁶ which can act to limit charge recombination²⁰⁷ and increase visible photocatalytic activity²⁰⁸ for correct choice of material. Noble metal nanoparticles with a surface plasmon resonance such as Au²⁰⁹ and Pt²¹⁰ incorporated on the surface of semiconductors have shown reports of increased photocatalytic activity attributed to electron injection from the metal to the semiconductor, effectively inhibiting charge recombination rates and extending the absorption of the system into the visible range²¹¹. Non-metals such as nitrogen²¹², sulfur²¹³ and carbon²¹⁴, have been explored as dopants for semiconductors as TiO₂ with reports of enhanced visible light photocatalysis. Schematic diagrams representing the mechanisms behind photocatalyst semiconductor modifications can be seen in Figs. 13 (b), (c) and (d) for dye-sensitisation²¹⁵, heterojunction²⁰⁶ and metal nanoparticle modifications²¹⁶, respectively.

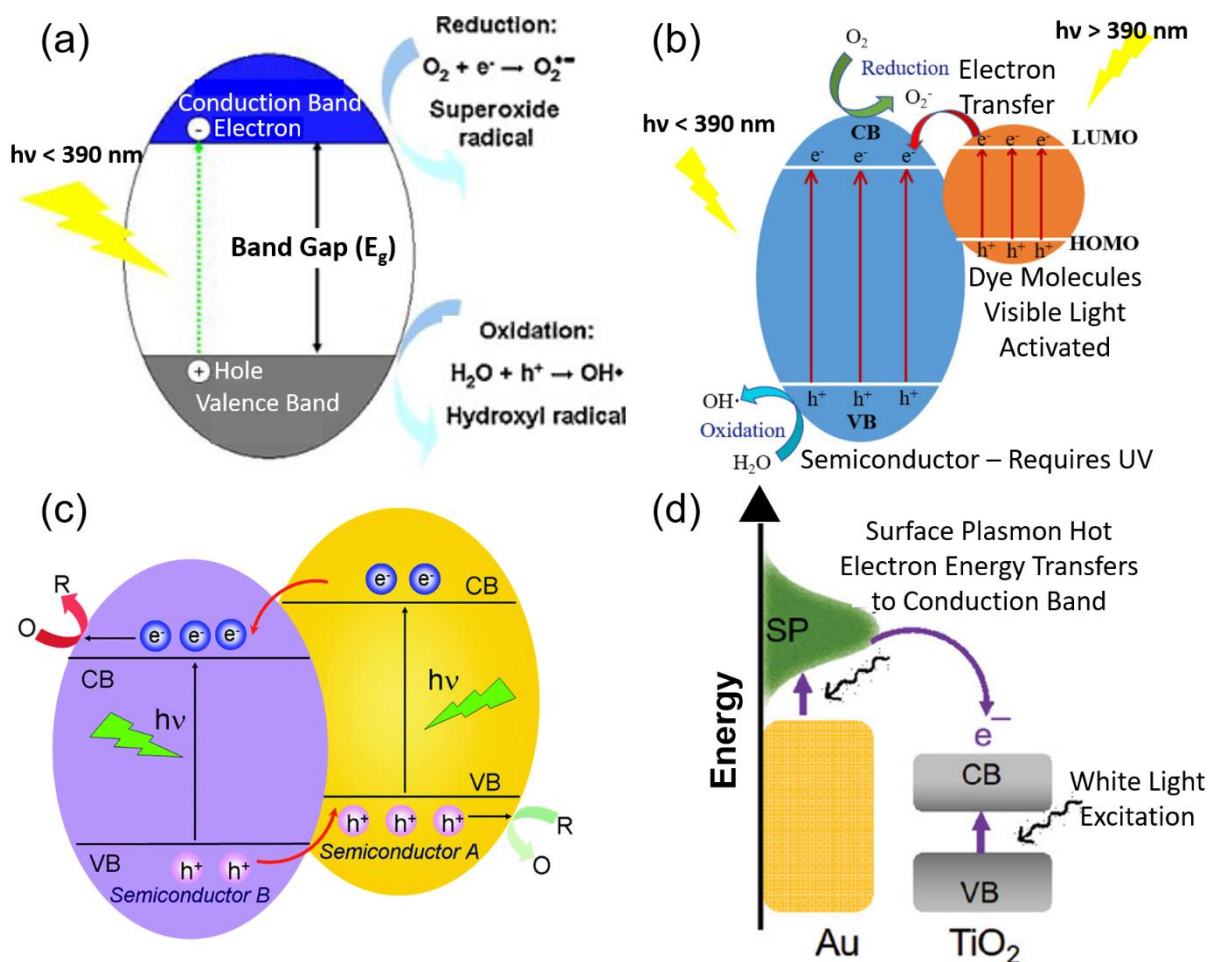


Fig. 13 (a) Mechanism of photocatalysis oxidation and reduction reactions for a semiconductor photocatalyst with an electronic bandgap in the UV²⁰³. Adapted from ref²⁰³. Copyright 2012, Elsevier. (b) Dye-sensitized photocatalysis mechanism showing visible excitation of dye molecules for a semiconductor with a wider bandgap²¹⁵. Adapted from ref²¹⁵. Copyright 2020, MDPI. (c) Semiconductor heterojunction showing the differences in bandgap energies and the flow of charges between valence and conduction bands for improved charge separation²⁰⁶. Adapted from ref²⁰⁶. Copyright 2014, Royal Society of Chemistry. (d) Schematic diagram of gold metal nanoparticles on a TiO₂ semiconductor²¹⁶. The localised surface plasmon resonance of the metal nanoparticles allow electrons generated in the visible region to enter the semiconductor conduction band. Adapted from ref²¹⁶. Copyright 2020, Wiley-VCH.

IO PhC designs are frequently used in photocatalytic systems. The structural porosity and higher effective surface area of IOs makes them attractive candidates for photocatalysts with reports of improved photocatalytic performances arising due to the effects of the structure^{211 217}. The optical effects associated with IOs, in particular the slow photon effect, has generated a lot of interest in photocatalysis research. As a controllable optical effect largely dependent on the structural size, the slow photon effect is often investigated in combination with other strategies, as described above, to enhance the photocatalytic performance of materials through a synergistic response^{218 219 220 216}. The reduced group velocity of light accompanying the slow photon effect is a desirable quality in photocatalysis; a decrease in group velocity leads to an increase in the effective optical path length of light which enhances light-matter interactions in the structure¹⁸⁶. Extending

the active range of frequencies for photocatalytic semiconductor materials through engineered slow photon effects is also a possibility with IO designs. At first glance, it may seem counterintuitive to associate photocatalytic enhancement (improved or extended light-matter interactions) with a PhC material which acts to reflect light from a surface. A common strategy is to engineer the photonic bandgap/stopband frequency to coincide with regions of high absorption in the semiconductor, effectively suppressing the photonic reflection, while simultaneously locating the slow photon region in a spectral region of interest for enhancement^{112 185}.

For slow photon photocatalytic enhancement in IOs, some of the earliest investigations were focused on slow photon amplified dye-sensitised systems^{180 221}. Dye-sensitised degradation of methylene blue on an anatase phase TiO₂ IO was investigated by varying the size (tuning the photonic stopband) of the IO periodicity and also the angle of the incident light, effectively shifting the slow photon region between different samples²²¹. The largest enhancement factors for the photocatalytic degradation occurred when the slow photon red-edge overlapped with the incident monochromatic radiation, as seen depicted in Fig. 14 (a). A separate study found that matching the absorption peaks of organic dyes such as methylene blue, rhodamine B and methyl orange to the stopband regions of various TiO₂ IOs enhanced the photocatalytic activity of the system under solar light illumination²²². The slow photon effect is credited with the enhancement of the dye-sensitisation, as seen from the increased kinetic constants in Fig. 14 (b).

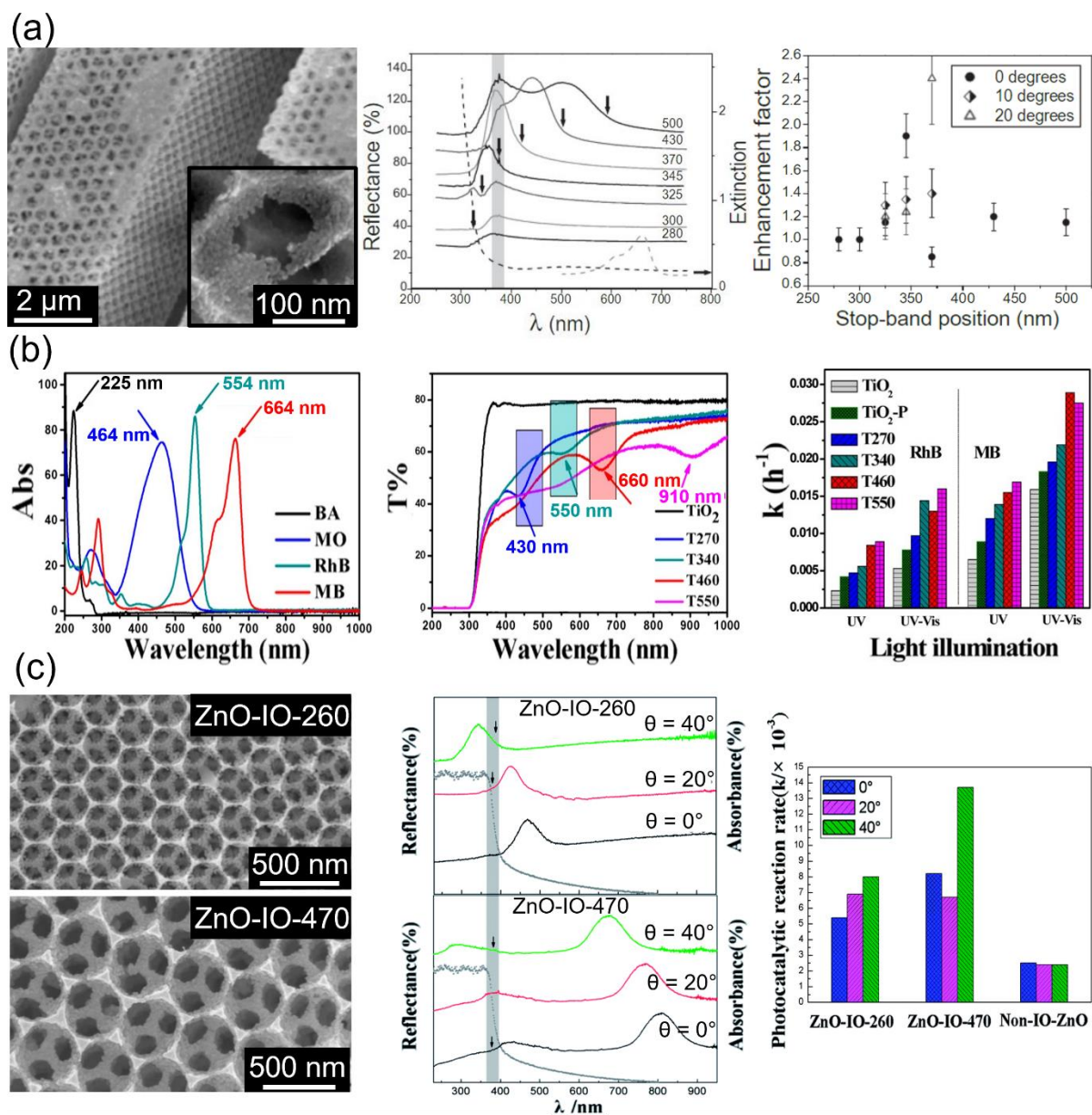


Fig. 14 (a) Dye-sensitised photocatalysis with slow photon effects for the photocatalytic degradation of methylene blue on TiO₂ IOs²²¹. The reflectance spectra of TiO₂ IOs, showing the stopbands, the red-edge of the slow photon regions (arrow) and the absorption region of TiO₂ are highlighted. The photocatalytic enhancement factor is highest under 370 nm illumination for an overlapping slow photon effect. Adapted from ref²²¹. Copyright 2006, Wiley-VCH. (b) Dye-sensitised photocatalysis, matching the peak absorbance of organic dyes with the slow photon effect of TiO₂ IOs²²². The stopbands of IOs are matched to the peak absorbance of methyl orange (MO), rhodamine B (RhB) and methylene blue (MB). For RhB and MB, overlapping the absorbance with slow photon effects are shown to give greater reaction rates in the UV-Vis. Adapted from ref²²². Copyright 2013, American Chemical Society. (c) Dye-sensitised degradation of rhodamine B on ZnO IOs²²³. The reflection spectra show the variable angle used to align the slow photon effect with the electronic absorbance of ZnO (shaded region). The photocatalytic reaction rate is shown highest upon overlap with the red-edge of the slow photon region. Adapted from ref²²³. Copyright 2014, Royal Society of Chemistry.

Outside of TiO₂ other IO materials report similar slow photon enhancement effects. A ZnO IO was found to present the highest photocatalytic reaction rate for dye-sensitised rhodamine B photocatalysis when the red-edge of the photonic stopband overlapped with the ZnO electronic absorption band²²³ at higher angles

of incidence. For the ZnO IO, the slow photon effect at the red-edge of the photonic stopband outperformed the blue-edge, as seen depicted in Fig. 14 (c).

Hybrid structures of SnO₂ IOs coated with nanocrystalline TiO₂ layers reported the highest rates of photocatalytic degradation of rhodamine B when the photonic stopband of the SnO₂ IO closely matched the electronic bandgap of TiO₂²²⁴. A heterostructure design of a TiO₂ IO infiltrated with 10 nm Cu₂O nanocrystals reported an increase in the photocatalytic degradation of rhodamine B and bisphenol A under UV-visible wavelengths when the slow photon region overlapped with the optical absorption of the Cu₂O nanocrystals²²⁵, as shown in Fig. 15 (a). Increased photocatalysis in this case was attributed to the synergy of the increased charge separation resulting from the heterostructure and the slow photon effect enhancing the light harvesting of the system. Similarly, a heterostructure of an SnO₂ IO with CdS quantum dots deposited uniformly over the surface of the IO reported increased rates for the removal of carbamazepine²²⁶, again attributed to a combination of the heterostructure and the slow photon effect as seen in Fig. 15 (b).

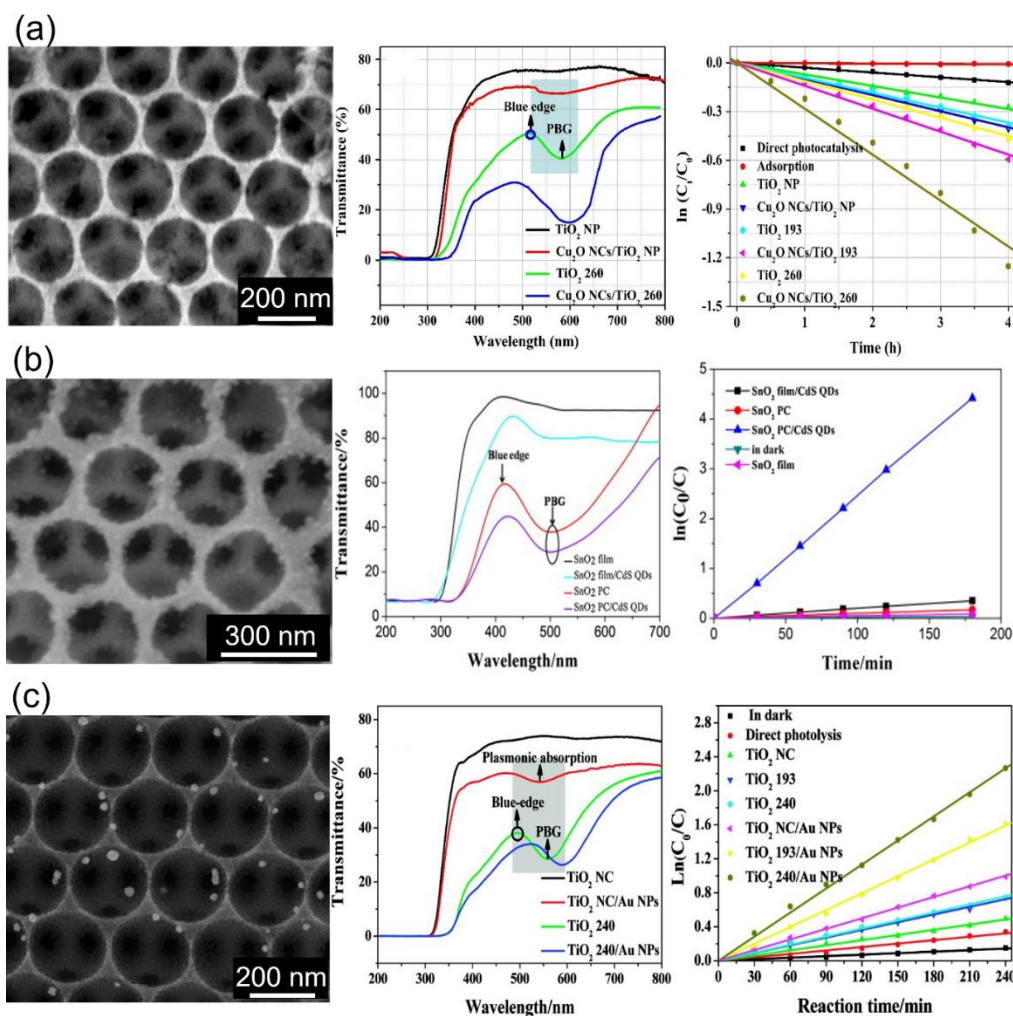


Fig. 15 SEM images, transmission spectra and measured photocatalytic degradation kinetics for synergistic slow photon effects with other semiconductor modification methods. (a) For a TiO₂ IO with a Cu₂O heterojunction, the highest degradation kinetics for bisphenol A occurs for overlap of the Cu₂O visible absorption with the blue-edge of the IO slow photon effect²²⁵. Adapted from ref²²⁵. Copyright 2015, Elsevier. (b) In a SnO₂ IO with a CdS quantum dot heterojunction, the photocatalytic degradation kinetics for carbamazepine were highest for an overlap of the blue-edge of the slow photon effect with the absorption of the CdS quantum dots²²⁶. Adapted from ref²²⁶. Copyright 2014, Elsevier. (c) For plasmonic Au nanoparticles deposited over a TiO₂ photocatalyst, the plasmonic absorption of the Au particles was amplified by the blue-edge of the slow photon region yielding increased degradation kinetics for 2,4-dichlorophenol²¹¹. Adapted from ref²¹¹. Copyright 2012, American Chemical Society.

The photocatalytic synergy between noble metal modification of semiconductors and the slow photon effect has also been explored. 2.3 wt% of Pt nanoparticles deposited on the surface of a TiO₂ IO demonstrated an enhancement of the photo degradation efficiency of acid orange by a factor of four²¹⁸. Neither the slow photon effect from the IO structure or the enhanced charge separation from the Schottky barriers at the TiO₂-Pt interface alone was sufficient to achieve this enhancement; the cooperative effects were needed to record the greatest enhancement factor. For improved performances in the visible spectrum Au nanoparticles have been deposited on TiO₂ IOs for photocatalytic degradation of 2,4-dichlorophenol using a combination of the

TiO₂-Au heterojunction for charge separation, the slow photon effect of the IO and the increased light absorption in the visible from the localised surface plasmon resonance of the Au nanoparticles²¹¹. This combination effect can be seen from the data depicted in Fig. 15 (c). These strategies for enhancing the photocatalytic performance of semiconductors through a combination of the slow photon effect with other existing methods are currently of great interest for photocatalysis research.

Recent works with visible light and Au nanoparticles incorporated onto ZnO^{219 227} or V₂O₅²¹⁶ IOs are further examples exploring this synergy of photocatalytic effects. The placement of Au particles in TiO₂ IOs and the role of slow photons in synergistic photocatalytic effects has also been studied²²⁸. Many emerging slow photon works focus on IO heterostructures, where two semiconductor materials are placed in contact to improve light harvesting effects in conjunction with slow photon effects. For photocatalytic CO₂ reduction, a rhenium-doped TiO_{2-x}/SnO₂ IO heterostructure²²⁹ and CeO₂ nanolayers supported by a TiO₂ IO²³⁰ have been investigated. Similarly, a TiO₂/graphitic-C₃N₄ IO heterostructure showed an enhanced performance for rhodamine B degradation²³¹ and Bi₂WO₆/WO₃ IO heterostructures with graphene quantum dots enhanced phenol degradation²³². Recent prevailing opinions^{233 234 235 236} emphasise that high quality, structurally scalable and mechanically stable inverse opal films with a strong optical signature are crucial for maximising the slow photon effect. It has even been suggested that higher order slow-light modes found only in high quality TiO₂ IO films may be more efficient at light trapping than traditional red and blue-edge of the photonic bandgap²³⁴.

4 Photonic Crystals in Solar Cell Devices

Solar cell devices operate under the principle of photovoltaic energy conversion under which electromagnetic radiation is converted into electrical energy. The process of electrical energy conversion can be described as light absorption by an absorber material creating a transition from ground to excited state, production of an electron and hole from this transition, charge migration of the electron through an external circuit from cathode to anode and recombination of the electron with a hole to return the absorber to the ground state²³⁷. Thick,

crystalline silicon-based solar cells have been the dominant photovoltaic devices in solar cell technology for quite some time. Silicon solar cells are popular due to the abundance of silicon available in the earth's crust, the non-toxicity of the material, the proven efficiency and stability of the technology and the semiconducting properties of silicon were widely studied.

Limitations on conventional silicon solar cells are known and were predicted^{238 239}; the indirect bandgap of crystalline silicon necessitates thick layers of silicon for efficient cells and the high associated cost of manufacturing thick layers of crystalline silicon created an economic impediment. Research trends in solar cells have been focused on driving production costs down, minimising energy usage and environmental CO₂ emissions²⁴⁰ from crystalline silicon production while attempting to preserve or improve on the efficiencies of the silicon solar cell. Thin-film silicon solar cells²⁴¹, thin films of alternate materials like cadmium telluride or copper-indium diselenide²⁴², organic solar cells²⁴³, perovskite solar cells²⁴⁴, and dye-sensitised solar cells²⁴⁵ are among some of the alternative classes of solar cell being researched for future implementation^{246 247 248}. Here, we discuss the role of PhC materials, specifically their optical properties, which have been used to enhance the performance of certain classes of solar cell.

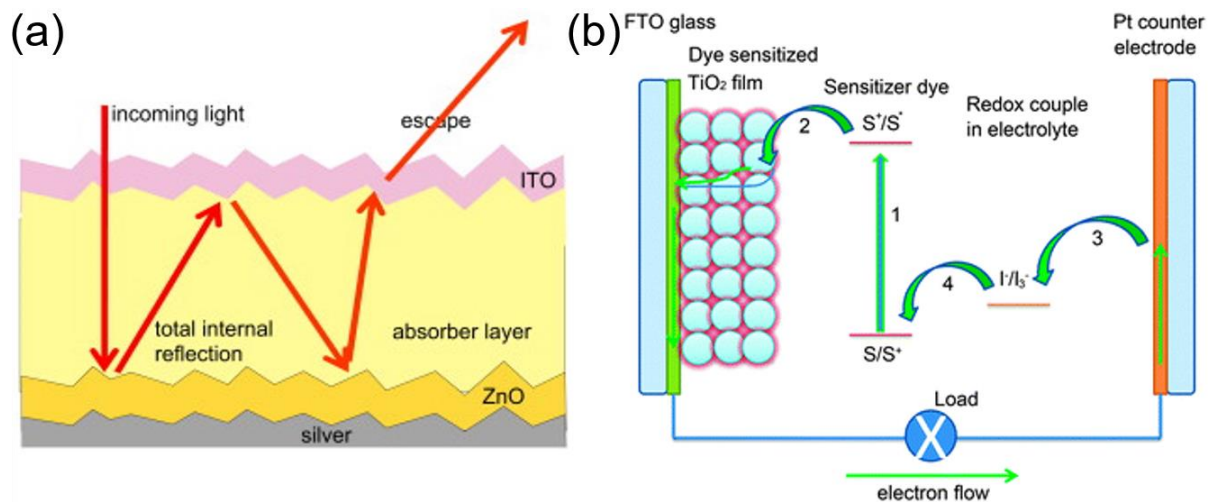


Fig. 16 (a) Schematic diagram showing typical modifications made to layers in a thin film solar cell, including textured surfaces for light scattering and a metal back reflector, to increase the path length and absorption probability of light in the cell²⁴⁹. Adapted from ref²⁴⁹. Copyright 2014, Elsevier. (b) Schematic diagram depicting the electron transfer processes in a dye-sensitized solar cell for a TiO₂ film sensitized with dye molecules versus a Pt counter electrode²⁵⁰. Adapted from ref²⁵⁰. Copyright 2013, Royal Society of Chemistry.

Thin film solar cells have been researched as alternatives to the thicker crystalline wafer silicon solar cells. Hydrogenated amorphous silicon (a-Si:H) and hydrogenated microcrystalline silicon ($\mu\text{c-Si:H}$) are common examples of silicon thin films used in these solar cells; the thin films of these materials offer the potential advantages of cost reduction in material preparation and are much quicker to pay back the energy input required to fabricate these devices²⁵¹. Direct bandgap semiconductors like cadmium telluride or copper-indium selenide species feature much larger absorption coefficients allowing for higher absorption of incident photons over a shorter distance, such as a thin film²⁵². Amorphous semiconductors with an indirect bandgap (such as a-Si:H) tend to feature larger absorption coefficients²⁵³ when compared to their crystalline counterparts due to the structural disorder in the amorphous material relaxing the quantum mechanical selection rules for absorption²⁵¹. In spite of a larger absorption coefficient, amorphous silicon features a wider bandgap ($\sim 1.7 - 1.9$ eV for a-Si:H) compared to crystalline forms of silicon (~ 1.1 eV), limiting the amount of the solar spectrum absorbed by the amorphous material²⁵⁴. Micromorph or tandem solar cells featuring heterojunctions of a-Si:H and $\mu\text{c-Si:H}$ have been developed to promote increased absorption at longer wavelengths and limit light-induced degradation of the amorphous material^{254 255}.

Increasing the absorption of the semiconductor material is key to improving the performance of thin-film solar cells. A widely used technique in thin-film solar cells is light trapping, which uses material or layer modifications to increase the path length of light in the absorbing material thereby increasing the probability of absorption^{256 257}. Light trapping techniques are essential for thin-film cells in particular as the absorbing layer is nominally short. The front surfaces of layers in the solar cell are often textured to promote scattering and total internal reflection effects which extend the path length of light in the material^{257 258}. Back reflectors, textured metal surfaces separated from silicon layers by a thin dielectric layer²⁵⁹, are also used to reflect incident light and create longer path lengths. Figure 16 (a) illustrates this effect where textured surfaces are utilised to confine light to the absorbing semiconducting layer. In thin film solar cells, PhCs find their application here by providing controllable and enhanced reflections from material layers to promote increased absorption.

A 1D PhC material of alternating dielectric layers of sputtered indium-tin oxide and SiO₂ layers has demonstrated potential for application in integrated photovoltaics, where semi-transparent solar cells for use in windows or skylights are designed using a back reflector of a conducting PhC in place of a metal layer for light trapping in thin-film cells²⁶⁰. The tunable reflections in the photonic structure can be modified by adjusting the layer thicknesses to selectively reflect specific wavelength ranges while transmitting the remainder of the spectrum for light or heating; in this case, wavelengths above the absorption edge of the a-Si:H thin-film were reflected to boost performance. The device structure and performance for these 1D photonic solar cell back reflectors can be seen in Fig. 17 (a)²⁶⁰. Another application involving alternating 1D PhC dielectric layers of silicon nitride and silicon oxynitride integrated into a crystalline silicon solar cell is based on aesthetically designing colored solar panels using the reflected wavelengths from the PhC for uses in smart design and green building²⁶¹. Red, blue, green and white solar cell panels were fabricated by adjusting the thicknesses of the dielectric layers deposited on the glass to tune the reflectivity of the photonic bandgap, as seen in Fig. 17 (b)²⁶¹.

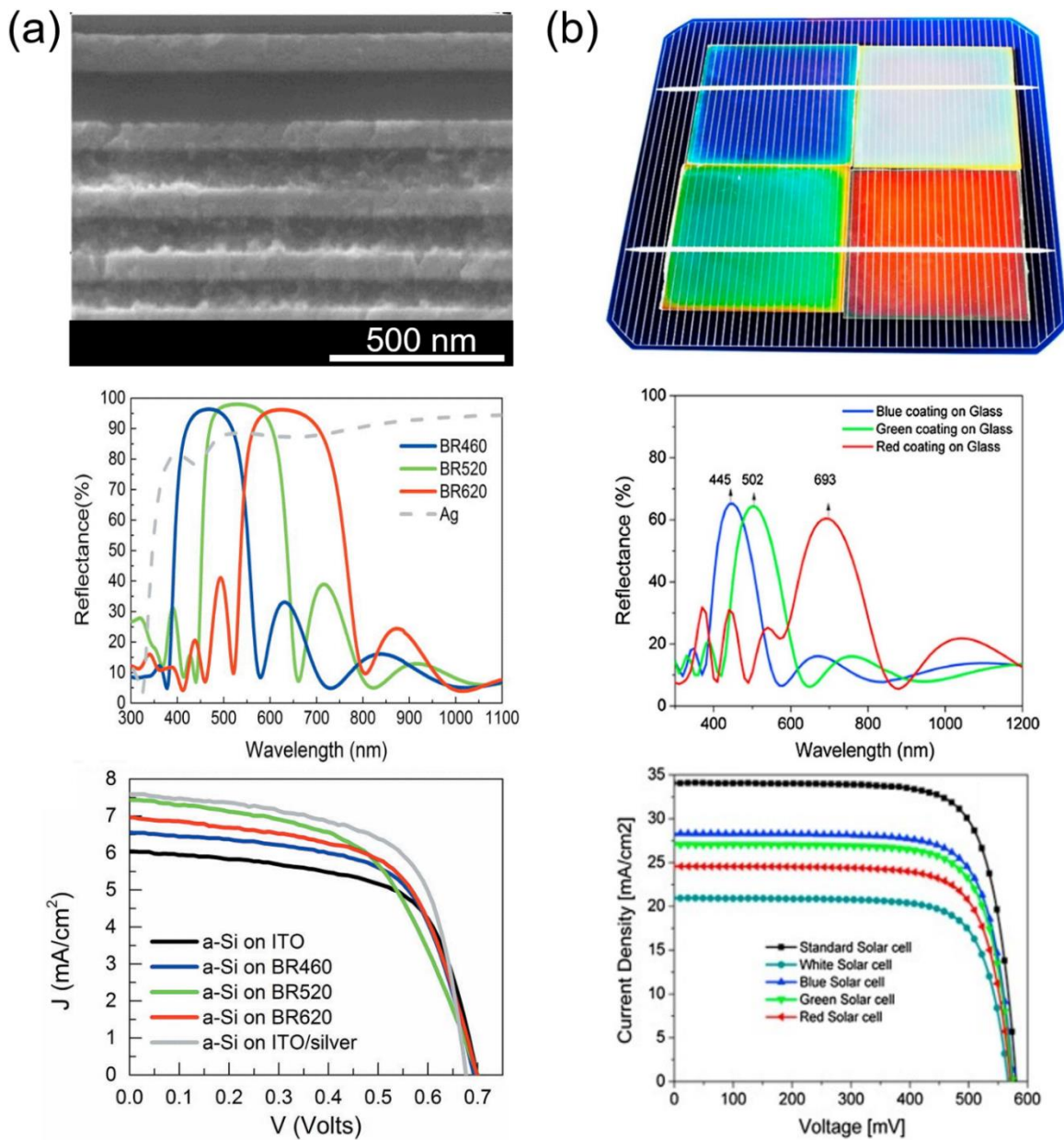


Fig. 17 (a) Design of a 1D PhC back reflector in a semi-transparent solar cell with alternating layers of indium-tin oxide and SiO₂. Peak reflections are shown for various PhC layer thicknesses alongside current densities for solar cells incorporating these designs²⁶⁰. Adapted from ref²⁶⁰. Copyright 2013, American Institute of Physics. (b) Aesthetic coloration for solar cell devices with visible transparency for non-reflective wavelengths based on a 1D PhC of alternating silicon nitride and silicon oxynitride layers. Peak reflections for different layer thicknesses are shown in addition to solar cell current densities for different designs²⁶¹. Adapted from ref²⁶¹. Copyright 2019, Elsevier.

3D PhCs in the form of silicon IOs have also been incorporated as back reflectors in crystalline silicon thin-film solar cells with a reported increase in the light trapping of the solar cell resulting from the IO back reflector²⁶². Photonic bandgap reflections, pseudogap regions, diffuse back scattering and surface diffraction effects in the IO material were all factors believed to contribute to the performance enhancement of the IO back reflector versus a back reflector of aluminium; the IO reflection could also be tuned to the near-IR region

where it is most needed for crystalline silicon solar cells. The IO back reflector solar cell was also combined with surface texturing, showing improved absorption using a combination of these effects as seen in Fig. 18 (a)²⁶².

PhC materials also find application in thin-film solar cells as intermediate reflector layers in tandem solar cells. Tandem solar cells often suffer from current mismatch between the absorbing layers in the solar cell and intermediate layers are often included in an attempt to equalise the current generated from each layer. In the case of a micromorph silicon tandem solar cell, the a-Si:H top layer emits a lower current compared to the $\mu\text{c-Si:H}$ bottom layer. This limits the overall efficiency of the solar cell and intermediate layers are included in an attempt to equalise the current generated by spectrally splitting and reflecting the spectrum²⁶³. A ZnO:Al IO in a tandem solar cell between a-Si:H and $\mu\text{c-Si:H}$ layers reported an enhancement factor of 3.6 in the external quantum efficiency of the limiting a-Si:H layer by acting as wavelength selective filter; high energy wavelengths were reflected back into the a-Si:H layer using the photonic bandgap and lower energy wavelengths were transmitted to the $\mu\text{c-Si:H}$ layer for absorption²⁶⁴. The IO intermediate layer was reported to outperform other intermediate layer materials such as thin-film based intermediate layers, the results of which can be seen in Fig. 18 (b).

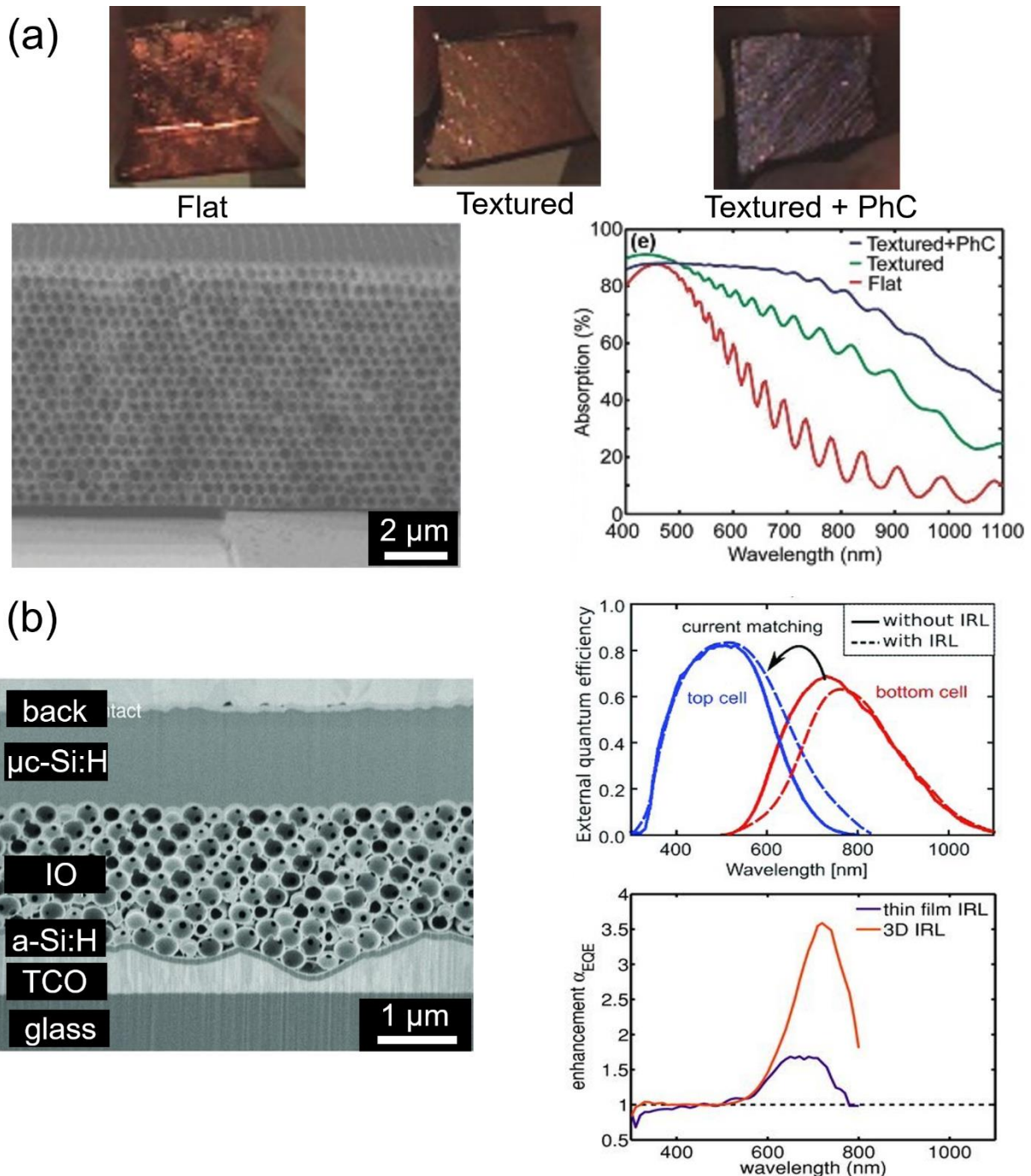


Fig. 18 (a) A 3D silicon IO used to enhance back reflection and light path lengths in a thin-film crystalline Si solar cell. A combination of surface texturing and PhC reflections were found to result in the highest solar cell absorptions²⁶². Adapted from ref²⁶². Copyright 2013, Wiley-VCH. (b) A tandem silicon micromorph solar cell with a ZnO:Al IO acting as a wavelength selective intermediate layer between a-Si:H and μ c-Si:H absorption layers. The current matching facilitated by the IO is shown via increased external quantum efficiency of the limiting top cell (a-Si:H) and an increased overall enhancement factor of the cell compared to other thin film layers²⁶⁴. Adapted from ref²⁶⁴. Copyright 2011, Wiley-VCH.

A separate class of solar cell devices which have seen an increased uptake of PhC materials are dye-sensitised solar cells (DSSCs). The operating principles of DSSCs are fundamentally similar to the dye-sensitised photocatalysis mechanism discussed in the Section 3. In DSSC systems, the production of electricity from light can be thought of in terms of a cycle of reactions as shown in Fig. 16 (b)²⁵⁰. Photoanodes, such as

mesoporous TiO₂, are deposited on transparent conductive substrates and sensitized with dye molecules to harvest light. A circuit is connected from the photoanode to a counter electrode, such as platinum coated conductive glass, and an organic electrolyte containing a redox couple, commonly I⁻/I³⁻, separates the electrodes²⁴⁵. Photo-excited electrons generated from dye absorption are transferred to the conduction band of the semiconductor, collected by anode, transported through an external circuit to perform work and arrive at the counter electrode. Sensitised dye molecules, after transferring electrons, are reduced by the electrolyte and in-turn the electrolyte absorbs the electrons which arrive at the counter electrode^{245 250}.

Unlike the photocatalysis reactions which act to degrade or eliminate dye molecules or other species in the reaction vessel, DSSCs operate by regenerating the dye species using an electrolyte and closed circuit such that no material is lost or converted and the cycle can continue to generate electricity. Compared to conventional crystalline silicon solar cells, DSSCs are cheaper, easier to fabricate, more flexible, feature a higher sensitivity to low intensity environments and have the potential to possess a low environmental impact with respect to material choices^{245 265}. Low efficiencies, long-term stability and material production costs of DSSCs hinder their economic viability²⁶⁵. The most successful DSSCs with highest efficiencies tend to feature Ru-bipyridyl compounds as sensitizer molecules which has a high associated cost, time consuming production steps and is a toxic material^{250 266 267} and presently natural alternatives do not offer comparably high efficiencies^{266 268}. For all manner of DSSCs research methods to improve efficiency of light absorption through cell design or material choice are an essential consideration. With regards to the photoanode material, methods to improve the light harvesting efficiency are based on increasing surface area, dye molecule pickup, reducing charge recombination, improving electron charge transport and increasing the light scattering ability to increase absorption^{245 269 270}.

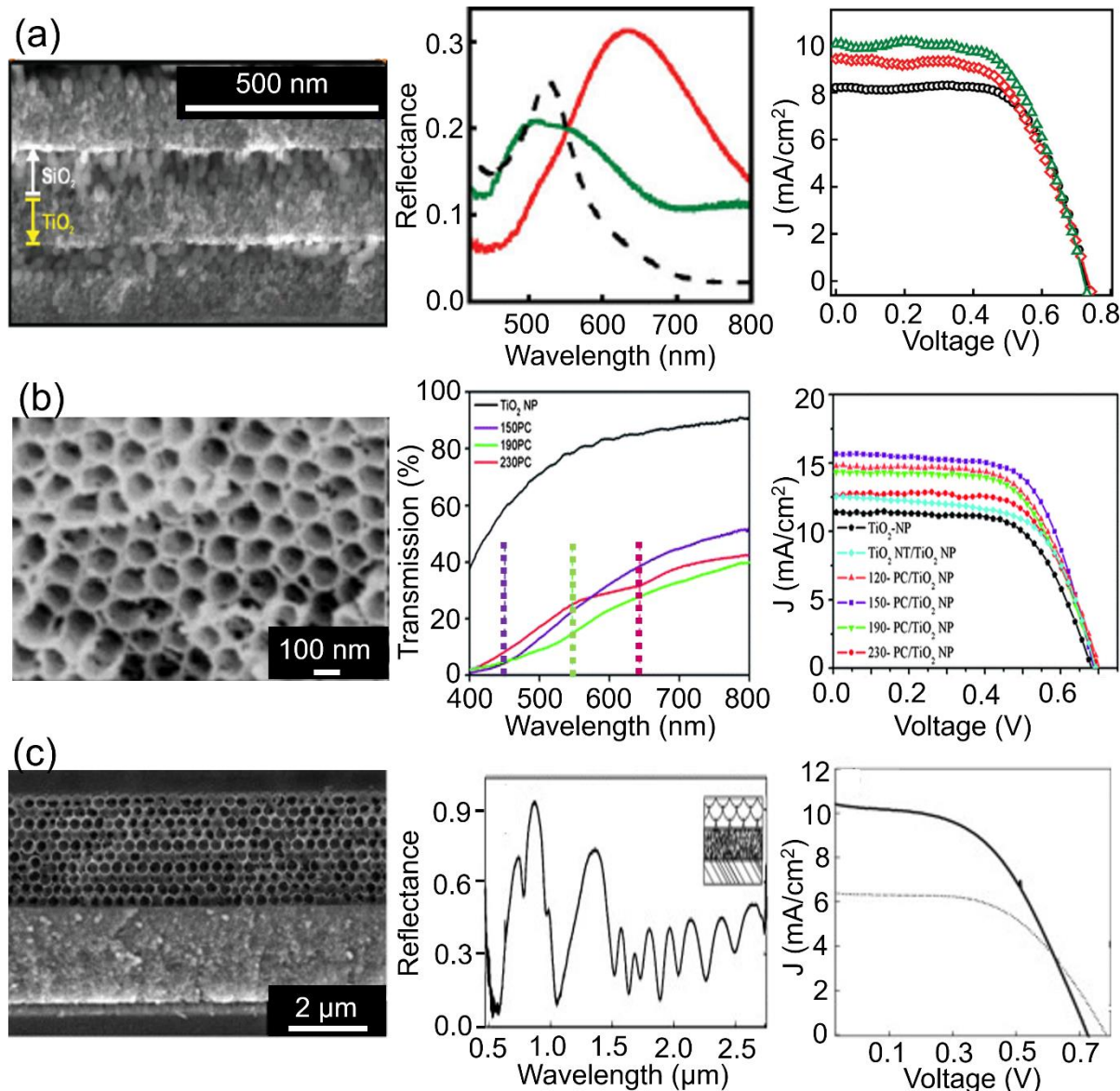


Fig. 19 (a) Porous 1D PhC layers deposited on a nanocrystalline TiO_2 anode in a DSSC. Reflectance spectra with photonic stopband maxima shown for two different PhC materials. Current density for both structures shown versus a DSSC with no PhC reflector²⁷¹. Adapted from ref²⁷¹. Copyright 2009, Wiley-VCH. (b) 2D PhC TiO_2 nanotube reflecting layer deposited on a TiO_2 nanoparticle layer in a DSSC. Transmission spectra for different nanotube sizes highlighting photonic stopband locations is presented alongside current densities showing enhanced performances for nanotube PhC layers²⁷². Adapted from ref²⁷². Copyright 2012, Royal Society of Chemistry. (c) A 3D silicon IO used as a reflecting layer in a DSSC atop a nanocrystalline TiO_2 anode with a reflectance spectrum of the silicon IO included. Larger current densities are observed for DSSCs including an IO reflecting layer²⁷³. Adapted from ref²⁷³. Copyright 2011, Wiley-VCH.

PhC materials find application in DSSCs as a means of promoting scattering and reflection effects for light incident on the photoanode. Typical photoanodes in TiO_2 DSSCs consist of a layer of mesoporous TiO_2 nanoparticles with a large surface area loaded with dye molecules. TiO_2 IOs with photonic stopbands in the visible range acting as the electrode in DSSCs were found to underperform compared to nanoparticle anodes, attributed to the superior dye loading ability of nanoparticle layers²⁷⁴; however, the potential of the IOs to act

as tunable dielectric mirrors to enhance dye absorption was highlighted. Different PhC configurations have been explored in conjunction with mesoporous TiO₂ electrodes to establish an improvement in the light harvesting ability of the photoanode using the optical properties of the PhC as a reflector or scattering region. Porous 1D PhCs, consisting of alternating layers of SiO₂ and TiO₂, deposited on the back surface of a nanocrystalline TiO₂ photoanode were shown to enhance power-conversion efficiency in DSSCs; the porous PhCs allowed the electrolyte to interact with dye molecules in the inner layer²⁷¹. Both 1D PhC materials with different photonic stopbands were found to provide an enhancement of the current density; the largest enhancement was achieved when the peak reflection of the PhC matched closest to the absorption band of the ruthenium dye, as seen in Fig. 19 (a).

Similar effects were observed with 2D TiO₂ nanotube PhCs prepared on the back surface of a dye-sensitised TiO₂ nanoparticle layer²⁷². All PhC nanotube structures were found to enhance the power-conversion efficiency when compared to non-PhC nanotubes or nanoparticle photoanodes fabricated at identical thicknesses; the enhancement effect was most pronounced for matching the PhC reflection with the maximum dye absorption²⁷². Figure 19 (b) displays the structure and performance enhancement of the nanotube PhC. 3D silicon IOs when successfully deposited onto nanocrystalline TiO₂ and ZnO nanowire electrode layers also demonstrated enhanced light-trapping in DSSC systems²⁷³. Reflections from the pseudo-photonic bandgap of the electrolyte infiltrated silicon IO enhanced the current density recorded for the DSSC, as observed in Fig. 19 (c). A large impediment to 3D PhC incorporation into a DSSC is the fabrication of high quality films on the mesoporous TiO₂ surface, though successful examples do exist in the literature^{273 275 276}. Multilayers of IOs with differing lattice constants and optical responses have also been suggested for further spectral light harvesting in DSSC systems²⁷⁷ with a two-layer IO system reporting an enhancement in a TiO₂ DSSC²⁷⁶.

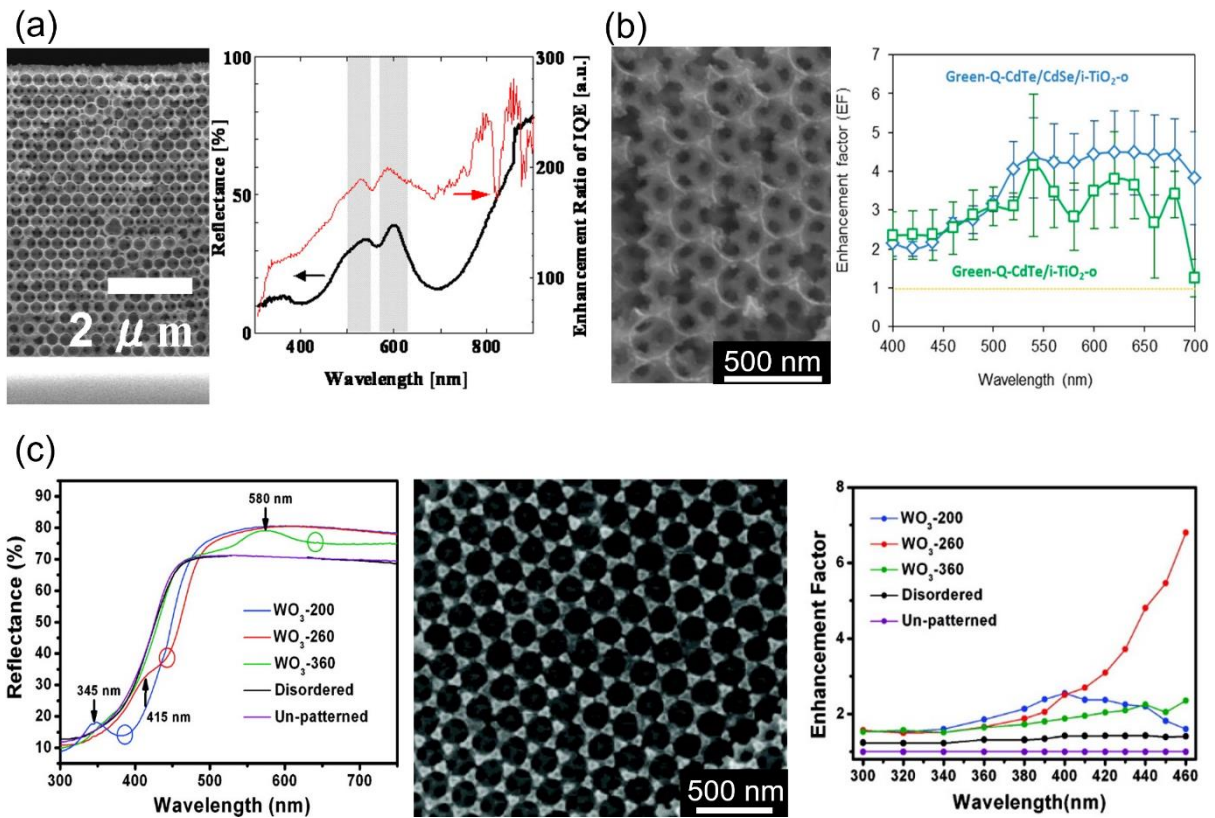


Fig. 20 (a) An inverse crystalline silicon opal showing reflectance (black line) and solar cell enhancement ratio (red line) with photonic bandgap reflections, slow photon edges and regions of enhancement highlighted as shaded regions²⁷⁸. Adapted from ref²⁷⁸. Copyright 2011, American Institute of Physics. (b) Enhancement factors of CdTe/CdSe (blue line) and CdTe (green line) quantum dot-sensitized TiO_2 IOs showing a 4-fold enhancement for slow photon effects overlapping with electronic absorption²⁷⁹. Adapted from ref²⁷⁹. Copyright 2020, American Chemical Society. (c) Reflectance spectra and solar cell enhancement factor for WO_3 IOs (sizes 200, 260 and 360) compared to disordered porous and unpatterned nonporous WO_3 . Slow photon effects for WO_3 -260 with the highest enhancement factor²⁸⁰. Adapted from ref²⁸⁰. Copyright 2011, American Chemical Society.

Finally, IO materials have also been explored in solar cell devices in order to exploit slow photon effects. The reduced group velocity of light at the photonic band edge has the potential to increase light-matter interactions, see Section 3 for more details. Inverse crystalline silicon opals treated with hydrogen plasma passivation demonstrated increases in the enhancement ratio of the internal quantum efficiency of the silicon solar cell at wavelengths close to the photonic bandgap and band edges²⁷⁸. This amplification in the photon-to-electron conversion efficiency around the photonic bandgap regions was attributed to slow light trapping effects, as seen in Fig. 20 (a). Large-area and high quality IO WO_3 photoanodes were found to exhibit large increases in the photon-to-electron conversion efficiency compared to disordered porous and unpatterned nonporous WO_3 electrodes²⁸⁰. Between the various IO sizes tested, the largest enhancement was observed when the red-edge of photonic bandgap overlapped with the WO_3 electronic absorption edge, as seen with the WO_3 -260 sample in Fig. 20 (c)²⁸⁰.

Quantum dot sensitised solar cells, where quantum dots are used as absorber sensitizers on semiconductor films, also feature reports of slow photon enhancement effects. TiO₂ IOs sensitized with quantum-confined CdSe films displayed a significant amplification of the photon-to-current conversion efficiency with an average enhancement factor of 6.7 ± 1.6 at 640 nm for an IO structure with a photonic bandgap at 700 nm compared to a nanocrystalline TiO₂ with similar CdSe sensitisation²⁸¹. This enhancement was attributed to a blue-edge slow photon effect overlapping with CdSe absorption edge (600 – 650 nm). More recently, CdTe/CdSe quantum dot sensitized TiO₂ IOs were shown to feature a 4-fold enhancement factor of the photon-to-current conversion, compared to nanocrystalline TiO₂ films, when the blue or red-edge of the photonic stopband was tuned to match the quantum dot absorbance edge²⁷⁹. Smaller gains in the enhancement factor were noted for quantum dot absorbance edges centred in the photonic stopband compared to blue or red-edge effects, heavily suggesting a slow photon amplification effect. Figure 20 (b) displays the slow photon enhancement factor for both CdTe/CdSe and CdTe quantum dots on TiO₂ IOs.

These are just some of the strategies combining the optical performance of PhC layers with the light harvesting capabilities of semiconductors materials and sensitizer molecules present in solar cell devices. Optically, the PhC layers in solar cells are often used to promote light absorption through targeted reflectance of specific wavelengths and improving the path length of light through the cell. Some recent works^{282 283 284} have attempted to determine the effects of the angular iridescence response of the photonic signature associated with PhCs on solar cell performance, simulating more realistic operating conditions with the changing position of the sun. Other works are focusing on the aesthetic capabilities of PhCs in solar cell devices with a wide range of tunable structurally colored designs options available for decorative purposes in solar cells which incorporate PhC layers^{285 286 287 288}. Solar cells featuring controllable PhC structural color are often explored as candidates for smart window designs^{261 289 290}. Current research trends appear point toward both a functional and aesthetic role for PhCs in solar cell devices.

5 Photonic Crystals in Waveguides and Optical Fiber Designs

Optical waveguides are structured materials designed to transport energies, typically in the visible or infrared regions, between a source and destination. Waveguides are designed to guide light based on how light interacts with different regions of the material. The theory and optics behind traditional optical waveguides are quite well understood²⁹¹. In general, a traditional optical waveguide will consist of a high refractive index core material, surrounded by a lower refractive index cladding, all encompassed by a protective jacket. Waveguides with this design are commonly called optical fibers.

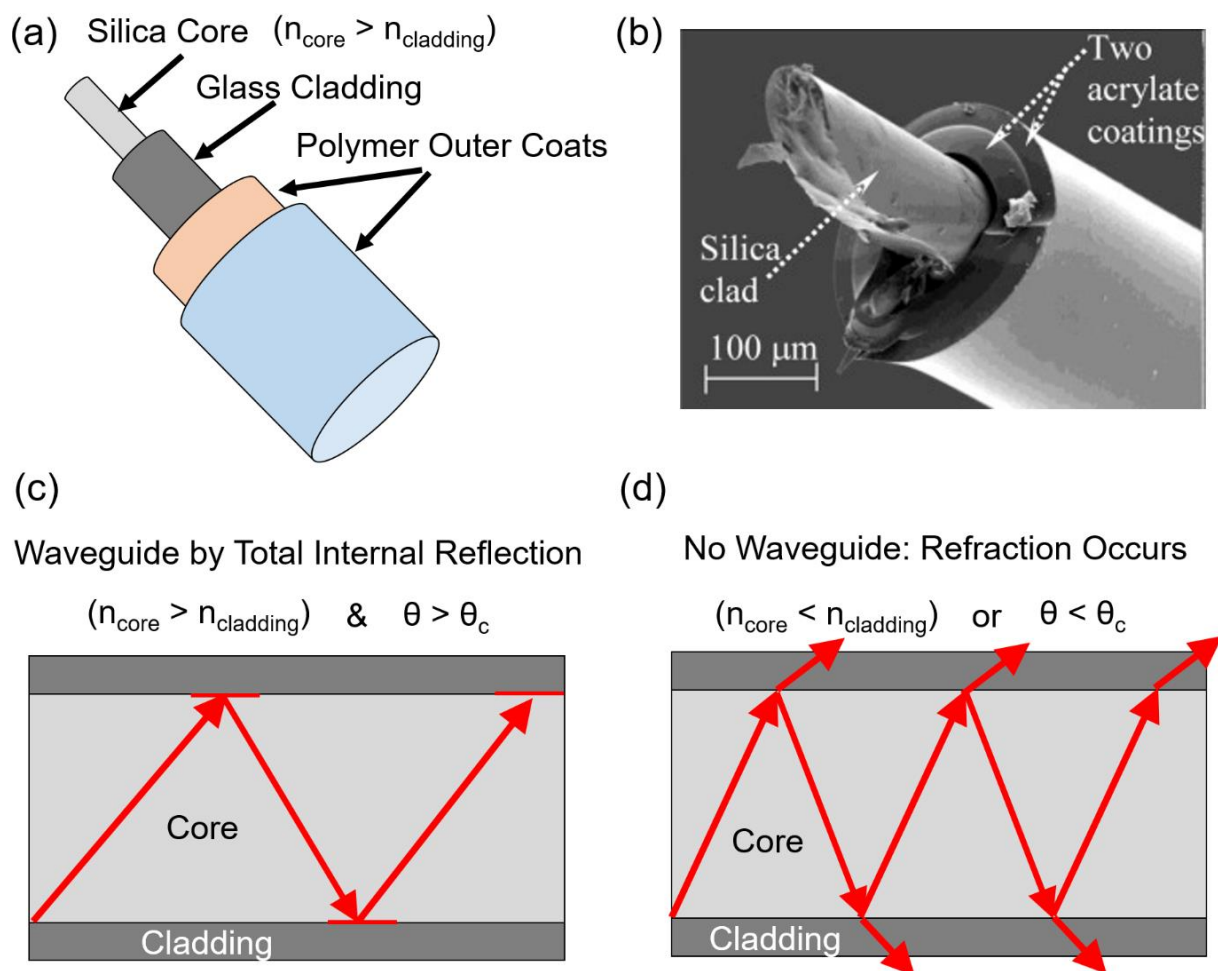


Fig. 21 Labelled components of a typical silica optical fiber design highlighting the core, cladding and protective outer coating materials for (a) a schematic diagram and (b) an SEM image of a used multimode silica fiber with two protective acrylate coatings²⁹². Reproduced from ref²⁹². Copyright 2015, Elsevier. Material constraints and light guiding mechanism in an optical fiber operating (c) as a waveguide where total internal reflection occurs for chosen refractive indices and propagating angle and (d) without a waveguide where light refracts through the cladding due to a lower core refractive index or angles smaller the critical angle.

Light is guided from one end of the fiber to the other using the principle of total internal reflection (TIR) between different refractive index regions of the fiber. The constraint of a high index core material is introduced from this mechanism of light guiding; waveguides relying on TIR confine light to the core region of the fiber only if TIR can occur i.e. the core refractive index must exceed the cladding refractive index. The angle at which the light enters the core region must also exceed the critical angle for TIR effects to be observed. The typical structure and waveguide mechanism for light in an optical fiber are shown in Figs. 21 (a) – (d).

Optical fibers are a widely used technology across many different fields of study. Flexible fibers are ideal for imaging internal organs in medicine^{293 294}, optical fiber lasers have been developed with doped cores to control the refractive index and photon absorption^{295 296} and optical fiber refractive index sensors and their applications were earlier discussed in Section 2. The most critical application of optical fiber waveguides is found in optical fiber communication technologies where nearly two billion kilometres of optical fiber are used for telecommunications and data transfer²⁹⁷. Internet connections and phone reception are dependent on high speed data transfer and the associated low cost of optical fibers. The conventional waveguide design by TIR is not without its challenges. Most optical fibers use silica glasses in their composition, linking the optical transparency and absorption to the material properties of silica. Silica is transparent in the visible and near-infrared regions yet prone to high attenuation in the mid-infrared and ultraviolet regions²⁹⁸. Silica based fiber optical cables of this design are also limited by small refractive index contrasts of the core and cladding material which need to be thermally compatible and the nonlinear optical response of the silica core limits the amount of light which can be transferred²⁹⁹. Conventional silica based optical fibers are designed with a careful balance between optical material losses and nonlinearity effects and years of refinement of fiber design has pushed the fabrication technology to close to the innovative limit for these structures^{299 300}.

PhC fibers are a separate class of optical fiber emerging in optical fiber research since the first demonstration of a silica core surrounded by a silica-air PhC fiber in 1996³⁰¹. PhC fibers were proposed as alternatives to traditional optical fibers, specifically for applications outside of optical communications where standard fibers failed to meet demands such as higher power transport, optical sensing, engineered dispersion and nonlinearity³⁰². PhC fibers make specific use of the photonic bandgap in ordered structures to guide light

along the waveguide. Typically, PhC fibers are categorised as solid or hollow core fibers depending on the composition of the waveguide. The mechanisms for light guiding in these structures are drastically different, as are the associated applications with each fiber. Solid core fibers are reminiscent of the conventional optical fiber design and function, while hollow core fibers represent a departure from the traditional optical waveguide mechanics used.

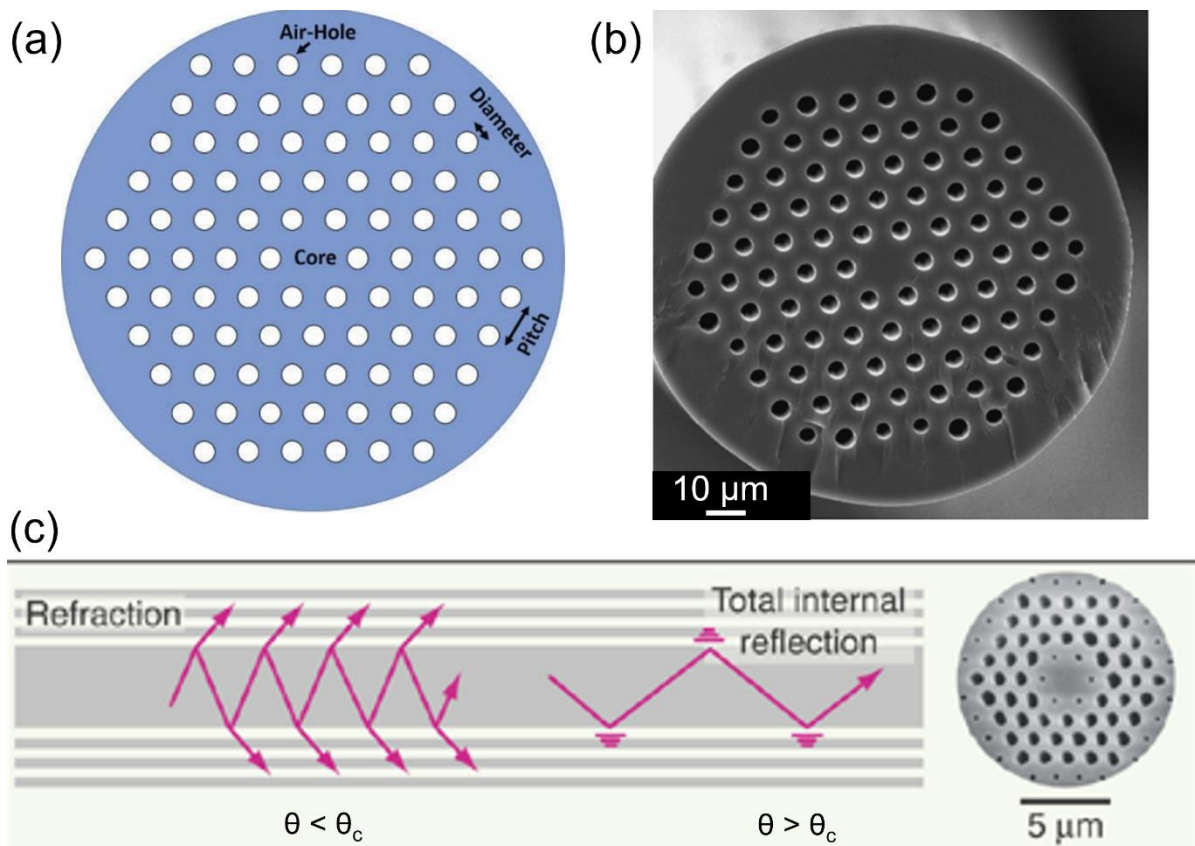


Fig. 22 (a) A solid core silica PhC fiber cross sectional image, showing a hexagonal PhC arrangement of five rings of air holes surrounding a silica core in a labelled schematic diagram³⁰³. Reproduced from ref³⁰³. Copyright 2019, OPTICA. (b) A microscopy image of a solid core 125.3 μm fiber with an average hole diameter of 4.79 μm and an average pitch of 9.97 μm ³⁰⁴. Adapted from ref³⁰⁴. Copyright 2006, OPTICA & IEEE Photonics Society. (c) The light guiding mechanism in solid core PhC fibers is shown governed by total internal reflection effects for angles larger than the critical angle²⁹⁹. Refraction effects prevent waveguide formation at angles below the critical angle. Adapted from ref²⁹⁹. Copyright 2002, American Association for the Advancement of Science.

First looking at solid core designs in PhC fibers, as depicted in Fig. 22, TIR governs the waveguide mechanism just as with standard optical fiber cables. The earliest PhC fiber designs were solid silica core structures surrounded by a PhC composed of a silica and air matrix with an incomplete photonic bandgap³⁰¹. Light is confined to the core region of these fibers by TIR effects between the silica core of higher refractive index and the silica PhC with a much smaller effective refractive index due to the presence of air holes. The

increase in refractive index contrast between the core and cladding affects the dispersion in these fibers, enabling the creation of a single-mode broadband optical continuum over the visible range³⁰⁵.

Ultra-flattened, near zero dispersion has also been achieved in the infrared region of solid core structures with precise control over the hole shape, size and core diameter³⁰⁶. The birefringence of the fiber can also be engineered in the structure by altering the air capillary thicknesses surrounding the silica core, creating birefringent effects up to ten times stronger compared to conventional optical fiber designs³⁰⁷. Larger core diameters supporting only a single-mode are also possible, provided the shape and geometry of the PhC fiber are conserved³⁰⁸. Larger effective core diameter designs allow for higher power applications while reducing nonlinear effects^{309 310}. Many of these effects can be engineered in fibers depending on the specific application. For example, supercontinuum light sources are feasible with PhC fibers due to the higher power output, broad spectral bandwidth and the control over nonlinear effects with applications in optical coherence tomography, spectroscopy and frequency metrology^{311 312 313}.

Hollow core PhC fibers operate on with a fundamentally different mechanism for guiding light. Hollow core fibers are generally formed as an air core surrounded by a 2D PhC structure. The first demonstration of a single mode hollow core fiber structure was of an air core surrounded by a silica-air PhC³¹⁴. Waveguides in hollow core fibers are created using the complete photonic bandgap of the cladding around the central air core. Specific frequencies of light are confined to the core based on the coherent Bragg reflection from the PhC cladding. Importantly, TIR effects are not occurring in hollow core fibers as the refractive index of the air core is strictly lower than the surrounding material; light is guided by photonic bandgap reflections only. This distinction in waveguide mechanics has led to the term photonic bandgap fiber often being used to describe hollow core fibers. Light travelling along a hollow core fiber is unique compared to other fiber designs as it does not need to transport through a solid material, like silica. As a result of this, 99% of the optical power in these fibers travels through air instead of silica glass removing the fundamental scattering and absorption processes associated with glass waveguides³¹⁵. The absence of the solid core loss mechanisms and reduced optical nonlinearity effects make hollow core fibers attractive candidates for low loss fiber designs^{315 316}. Typical designs of hollow core PhC fibers can be seen depicted in Fig. 23.

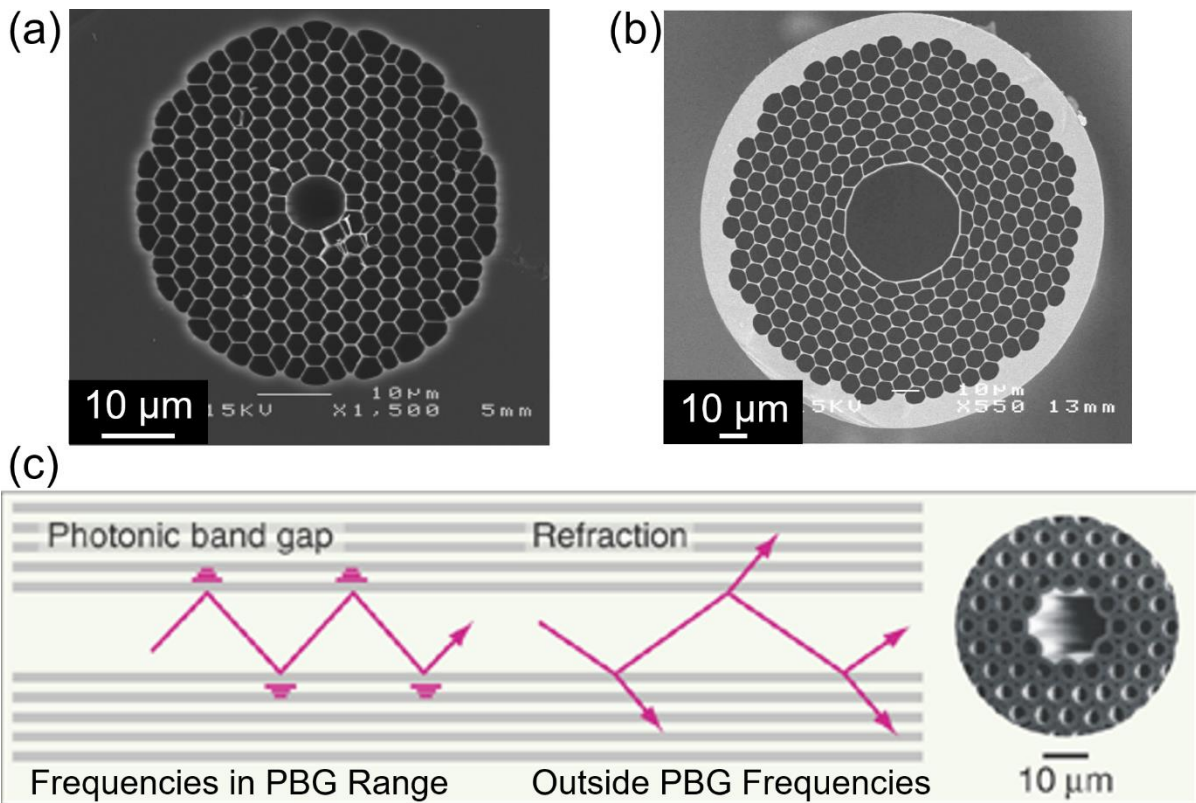


Fig. 23 (a) Microscopy image of a hollow core silica PhC fiber designs engineered with an 8.2 μm diameter hollow core surrounded by a 7-layer silica PhC used as a waveguide for 1064 nm radiation³¹⁷. Adapted from ref³¹⁷. Copyright 2004, OPTICA. (b) A 40 μm diameter hollow core surrounded by a 7-layer silica PhC designed as a waveguide for Mid-IR wavelengths above 3 μm ³¹⁸. Adapted from ref³¹⁸. Copyright 2005, OPTICA. (c) Schematic diagram showing the conditions for establishing a waveguide in hollow core PhC fibers²⁹⁹. Frequencies inside the span of the photonic bandgap are guided along the fiber; refraction occurs for frequencies outside the photonic bandgap. Adapted from ref²⁹⁹. Copyright 2002, American Association for the Advancement of Science.

Hollow core fiber designs present many opportunities and applications compared to traditional optical fibers. The reduced nonlinear response and absorption of an air core compared to a silica core is reported to reduce the Kerr response (nonlinear refractive index changes) of the fiber by a factor of up to 1000^{319 320}. This reduction in nonlinear effects has led to the development of anti-resonant hollow core fibers used for transporting high power ultrashort laser pulses^{298 317 320 321} without lengthening the pulse duration, reducing the peak intensity or incurring damage to the fiber, as experienced in conventional silica core waveguides. Ultrashort laser pulses have practical applications in areas such as micromachining³²² and biomedicine^{323 324}. Hollow core PhC fibers are also ideal for transporting wavelengths of light which fall outside the silica transparency window. Silica is prone to damage from UV wavelengths; anti-resonant hollow core fibers can better transport UV light due to significantly reduced interactions between the guided light and solid material in the PhC cladding^{298 325}. While mid-IR waveguides in solid core fibers can be achieved by using modified

chalcogenide glasses in the fiber design, hollow core fibers have the advantage of being less fragile and transmitting deeper into the infrared³²⁶.

One area which has exploited the photonic bandgap confinement in hollow core fibers is nonlinear optics³²⁷. The design of hollow core fibers allows a tailored nonlinear optical response depending on the application; air-filled fibers with low intrinsic nonlinearities are ideal for transporting high power pulses and liquid or gas-filled fibers can create high levels of nonlinearity for low power frequency conversion effects. Nonlinear materials, such as liquids and gasses, can also be introduced into the hollow core region for specific applications requiring increased light path lengths, high intensities, high optical damage threshold and a controlled group velocity dispersion by alteration of the pressure³²⁸. Argon gas-filled hollow core PhC fibers have demonstrated a capability of acting as bright, spatially coherent and wavelength tunable UV laser sources using the nonlinear response of a 27 μm gas-filled fiber when pumped with IR ultrashort pulses³²⁹. Variation of the pulse energy and Ar gas pressure allowed the wavelength of the UV light produced to be tuned between 200 and 300 nm with conversion efficiencies up to 8%.

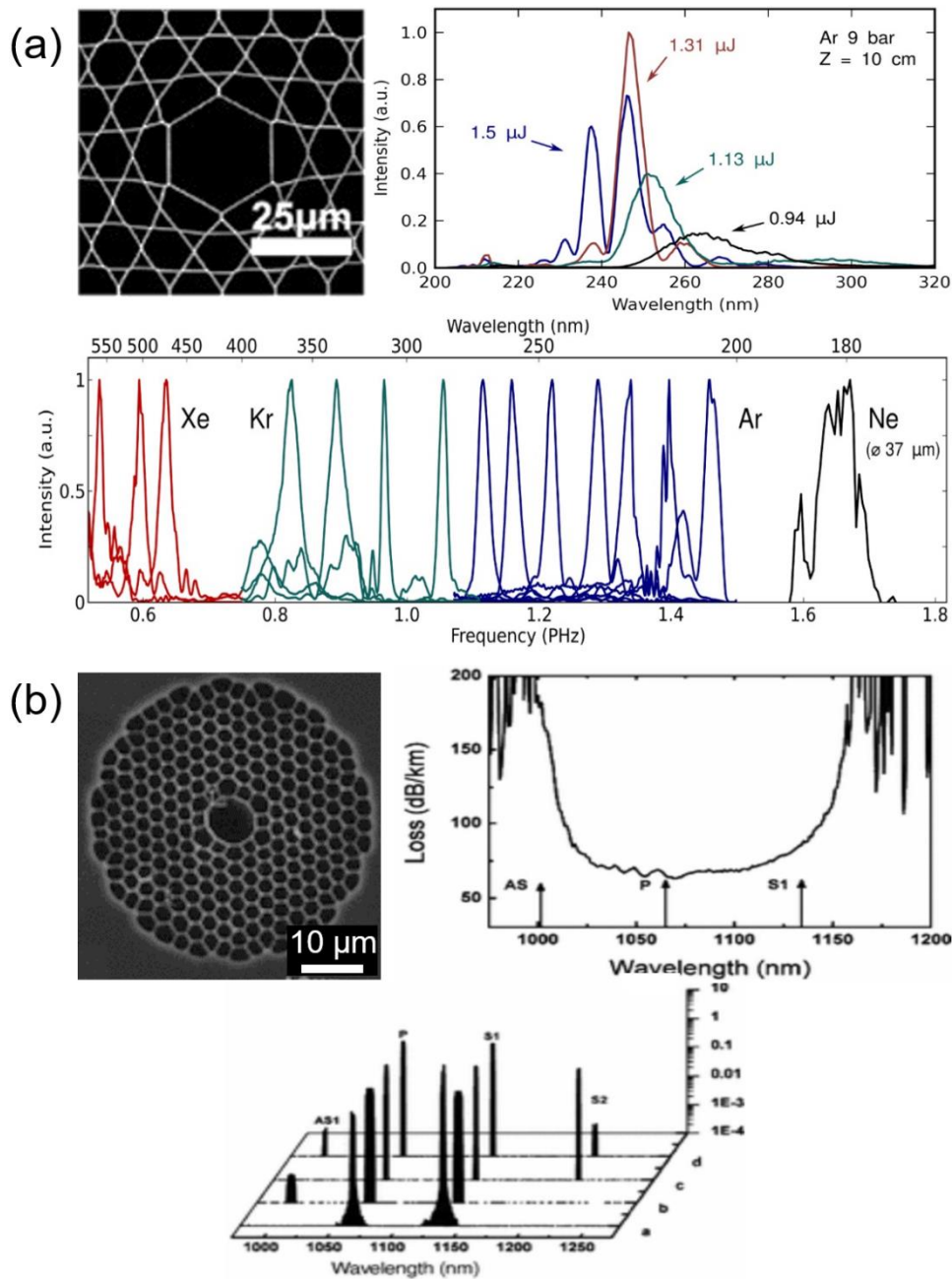


Fig. 24 (a) A 27 μm hollow core PhC fiber with a Kagomé design. The Ar-filled fiber pumped at 800 nm displays a range of different spectral shapes depending on the power of the input pulse. Different gas pressures and pump energies vary the spectral output for Xe and Kr gas in the same fiber. A deeper UV output is possible with Ne gas in a larger fiber³³⁰. Adapted from ref³³⁰. Copyright 2013, OPTICA. (b) A hollow core fiber design filled with H₂ gas for detection of rotational Raman bands with low loss across the fiber for the pump wavelength (P), Stokes (S1) and anti-Stokes (AS) signals. Output could be tuned by varying polarisation and input pump power³³¹. Adapted from ref³³¹. Copyright 2004, American Physical Society.

A follow up study³³⁰ found that the gas could also be changed resulting in optical frequencies for Xe and Kr and a deeper UV signal for Ne, as seen in Fig. 24 (a). Low threshold stimulated Raman scattering is another example of an application of hollow core fibers. Using photonic bandgap guided light in hollow core fibers, frequencies were filtered in light interacting with H₂ gas, suppressing stronger vibrational modes and

allowing the observation of weaker rotational bands at energy thresholds up to 10^6 lower than previous observations^{331 332}. Varying the pump polarisation further allowed the Raman output spectral components to be controlled, as seen in Fig. 24 (b). Lastly, there have even been reports of utilising the slow photon effect in conjunction with nonlinear optics in PhC waveguides³³³. Enhancements of self-phase modulation induced spectral broadening of output signals and two photon absorption³³⁴ alongside delayed transmissions of picosecond optical pulses³³⁵ are some examples of effects being attributed to slow photon behavior in 2D silicon waveguides.

Recent studies with PhC fibers, primarily hollow core designs, are exploring the vast range of analytes which can be detected using PhC fiber sensors. Sensors for chemical and biological species are consistently emerging from the literature. Gas sensors for CO_2 ³³⁶, N_2O ³³⁷ and CH_4/HF ³³⁸, chemical sensors for kesosene concentration in fuel³³⁹ and detecting illicit drugs³⁴⁰, health monitoring biosensors for glucose³⁴¹ and cholesterol³⁴² and health diagnostic sensors for detecting various types of cancer cells^{343 344 345} are among some of the emerging applications for PhC fiber sensors. Some PhC fiber sensor research aims to improve the selectivity and sensitivity of detections by combining the waveguide mechanism of the fiber with the surface plasmon effect^{346 347 348}, incorporating metal particles or thin metal layers into the fiber to enhance detection sensitivity. Other research works investigate the material used to fabricate the fiber to identify optimal operating conditions with thermoplastic polymer materials, such as Zeonex and Topas, showing promising applications for Terahertz frequency ranges^{349 350}. Emerging graphene-based PhC fibers are being explored due to graphene's high surface to volume ratio, low associated cost with simple synthesis and its ability to protect against oxidation of metals (e.g. Ag) with its high electron density preventing molecules from passing through the ring-like structure for surface plasmon applications^{351 352 353}.

6 Photonic Crystal Structural Porosity and Interconnectivity Applications

Thus far, the wide array of optical applications for PhC materials have been discussed across several disciplines. When discussing optical implementation, the ability of the material to attenuate, tune or reflect

incoming light is a major consideration for the incorporation of repeating structured dielectric layers; the role of the structure is to provide the required optical response. Beyond optical applications, PhC materials have found practical uses relating to their structure alone. 3D PhC structures, such as IOs in particular, are often prepared for the porous interconnected structure of crystalline material as opposed to any optical considerations. In many cases where the structure of ordered material is central to its implementation, IOs and other 3D PhCs are often classified as three-dimensionally ordered macroporous (3DOM) materials^{82 354 355}. From a structural standpoint, some of the attractive qualities of 3DOM materials include an increased surface-to-volume ratio compared to bulk materials, a bi-continuous material with an interconnected solid material and an interconnected pore system, efficient mass transport through the structure with low tortuosity and relatively large pores to allow for surface functionalisation of the material walls^{83 356}. For porous structures, the simplicity and inexpensive size-controlled fabrication method for IOs alongside the wide range of compatible materials add to the appeal of using IO 3DOM materials versus other ordered porous materials³⁵⁷. In this section, applications involving the structure of 3DOM materials are discussed to shed some light on the potential benefits arising from utilising materials like IOs other than their ability to modulate light propagation.

IO materials have emerged as ideal structured candidates in certain areas of biomedicine^{114 115}. In general, the scale of these types of IO materials are much larger than their photonic counterparts with pore sizes of around 100 μm . However, the colloidal crystal templating and inversion procedure is identical, producing structurally similar IO materials, albeit with larger repeating lattice sizes etc. The role of IO materials in biomedical research is to act as structural scaffolds or biomimetic supports with an ordered and interconnected surface; purely a structural function with no optical component. In biomedicine, the area of cell culturing and tissue engineering has explored the benefits of IO materials as structural supports. Tissue engineering involves transplanting a biofactor (cells, genes or proteins) into a porous degradable material scaffold; the scaffold acts to provide temporary mechanical support and deliver the biofactor throughout so that the regenerated tissue assumes function as the scaffold degrades³⁵⁸. Aside from initially supporting the cells and aiding in their proliferation, the architecture of the porous support ultimately decides the shape of the newly grown tissue in an ideally reproducible and economically viable large scale³⁵⁹.

A major factor found to influence the reproducibility and the homogeneity of cells grown across the porous scaffold is the uniformity of the scaffold material, with uniform IOs outperforming structures with non-uniform pore sizes in terms of diffusion of macromolecules and the uniformity of the fibroblast cell distribution in the IO scaffold³⁶⁰, as seen in Fig. 25 (a). Non-uniform pore structures can produce regions with insufficient concentration of nutrients for cells, inhibiting homogenous tissue formation. In this case, gelatin microspheres, prepared via sedimentation evaporation, were used as the sacrificial template and infiltrated with PGLA under vacuum suction to form the IO structure. A common IO material used in tissue engineering is poly(D,L-lactide-co-glycolide) (PLGA)^{360 361 362}, a polyester material approved for clinical trials with a controllable degradation rate depending on the lactic and glycolic acid ratios used in preparation³⁶³. A study of PLGA IOs found that the pore and window (interconnected circular openings between adjacent pores) size of uniform IOs had an effect on the physical properties (compressive moduli) and migration depth of cells in the IO scaffold³⁶¹. Larger pores and windows featured a greater migration depth of cells with a lower compressive modulus. PLGA IO scaffolds with gradations in hydroxyapatite (HAp) nanoparticle minerals allowed for a spatial control of cells grown across the scaffold, potentially beneficial for emulating connective tissue-to-bone interfaces³⁶². Outside of PLGA IOs, chitosan³⁶⁴ and silk fibroin³⁶⁵ IO scaffolds have also been investigated for tissue engineering. For the silk fibroin IO scaffolds, the ordered geometry of the IO structure was found to promote almost double the mineralisation of human mesenchymal stem cells compared to a silk fibroin scaffold prepared with a similar average pore diameter by salt-leached processes³⁶⁵, as seen from calcium concentrations in Fig. 25 (b). In more recent works, hydrogel IO systems have been used as targeted drug delivery systems with drug release controlled by application of NIR radiation for wound healing³⁶⁶ or spinal cord repair³⁶⁷. Anisotropic IO structures, deformed by stretching an axis in a particular direction, have been utilised to direct the orientation of cell growth for controlling nerve cell growth³⁶⁸ and preventing skin scar formation³⁶⁹.

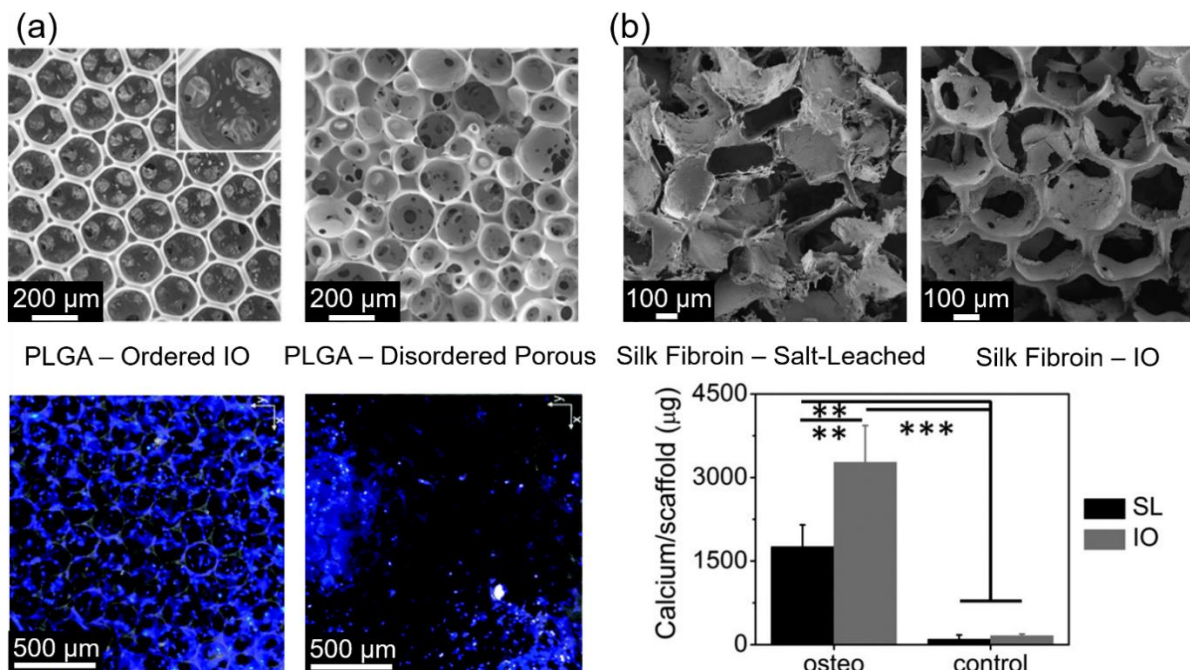


Fig. 25 (a) Comparison between PLGA scaffolds using an ordered IO and a disordered porous scaffold with fluorescence micrographs showing fibroblast cell distributions throughout each structure after 7 days of cell culture³⁶⁰. Adapted from ref³⁶⁰. Copyright 2010, American Chemical Society. (b) Comparison between silk fibroin scaffolds prepared from a salt-leaching process and an IO. Greater mineralisation is detected for the IO with higher calcium content per scaffold³⁶⁵. Adapted from ref³⁶⁵. Copyright 2017, Wiley.

The macroporous structure of IO configurations has also attracted some attention for its potential to act as a separation or filtering membrane. Specifically, 3DOM IO structures with highly interconnected and regular pore sizes have been explored as microfiltration³⁷⁰ or ultrafiltration³⁷¹ separation membranes. Porous membranes are often used in filtration systems where the membrane attempts to remove particles suspended in a liquid, with water purification being a prime example of the process. Porous membranes are often investigated in terms of the separation efficiency (the efficiency at which particles are removed) and the permeation flux (the stable rate at which a liquid feed can be processed). An enhancement of the separation efficiency often results in a decrease of the permeation flux and vice-versa. 3DOMs are appealing as separation membranes due to their high pore uniformity with the potential to act as highly selective separators for desired species³⁷². The ability to tune pore size in fabrication allows the sizes of filtered particles to be controlled while an interconnected pore system in a membrane is advantageous for establishing a slower rate of flux decline from pore blockage³⁷³. Compared to other methods of fabricating 3DOMs, including non-solvent-induced phase separation of block co-polymers and microelectromechanical systems, IOs offer a simple

solution of producing a uniform porous membrane without the need for highly specialised machinery for patterning or fine tuning the stochastic porous structures for block co-polymers.

IO membranes prepared from photo-initiated polymerisation of monomer solutions of hydroxybutyl methacrylate and 2-hydroxyethyl methacrylate at differing ratios were demonstrated to be capable of particle fractionation of silica particles in a feed solution³⁷⁰. For samples prepared from 835 nm silica templates, smaller interconnecting pore windows of about 200 nm in the IO membrane prevented larger particles (440 and 835 nm silica particles) from transmitting across the membrane while allowing smaller 60 nm silica particles to pass through. Many battery systems often contain a separator membrane in the electrolyte between the anode and the cathode to prevent electrical contact between the electrodes and maintain ionic flow. Uniform IO structures fabricated from UV curing of ethoxylated trimethylolpropane triacrylate (ETPTA) polymer in a SiO₂ nanoparticle matrix have shown promising applications as battery separator membranes relative to commercial trilayer polypropylene / polyethylene / polypropylene (PP/PE/PP) separators with randomly distributed pores³⁷⁴. In a LiCoO₂ cathode and graphite anode battery configuration, the ETPTA IO separator membranes showed similar performances to the commercial separators at low mass loadings and slow cycling rates and improved performances for high mass loadings and fast cycling rates, as seen in Fig. 26 (a). The improvement in performance was attributed to the increased ion transport through the well-ordered, nanoporous structure of the IO separator membrane.

Modifications to macroporous 3DOMs have allowed IO membranes to modify their particle selectivity. Particle-nested IO structures, consisting of polystyrene particles embedded in a poly(urethane acrylate) IO matrix, have been shown to possess excellent separation efficiency of nanoparticles with the potential to tune the size selectivity of the particle separation via alteration of the size ratio between the nested polystyrene particle and the IO pore window³⁷⁵. Nanoparticle separation is attributed to nanochannels formed between the nested polystyrene particle and the IO walls; Au nanoparticles exhibited high rejection rates when the estimated size of the nanochannels were smaller than the Au nanoparticle sizes, as seen in Fig. 26 (b). A hybrid structure combining the macroporous nature of a poly(urethane acrylate) IO matrix with mesoporous block-copolymer (polystyrene-block-polymethyl methacrylate) structures inside the interconnecting pore

windows has demonstrated a size-selective nanoparticle separation without comprising the high permeability of the IO structure³⁷⁶. 18 nm nanosieves in the block-copolymer material of the hybrid membrane structure displayed excellent size selectivity in filtering Au nanoparticles with sizes above 18 nm showing complete separation, as seen Fig. 26 (c).

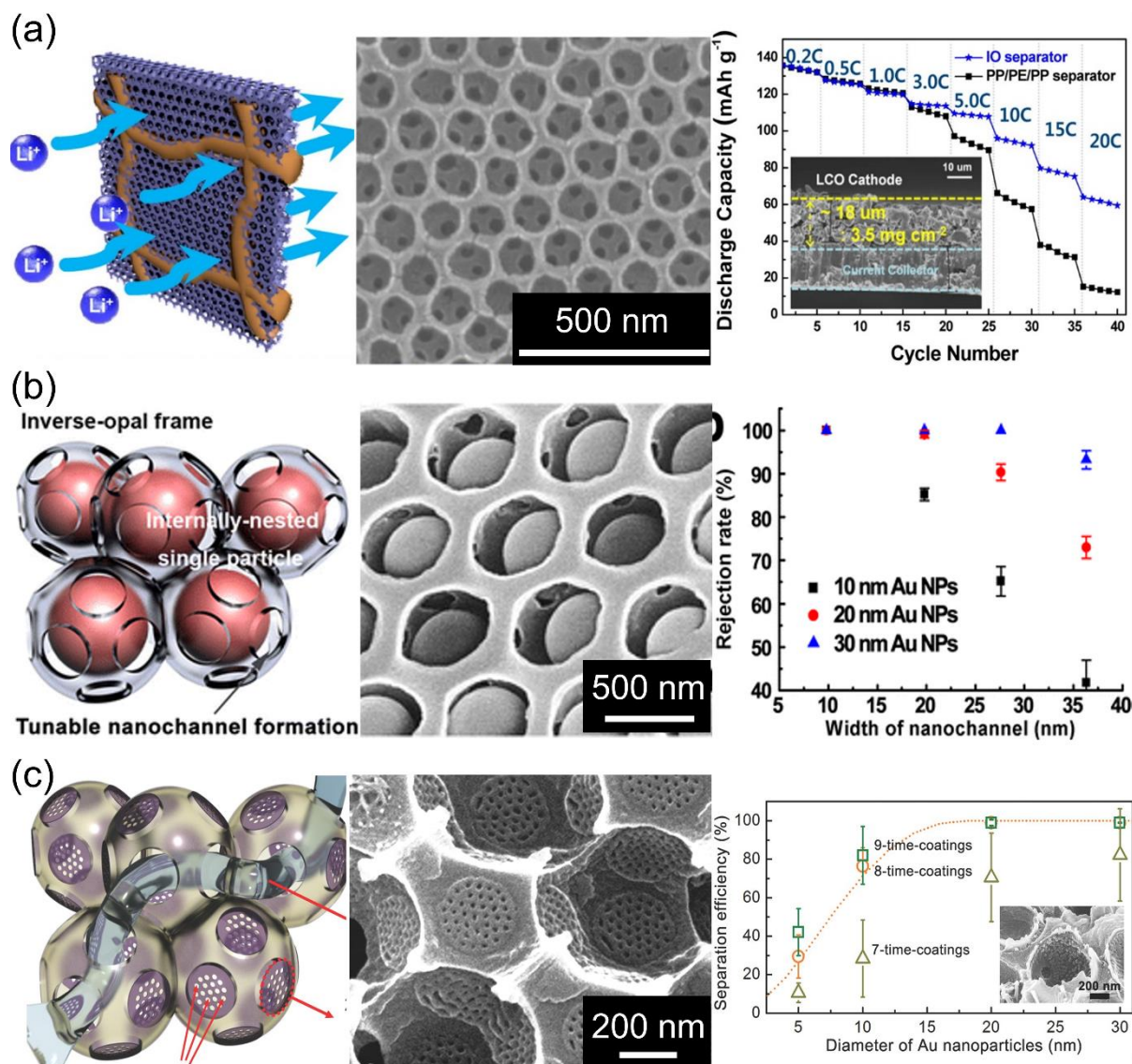


Fig. 26 (a) SEM image and concept art of an ETPTA IO separator membrane used in a LiCoO₂ versus graphite battery³⁷⁴. Discharge capacities are compared for an IO separator versus a commercial randomly porous PP/PE/PP separator for various cycling rates. Adapted from ref³⁷⁴. Copyright 2014, American Chemical Society. (b) Schematic diagram and SEM image for a poly(urethane acrylate) IO with a nested polystyrene particle within the IO cavity³⁷⁵. The rejection rate of Au nanoparticles of different sizes versus estimated widths of nanochannels is also shown. Adapted from ref³⁷⁵. Copyright 2014, American Chemical Society. (c) Schematic diagram and SEM image for a hybrid macroporous poly(urethane acrylate) IO with mesoporous block-copolymer nanosieves. The separation efficiency of the structure with 18 nm nanosieve dimensions is shown for Au particles of various diameters³⁷⁶. Adapted from ref³⁷⁶. Copyright 2014, Wiley-VCH.

The interconnectivity and increased surface area exposed in 3DOMs has attracted attention for catalytic applications where catalytic reactions are increased due to the macroporous nature of the structured material. Ceria-zirconia IOs ($\text{Ce}_{0.5}\text{Zr}_{0.5}\text{O}_2$) were investigated in relation to the role of the macroporous interconnected geometry of the 3DOM in relation to the catalytic oxidation of propane and compared to $\text{Ce}_{0.5}\text{Zr}_{0.5}\text{O}_2$ catalysts produced from crushed IOs or featuring no template³⁷⁷. The macroporous IO structures featured the best performances, attributed to the increased tortuosity of the gas transport path in the other structures investigated, as seen in Fig. 27 (a).

The ordered IO structure can also function as an excellent catalyst support for loading of metal particles onto a semiconductor surface. The high surface area and porosity of an SnO_2 IO was utilised for functionalisation of the IO material with monodispersed immobilised Pd nanoparticles which were well dispersed throughout the structure and easily removed post reaction³⁷⁸. Compared to commercially available Pd/C structures, the Pd/ SnO_2 IOs demonstrated formic acid oxidation with an onset voltage ~ 180 mV below the commercial standard, as depicted in Fig. 27 (b). This enhancement effect was attributed to the uniform distribution of particles and the porosity of the IO structure facilitating increased access to catalytically active sites. Some recent works choose to adopt IO structured materials primarily for their ability to easily increase the specific surface available through their natural porosity, thus increasing the number of active catalytic sites for the photocatalyst material^{379 380}. Other works choose IO materials for their ability to easily accommodate metal particles onto a semiconductor surface due to the open network of material alongside the intrinsic structural porosity, such as noble metal decoration onto TiO_2 ^{381 382} and ZnO ^{227 383} photocatalysts. Double inverse opal structures have also been proposed as a method to confine particulate photocatalysts to a structure without decreasing the active surface area³⁸⁴. From examples in the literature, photocatalysts are frequently structured as 3DOMs, both for the structural advantages of the macroporous structure and optical phenomenon such as the slow photon effect, see Section 3 for more details.

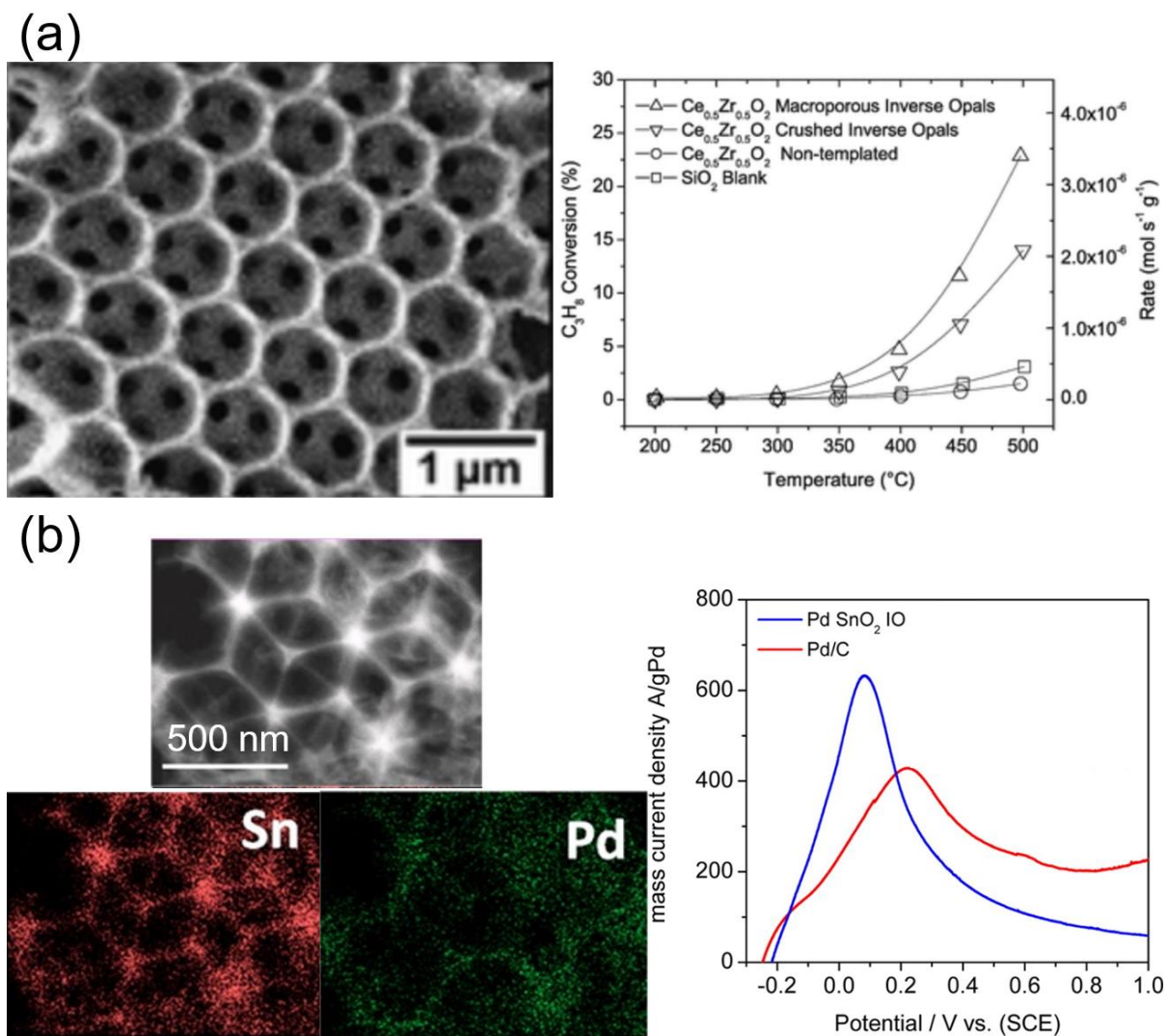


Fig. 27 (a) $\text{Ce}_{0.5}\text{Zr}_{0.5}\text{O}_2$ IOs with a macroporous structure showing an enhanced catalytic oxidation of propane compared to non-templated and crushed IO structures³⁷⁷. Adapted from ref³⁷⁷. Copyright 2008, Royal Society of Chemistry (b) SnO_2 IOs with Pd nanoparticles dispersed throughout the structure³⁷⁸. The peak potential for catalytic formic acid oxidation is compared for the Pd SnO_2 IO and commercially used Pd/C structures. Adapted from ref³⁷⁸. Copyright 2013, American Chemical Society.

IO 3DOMs have seen widespread use in battery electrode research in recent years with the macroporosity of the interconnected electrode being investigated for lightweight, high cycling rate and high energy density applications. A vast array of different material candidates have been structured with an IO geometry for evaluation of the electrochemical performance as an anode or cathode. On the anode side silicon³⁸⁵, carbon³⁸⁶, germanium³⁸⁷, TiO_2 ¹¹¹, GeO_2 ³⁸⁸ and Co_3O_4 ³⁸⁹ are among some of the materials for which the incorporation of the IO structure has been investigated. IO structures of LiFePO_4 ³⁹⁰, V_2O_5 ³⁹¹ and sulfur³⁹² (encapsulated by a polypyrrole IO framework) have been explored as cathodes. From the earliest application of a 3DOM to an electrode³⁹³, the electrochemical benefits of an IO structure were proposed as a reduction in

electrode polarisation compared to bulk materials where mass transport is inhibited by the high tortuosity of ion diffusion paths. Lithium-ion battery electrodes with a 3D structure are thought to reduce the overall cell resistance by improving the electrolyte transport, creating a fast charging capability and reducing the risk of lithium plating in the cell³⁹⁴. For IOs, the macroporous structure facilitates electrolyte access to the electrode material at interstitial points. The IO material walls are also nominally thin relative to the IO pore size, often just several nanometres thick, allowing for short ion diffusion paths and creating high rate capabilities.

In terms of the specific energy associated with an electrode, the specific capacities (capacity per mass of material) for a range of different electrode designs in lithium-ion batteries have been investigated relative to IO designs. For flexible TiO₂ electrodes deposited on carbon cloth, two anatase TiO₂ IO electrodes (3T-CC – annealed in air and 3T-C-CC – annealed in Ar) were investigated versus an anatase TiO₂ nanoparticle slurry on carbon cloth (NP-CC) with carbon black and polyvinylidene difluoride additives³⁹⁵. Figure 28 (a) displays the performance of the electrodes compared at a high cycling rate of 10 C with the superior performance of the IO materials displaying larger specific capacities compared to the nanoparticle coating; a larger surface area in contact with the electrolyte and fast lithiation kinetics were proposed for the superior IO 3DOM performance. A separate study of rutile TiO₂ IOs¹¹¹ found that the IO electrode composition was maintained alongside a stable specific capacity across 5000 cycles indicating long-term structural stability and cycle life, even when tested at high cycling rates.

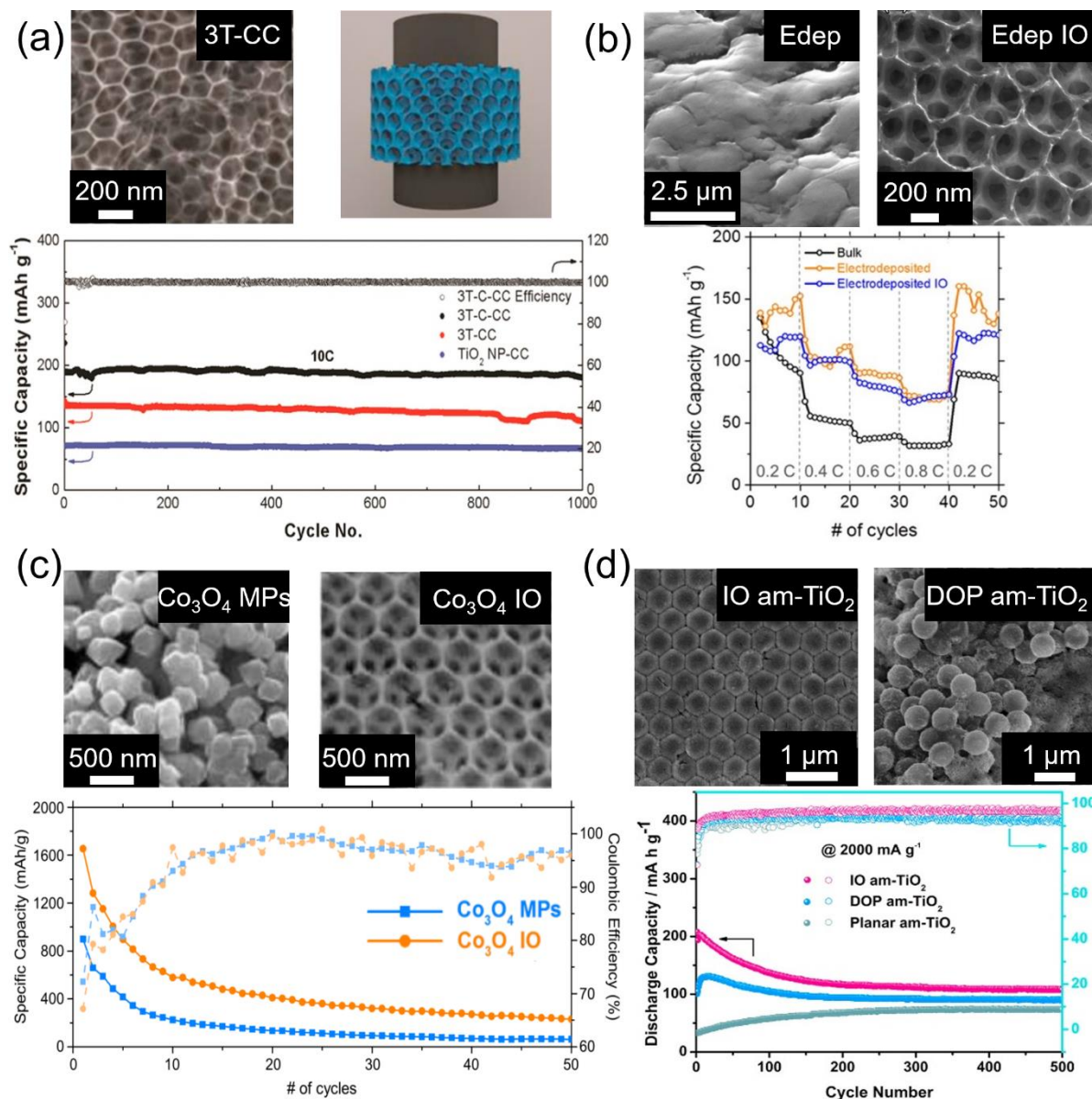


Fig. 28 (a) Flexible anatase TiO_2 IO electrodes prepared on carbon cloth (red and black data) showing superior specific capacity compared to anatase TiO_2 nanoparticle (blue data) slurry³⁹⁵. Adapted from ref³⁹⁵. Copyright 2016, Elsevier. (b) SEM images of electrodeposited V_2O_5 films for non-structured and IO-structured electrodes with higher specific capacities at rates below 1 C for electrodeposited films compared to bulk V_2O_5 films³⁹¹. Adapted from ref³⁹¹. Copyright 2015, American Chemical Society. (c) SEM images of Co_3O_4 micro particles and Co_3O_4 IO anodes. The specific capacity for the electrodes is higher with the IO structure³⁸⁹. Adapted from ref³⁸⁹. Copyright 2017, IOP Publishing. (d) SEM images of hollow amorphous TiO_2 spheres in IO and disordered porous architectures. The IO architecture shows the highest specific capacity compared to TiO_2 disordered porous and planar films in a sodium-ion battery system³⁹⁶. Adapted from ref³⁹⁶. Copyright 2017, Elsevier.

At low cycling rates (< 1 C) electrodeposited V_2O_5 cathodes, structured with and without an IO architecture, were found to boost improved specific capacities relative to bulk V_2O_5 films, as seen in Fig. 28 (b)³⁹¹. The V_2O_5 IO cathodes were also found to maintain a dominant intercalation mode response at higher

scan rates. The performance of a conversion mode Co_3O_4 anode was compared for a 400 nm IO structure and an electrode formed from 400 nm Co_3O_4 micro particles, both deposited on stainless steel³⁸⁹. The ordered IO structure offered significantly higher specific capacity compared to the disordered collection of micro particles, as seen in Fig. 28 (c). Outside of lithium-ion batteries, sodium-ion batteries have also explored the IO structure for their electrodes^{396 397 398}. amorphous TiO_2 IO architectures, prepared as hollow spheres using atomic layer deposition, were explored for use in sodium-ion batteries and compared to amorphous disordered TiO_2 and planar TiO_2 films³⁹⁶. The ordered IO architecture featured the largest specific capacity and highest rate performance, as depicted in Fig. 28 (d), which was attributed to good electrolyte wettability enhancing the effective surface ion availability, an important consideration in sodium-ion batteries due to the larger ion size relative to lithium-ion batteries.

The interconnected electrode material may also achieve better electrical conductivity compared to other material designs aimed at improving surface area interactions. In comparison to interconnected 3DOMs, energy densities in composite nanoparticle coatings are often limited by the requirement of additional binder and conducting agents to ensure electronic conductivity between particles despite the higher relative surface areas nanoparticle electrodes could provide³⁹⁹. As mentioned previously, the porous IO network allows for greater electrolyte access and easier ion insertion/removal. A common observation with IO electrode materials is an impressive C-rate for the battery material; high specific currents are often shown to be fully reversible while maintaining an impressive specific capacity for the system, an important consideration for high energy applications. The macroporosity of the IO structure has also been proposed to help reduce structural stresses in materials with large volume changes during lithium insertion and removal³⁸⁵. Some of these features of IO electrodes are examined in Fig. 29.

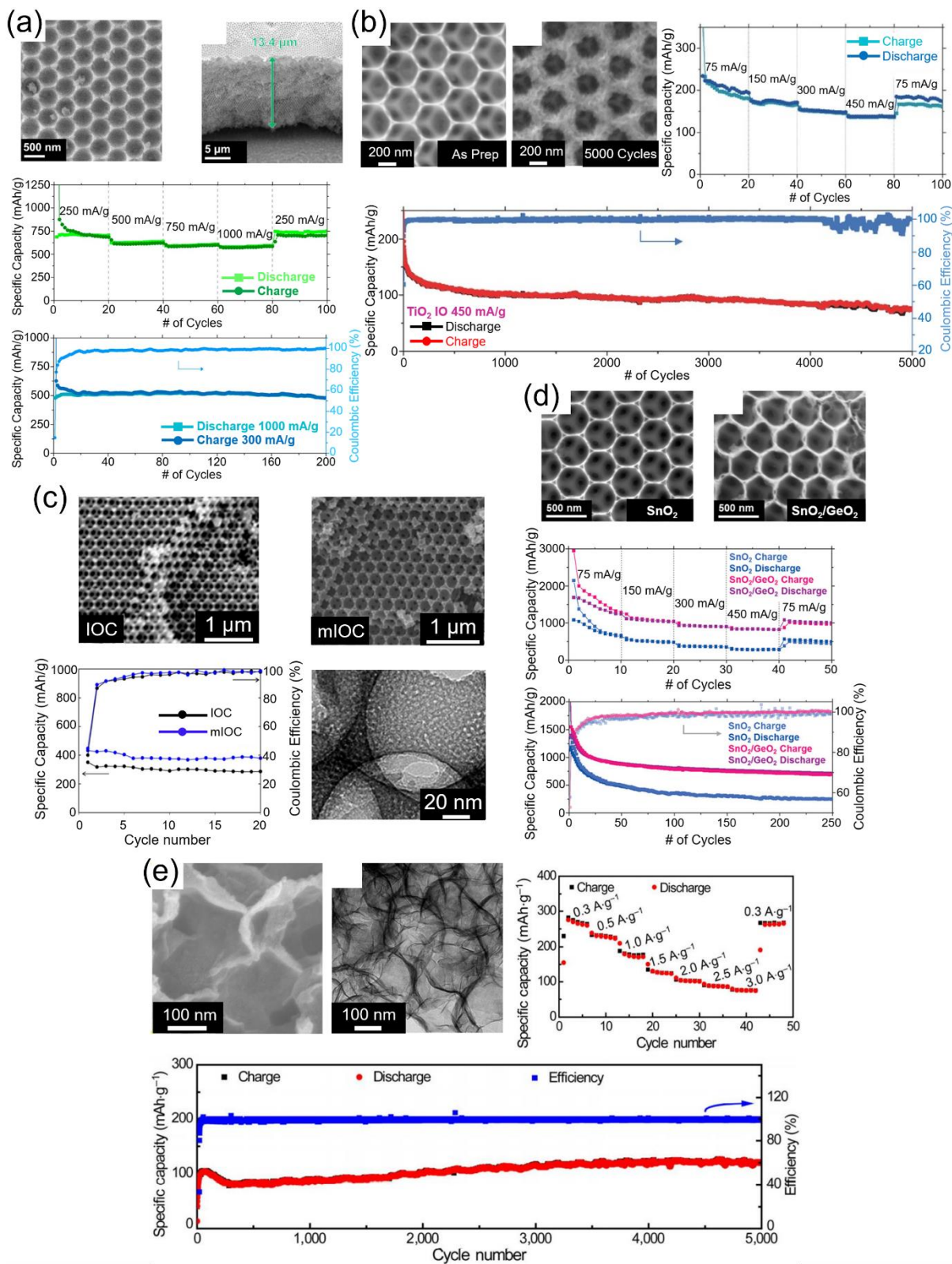


Fig. 29 (a) GeO_2 IO anode exhibiting large specific capacities, high rate capabilities (highly reversible capacities up to 1000 mA/g) and stable asymmetric galvanostatic cycling³⁸⁸. Adapted from ref³⁸⁸. Copyright 2018, Elsevier. (b) TiO_2 IO anode with high rate capability and long term performance stability of up to 5000 cycles¹¹¹. Adapted from ref¹¹¹. Copyright 2017, Wiley. (c) Carbon IO anode materials with a bare carbon IO (IOC) compared to a mesoporous carbon IO (mIOC)⁴⁰⁰. Mesoporous carbon combined with the IO shows superior performance. Adapted from ref⁴⁰⁰. Copyright 2013, American Chemical Society. (d) Nanocomposite $\text{SnO}_2/\text{GeO}_2$ IO anodes with strong rate capability and higher specific capacities when compared to a bare SnO_2 IO anode⁴⁰¹. Adapted from ref⁴⁰¹. Copyright 2020, Wiley-VCH. (e) MnO_2 IO cathode used in an aqueous zinc-ion battery. The stable electrode performance (up to 5000 cycles) and high rate capability is attributed to the stacked IO template⁴⁰². Adapted from ref⁴⁰². Copyright 2019, Springer Science + Business Media.

Figure 29 (a) shows a germanium(IV) dioxide (GeO_2) inverse opal explored as an anode candidate in a lithium-ion battery³⁸⁸. The highly interconnected IO structure of the electrode does not require additional binders or conducting additives and delivers a high specific capacity of 531 mA h g^{-1} even after 1000 cycles at a specific current of 300 mA g^{-1} . Excellent rate capabilities are also demonstrated with fully reversible cycling present for higher specific currents up to 1000 mA g^{-1} . The potential for asymmetric discharge (1000 mA g^{-1}) and charge (300 mA g^{-1}) rates are also explored. A long term study for rutile phase TiO_2 IOs is present in Fig. 29 (b), where a TiO_2 IO is investigated as an anode material in lithium-ion batteries for up to 5000 cycles¹¹¹. The SEM images illustrate the structural stability is maintained in the IO even after long-term cycling. Different specific currents ranging from 75 to 450 mA g^{-1} , approximately yielding C-rates of 0.45 C & 2.68 C respectively, were found to be highly reversible for the material. The IO electrode demonstrated an impressive cycle life, yielding a specific capacity of 95 mA h g^{-1} after 5000 cycles.

Bare carbon inverse opals are compared to mesoporous carbon inverse opals in Fig. 29 (c) in relation to their performance as anode materials in lithium-ion batteries⁴⁰⁰. The extra surface area provided by the mesoporous carbon was thought to establish shorter solid state diffusion lengths. This effect, in combination with the inherent high interconnectivity of the IO template, gave larger specific capacities (32% larger after 20 cycles with a specific current of 100 mA g^{-1}) for the mesoporous carbon IO material compared to the bare carbon IO. Composite IO materials consisting of a combination of different active materials have also been explored as electrodes. A $\text{SnO}_2/\text{GeO}_2$ composite anode for use in lithium-ion batteries has been explored as a method of mitigating capacity fade from material volume variations commonly experienced in SnO_2 electrodes⁴⁰¹. Comparisons in electrochemical performance between bare SnO_2 IOs and composite $\text{SnO}_2/\text{GeO}_2$ IOs can be observed in Fig. 29 (d). Most notably, a much higher specific capacity and an improved capacity retention can be observed for the composite IO material. Similar IO works with composite materials of have explored similar strategies to improve the electrochemical performance and stability; Some examples include $\text{SnO}_2/\text{Bi}_2\text{O}_3$ composite IOs prepared on nickel foam⁴⁰³ and $\text{Li}_2\text{FeSiO}_4/\text{C}$ composite nanofibers incorporated into an IO design⁴⁰⁴. The enhanced rate capabilities and impressive cycle life of IO materials have also been explored for non-lithium-ion systems, such as a aqueous zinc-ion battery system with a MnO_2 cathode⁴⁰² shown in Fig. 29 (e). Even after completing 5000 cycles the aqueous system with the layered MnO_2 IO

structure shows an impressive specific capacity of 121 mA h g^{-1} at a high current density of 2000 mA g^{-1} , effects which were attributed to the structure of the cathode.

Conversely, in spite of the relatively large specific energies associated with IO electrodes, the inherently high porosity of the IO structure (26% material, 74% pore space) creates a lower volumetric energy density, when compared to other electrode structures³⁹⁹. Some efforts to enhance the volumetric energy density of IO electrodes have focused on additional material coatings deposited onto the IO scaffold^{399 405}.

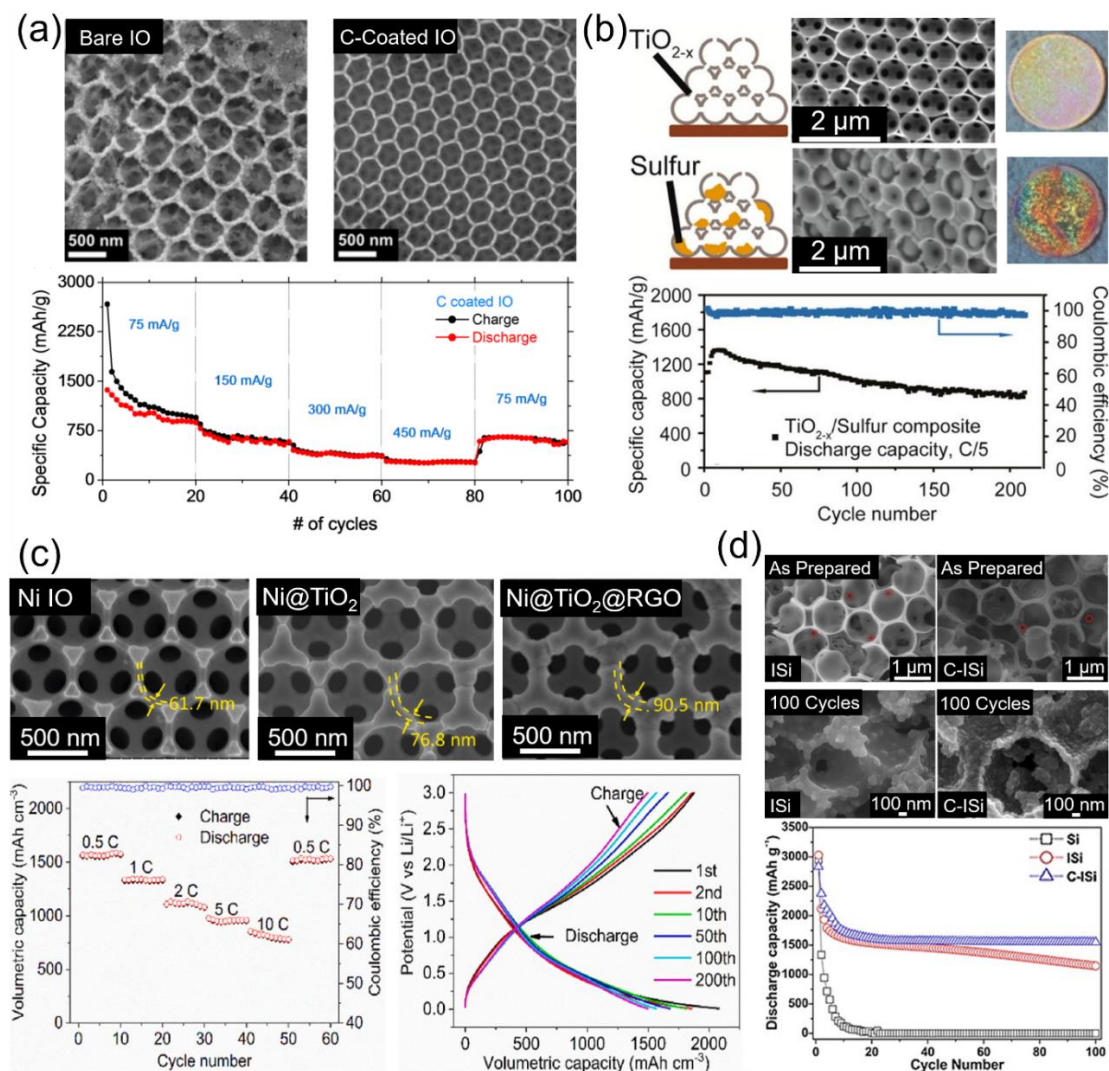


Fig. 30 (a) A conversion mode Ni-Mn-Co-O IO anode coated with carbon displaying high-rate performance and high specific capacities⁴⁰⁶. Adapted from ref⁴⁰⁶. Copyright 2017, Nature. (b) A hydrogen reduced TiO_2 IO structure infiltrated with sulfur to create a lithium-sulfur battery cathode⁴⁰⁷. Sulfur infiltration can be visually seen via structural color changes to the electrode and high reversible capacities are obtained after 200 cycles. Adapted from ref⁴⁰⁷. Copyright 2014, American Chemical Society. (c) A Ni IO anode coated with TiO_2 and further coated with reduced graphene oxide (RGO) showing high volumetric capacities and an excellent rate capability and an overall increased active material loading of the coated IO⁴⁰⁸. Adapted from ref⁴⁰⁸. Copyright 2021, Elsevier. (d) Silicon inverse opals (ISi) compared with carbon-coated silicon inverse opals (C-ISi) as anode materials⁴⁰⁹. SEM images and specific capacity are shown after 100 cycles. Adapted from ref⁴⁰⁹. Copyright 2015, Elsevier.

The inherent high interconnectivity and electrical conductivity, combined with the open porous network, of the materials used in IO electrodes makes them ideal candidates for hosting materials within their structure. Figure 30 explores some examples of how the IO structure has been utilised as a structural template support for other materials and the synergistic performance observed.

A conversion mode IO anode (Ni-Mn-Co-O) consisting of mixed oxides of nickel, manganese and cobalt used in a lithium-ion battery, both in a half-cell configuration and full cell versus a V_2O_5 cathode, is shown in Fig. 30 (a)⁴⁰⁶. The mixed oxide IO material was further altered via a carbon coating applied to the IO structure with the additional carbon thought to help maintain the structure during cycling. A lithium-sulfur system can be seen in Fig. 30 (b), where the sulfur material for the cathode is infiltrated into a hydrogen-reduced TiO_2 IO network acting as a host material to accommodate volume changes and strain during cycling⁴⁰⁷. The IO network acts to confine the sulfur material to the cathode and the surrounding hydrogen-reduced TiO_2 material prevents diffusion to the anode by binding with the polysulfide material generated, delivering a high specific capacity of 890 mA h g^{-1} after 200 cycles at a rate of 0.2 C. Similar strategies are used in other lithium-sulfur works with IOs of carbon⁴¹⁰ and polypyrrole decorated with ZnO nanocrystals⁴¹¹ investigated for confinement.

A Ni IO structural template was modified with two successive material coatings in an attempt to improve the volumetric energy capacity of porous electrode systems, where specific mass performances are often high yet the volume fraction of active material is often low due to high porosity. Figure 30 (c) displays Ni IO coated with TiO_2 material through atomic layer deposition and then further coated with reduced graphene oxide (RGO) through spray coating for an anode in a lithium-ion battery⁴⁰⁸. High volumetric capacities are obtained for the electrode system which were thought to arise from the synergistic effects of all active materials. The inner nickel material was stable while highly conductivity and the similar Li-ion intercalation mechanism in TiO_2 and RGO helped to maintain structural integrity. Silicon IOs are often investigated as anode materials for lithium-ion batteries due to the large specific capacities associated with silicon electrodes. Volumetric expansion of silicon when alloying with lithium-ions often necessitates the need for a porous, structural network to account for volume changes. Figure. 30 (d) shows a comparison between a

silicon IO (ISi) and a carbon-coated silicon IO (C-ISi)⁴⁰⁹. The carbon material deposited onto the IO displayed provided stronger specific capacity retention and helped to maintain the structure of the IO network after 100 cycles.

7 Conclusions and Outlook on the Role of Photonic Crystal Materials

The significance of PhCs across a multitude of different areas has been discussed with particular emphasis on the optical application of the structure. The repeating lattice of alternating dielectric materials found in a PhC can be designed for 1D, 2D and 3D structures with plenty of applications incorporating the optical response of these materials. The properties of the photonic bandgap/stopband associated with a PhC are an essential consideration for any optical application of these structures. As such, the desired wavelength position of the photonic bandgap/stopband for a particular application will dictate the size, geometry and material of the PhC utilised. For creating waveguides using the reflection from a photonic bandgap, such as in hollow core photonic crystal fibers, the highest possible reflectivity from the photonic bandgap is desirable, often utilising silica fibers with a full photonic bandgap to accomplish this. The degree of reflectivity is also a concern for PhC reflectors used in solar cell designs, yet not the only consideration. The specificity of the reflection from the PhC can be designed for selectively reflecting certain wavelength ranges in tandem thin film silicon solar cells. Likewise, the porosity of the PhC back reflectors utilised in DSSC systems is a crucial consideration for enabling the electrolyte to interact with dye-sensitised molecules on the electrode surface.

Certain applications act to suppress the peak reflection altogether, treating PhC reflection as an undesirable effect, such as in photocatalysis. Photocatalysts structured as 3DOM, reap the structural benefits of increased surface area and porosity for catalytic reaction sites and the optical benefits of the slow photon effect at the photonic band edges for increased light path lengths and photocatalytic reaction rates. However, peak reflections from PhCs in photocatalysts are often suppressed using the regions of strong electronic absorption of the semiconductor PhC to ensure that light which may be used for initiating photocatalysis is not wasted by reflections from the photocatalyst surface. Conversely, for applications involving PhC sensors, well-defined, easily-observable and tunable photonic bandgaps/stopbands are of paramount concern for

optically detecting changes in the sensor system. The sensitivity of the peak reflection/transmission dip to minor changes in the material environment or modifications to the structure is the core function of the PhC sensor. The key point illustrated from the many successful examples of implementation from the literature is that the strength of the PhC structure is inherently tied to the flexibility of its signature optical response. Depending on the application, the photonic bandgap can be maximised for reflection, suppressed and tuned for slow photon effects or monitored for material changes simply by control over the dimensions of the repeating structure.

Beyond optical applications, the ordered structure of photonic crystals has attracted attention in certain fields, particularly IO 3DOMs. High surface-to-volume ratios, bi-continuous networks of scaffold material and pores, efficient mass transport and relatively easy functionalisation of the material walls have established IO PhCs as prominent 3DOMs for a range of structural applications^{83 356}. The interconnecting scaffold and porous structure of the IO has found applications in tissue engineering, selectively porous membranes, catalysis and battery electrode architectures. Certain areas, such as photocatalysis, have already begun to capitalise on the structural and optical benefits offered by IO PhCs. Slow photon effects can be introduced into the photocatalyst material via tuning of the optical properties of the IO, while exploiting the structural porosity for increased surface area or incorporation of dye molecules and metal particles. There are numerous examples of IO materials being utilised as photocatalysts to capitalise on synergistic effects between the slow photon effect of the IO structure and existing semiconductor modifications e.g. dye-sensitisation and plasmonic nanoparticle resonances. The slow photon optical activity of the IO structure is used to improve the performance of the semiconductor material.

Moving forward, the potential of PhCs will most likely be realised from identifying areas where the inclusion of an ordered architecture with a signature optical response can enhance or add functionality to existing technologies. Recently, in-situ and operando analysis techniques are a prime example of an emerging application involving IO structures. Structuring existing successful materials as an IO has provided an opportunity to obtain real-time data using a variety of different techniques. When Cu-In alloys used in the electrochemical reduction of CO₂ adopted an IO structure, the Cu-In IO displayed efficient CO₂ reduction

while also allowing a sensitive detection of the CO₂ reduction intermediates using surface-enhanced Raman scattering⁴¹². The inclusion of the IO structure dramatically enhanced the Raman signal of the Cu-In alloy when compared to a structure without an IO design, enabling in-situ Raman analysis due to the enhanced signal. This effect is thought to be facilitated by an electric field enhancement where the high curvature of the IO structure concentrates the electric field creating “hot edges”. A nickel IO used as a structural scaffold for silicon material has demonstrated a capability of operando identification of strain in an anode used for a lithium-ion battery⁴¹³. Silicon is known to experience a volume expansion upon lithiation; on an IO architecture the silicon is free to expand into the IO pores but constrained from expanding into the nickel scaffold, creating a compression on the Ni material. Operando x-ray diffraction monitoring of the strain on the Ni scaffold during lithiation was accomplished using diffraction peak position and peak broadness with the possible identification of amorphous silicon delamination from the scaffold. A similar study⁴¹⁴ has since adapted this in-situ strain measurement technique for Ni₃Sn₂ coated Ni IO anodes.

PhC optical sensors have long demonstrated their capability of acting as in-situ monitors on merit of the sensitivity of the photonic bandgap/stopband. Several of these sensing applications have been highlighted throughout this review. PhC sensors have been developed for identification of solvents^{117 129}, vapors¹⁴⁵, oils¹⁴⁰, ions¹⁵⁵, biomolecules^{154 158} and nerve agents¹⁵⁷ to name just a few. The photonic bandgap of the PhC material defines the sensing response of the structure with systems calibrated to interpret changes to the photonic bandgap position to changes in concentration or structure. Extending this optical sensing ability to incorporate into other functional materials has the potential to establish operando monitoring for different techniques. Recently, a reduced oxide graphene film deposited on the surface of an IO acetylcellulose structure displayed a dual functionality for in-situ monitoring⁴¹⁵. The electrical resistance of the graphene sheet displayed a sensitivity to the tensile/compressive strain applied, allowing human motion to be tracked in-situ via changes in resistance. The IO component of the composite sensor allowed NaCl concentrations to be tracked as function of peak reflection position, with the potential to act as a glucose sensor.

Certainly, the work summarized here acts to further extend the sensing applications of PhC materials in the energy storage field using the optics from solid-state physics, and knowledge of advances in

photoelectrochemistry and related fields. Lithium-ion battery electrodes are now being designed in the form of an IO PhC with reasonably good electrochemical behavior in battery cells, with the added function of an optical sensor arising from the electrode architecture. The presence of an observable photonic stopband allows an operando monitoring of the electrode during battery operation. For lithium-ion batteries, operando characterisation techniques are desirable for the advancing the development of electrode materials due to their potential to provide in-depth information on reaction processes, degradation mechanisms, side reactions, structural evolution, SEI formation and redox mechanisms^{416 417}. X-ray diffraction, microscopy techniques, neutron analysis, scanning probe microscopy, Raman and FTIR spectroscopy are among some of the techniques currently utilised for operando monitoring of lithium-ion batteries. Current research shows ongoing efforts to improve the quality, scale and design of photonic crystal films through mixed oxide precursors¹²⁸, precursor co-assembly with crystalline nanoparticles^{418 236}, increased film wettability during assembly⁴¹⁹, particle-nested double inverse opal structures^{384 420 421} and photonic crystal heterostructures with varying lattice size^{126 422 423} or material composition^{231 424 425}. These various strategies show a concerted effort to achieve large scale crack-free IO photonic crystal films with a strong optical signature. This focus on higher quality films, often with simplified fabrication procedures, should only act to expand the prevalence of IO photonic crystal films in other research areas, particularly in areas which may benefit from an added optical sensor function in addition to the ordered porous network of material present.

Appendix I

Here, the Bragg-Snell model for light diffraction will be derived for the maximum wavelength of destructive interference for light transmission through photonic crystal structures which is indicative of the photonic bandgap position. Technically speaking the condition for maximum constructive interference in the reflected wave is shown, as this corresponds to maximum destructive interference in the transmitted wave. Figure A.1 displays a geometric diagram showing the diffraction angles involved in constructive interference for reflected light waves incident from a medium of refractive index n_1 at some angle θ_1 into a photonic crystal medium of composite refractive index n_{eff} (individual particles of refractive index n_2) with an interplanar spacing d between the photonic crystal planes.

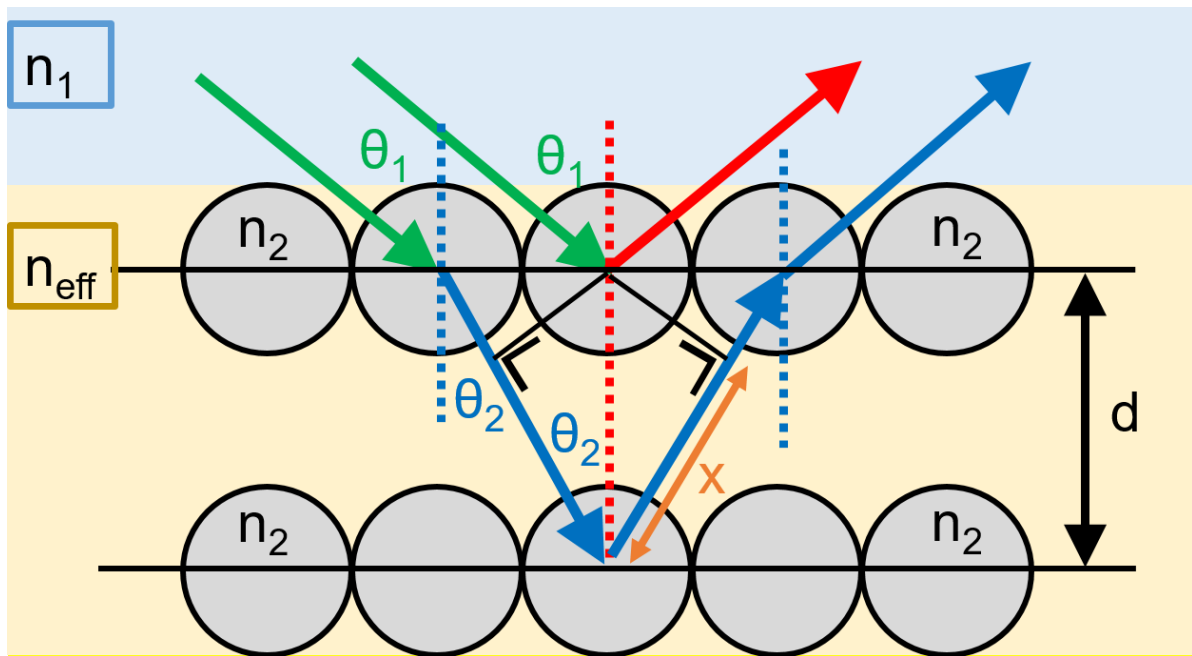


Figure A.1 Schematic diagram showing diffraction from crystal planes in photonic crystal structures as per the Bragg-Snell relation.

With reference to Fig. A.1, two reflected waves (red and blue arrows) from the photonic crystal surface will be in phase and interfere constructively if the path difference of the refracted wave through the medium is an integer number of wavelengths. The path difference created by refraction is labelled x and the light wave travels this distance twice. For some integer m at a wavelength λ' , the condition for constructive interference in the reflected wave, as per thin film interference, is then:

$$m\lambda' = 2x \quad (\text{A.1})$$

The path difference x can be found by taking the cosine of the refracted angle as:

$$x = d \cos \theta_2 \quad (\text{A.2})$$

It is very common to see the refractive index of the photonic crystal medium represented by n_{eff} or n_{avg} , indicating the dependence of the refractive index in the photonic crystal region as some combination of refractive indices of the constituent materials (photonic crystal material + interstitial void space filling). There are different approaches used to estimate the effective refractive index for a photonic crystal medium in the literature. Two of the more common methods used to calculate this parameter for a two material photonic crystal medium (material 1 with refractive index n_1 and volume fraction φ_1 and material 2 with refractive index n_2 and volume fraction φ_2) are given by the models:

$$n_{\text{eff}} = n_1 \varphi_1 + n_2 \varphi_2 \quad (\text{A.3})$$

$$n_{\text{eff}} = \sqrt{n_1^2 \varphi_1 + n_2^2 \varphi_2} \quad (\text{A.4})$$

Unfortunately, there appears to be an unclear consensus on which method is most suitable for estimating n_{eff} for a given system. Here for simplicity, a general n_{eff} term will be used to derive the final form of the Bragg-Snell equation.

The wavelength λ' corresponds to the wavelength of light in the photonic crystal medium as it passes through a refractive index n_{eff} . This can be related to the vacuum wavelength of light λ exterior to the photonic crystal medium with:

$$\lambda' = \frac{\lambda}{n_{\text{eff}}} \quad (\text{A.5})$$

Substituting equations (A.2) and (A.6) back into equation (A.1) yields:

$$\frac{m \lambda}{n_{\text{eff}}} = 2 d \cos \theta_2 \quad (\text{A.6})$$

This can also be written as:

$$m \lambda = 2 d n_{\text{eff}} \cos \theta_2 \quad (\text{A.7})$$

This can be further modified using Snell's law to create a dependence on θ_1 , which is more easily measured/controlled than θ_2 , with Snell's law giving:

$$\sin \theta_2 = \frac{n_1}{n_{\text{eff}}} \sin \theta_1 \quad (\text{A.8})$$

Squaring both sides of the equation and subtracting them from 1 allows equation (A.8) to be rewritten as:

$$1 - \sin^2 \theta_2 = 1 - \frac{n_1^2}{n_{\text{eff}}^2} \sin^2 \theta_1 \quad (\text{A.9})$$

Recognising the left-hand side of equation (A.9) as being equivalent to $\cos^2 \theta_2$, we now have:

$$\cos \theta_2 = \sqrt{1 - \frac{n_1^2}{n_{\text{eff}}^2} \sin^2 \theta_1} \quad (\text{A.10})$$

Equation (A.10) is often further simplified as:

$$\cos \theta_2 = \frac{1}{n_{\text{eff}}} \sqrt{n_{\text{eff}}^2 - n_1^2 \sin^2 \theta_1} \quad (\text{A.11})$$

Substitution of this form of $\cos \theta_2$ into equation (A.7) creates a constructive interference condition for reflected light as:

$$m \lambda = 2 d \sqrt{n_{\text{eff}}^2 - n_1^2 \sin^2 \theta_1} \quad (\text{A.12})$$

Equation (A.12) is a general form for the maximum reflected constructive interference wavelength in photonic crystal structures which depends on interplanar spacing d , composite refractive index in the photonic crystal medium n_{eff} , refractive index of the surrounding medium n_1 and the angle of incidence for light entering the structure. For opal and inverse opal structures the interplanar spacing of the (111) reflection, the most prominent reflection at normal incidence, using the unit cell parameter can be found as:

$$d_{hkl} = \frac{a}{\sqrt{h^2 + k^2 + l^2}} \quad (\text{A.13})$$

$$d_{111} = \frac{\sqrt{2} D}{\sqrt{3}} \quad (\text{A.14})$$

The parameter D represents the centre-to-centre distance between adjacent spheres/IO pores for photonic crystal structures. For reflections from the (111) plane in FCC structured photonic crystals the condition for constructive interference can be written as:

$$m \lambda = \sqrt{\frac{8}{3}} D \sqrt{n_{\text{eff}}^2 - n_1^2 \sin^2 \theta_1} \quad (\text{A.15})$$

This form of the constructive interference condition is often presented when working with photonic crystal structures. If the photonic crystal is placed in an air medium ($n_1 = 1$) and a first order resonance ($m = 1$) is being measured, this equation can also be seen represented as:

$$\lambda = 1.633 D \sqrt{n_{\text{eff}}^2 - \sin^2 \theta_1} \quad (\text{A.16})$$

Acknowledgments

We acknowledge support from the Irish Research Council Government of Ireland Postgraduate Scholarship under award no. GOIPG/2016/946. We also acknowledge funding from the Irish Research Council Advanced Laureate Award under grant no. IRCLA/2019/118.

References

1. Xia, Y.; Rogers, J. A.; Paul, K. E.; Whitesides, G. M., Unconventional Methods for Fabricating and Patterning Nanostructures. *Chemical Reviews* **1999**, *99* (7), 1823-1848.
2. Xiao, M.; Wang, Z.; Lyu, M.; Luo, B.; Wang, S.; Liu, G.; Cheng, H.-M.; Wang, L., Hollow Nanostructures for Photocatalysis: Advantages and Challenges. *Advanced Materials* **2019**, *31* (38), 1801369.
3. Centi, G.; Perathoner, S., The Role of Nanostructure in Improving the Performance of Electrodes for Energy Storage and Conversion. *European Journal of Inorganic Chemistry* **2009**, *2009* (26), 3851-3878.
4. Goldberg, M.; Langer, R.; Jia, X., Nanostructured materials for applications in drug delivery and tissue engineering. *Journal of Biomaterials Science, Polymer Edition* **2007**, *18* (3), 241-268.
5. Bruce, P. G.; Scrosati, B.; Tarascon, J.-M., Nanomaterials for Rechargeable Lithium Batteries. *Angewandte Chemie International Edition* **2008**, *47* (16), 2930-2946.
6. Holzinger, M.; Le Goff, A.; Cosnier, S., Nanomaterials for biosensing applications: a review. *Frontiers in Chemistry* **2014**, *2* (63).

7. Cao, L.; Fan, P.; Barnard, E. S.; Brown, A. M.; Brongersma, M. L., Tuning the Color of Silicon Nanostructures. *Nano Letters* **2010**, *10* (7), 2649-2654.
8. Fang, Z.; Zhu, X., Plasmonics in Nanostructures. *Advanced Materials* **2013**, *25* (28), 3840-3856.
9. Rycenga, M.; Cobley, C. M.; Zeng, J.; Li, W.; Moran, C. H.; Zhang, Q.; Qin, D.; Xia, Y., Controlling the Synthesis and Assembly of Silver Nanostructures for Plasmonic Applications. *Chemical Reviews* **2011**, *111* (6), 3669-3712.
10. Sun, J.; Bhushan, B.; Tong, J., Structural coloration in nature. *RSC Advances* **2013**, *3* (35), 14862-14889.
11. Fu, Y.; Tippets, C. A.; Donev, E. U.; Lopez, R., Structural colors: from natural to artificial systems. *WIREs Nanomedicine and Nanobiotechnology* **2016**, *8* (5), 758-775.
12. Kinoshita, S.; Yoshioka, S., Structural Colors in Nature: The Role of Regularity and Irregularity in the Structure. *ChemPhysChem* **2005**, *6* (8), 1442-1459.
13. Xu, J.; Guo, Z., Biomimetic photonic materials with tunable structural colors. *Journal of Colloid and Interface Science* **2013**, *406*, 1-17.
14. Piszter, G.; Kertész, K.; Bálint, Z.; Biró, L. P., Variability of the Structural Coloration in Two Butterfly Species with Different Prezygotic Mating Strategies. *PLOS ONE* **2016**, *11* (11), e0165857.
15. Vigneron, J. P.; Simonis, P., Natural photonic crystals. *Physica B: Condensed Matter* **2012**, *407* (20), 4032-4036.
16. Poladian, L.; Wickham, S.; Lee, K.; Large, M. C. J., Iridescence from photonic crystals and its suppression in butterfly scales. *Journal of The Royal Society Interface* **2009**, *6* (suppl_2), S233-S242.
17. Gu, Z.-Z.; Uetsuka, H.; Takahashi, K.; Nakajima, R.; Onishi, H.; Fujishima, A.; Sato, O., Structural Color and the Lotus Effect. *Angewandte Chemie International Edition* **2003**, *42* (8), 894-897.
18. Kuang, M.; Wang, J.; Jiang, L., Bio-inspired photonic crystals with superwettability. *Chemical Society Reviews* **2016**, *45* (24), 6833-6854.
19. Wang, J.; Zhang, Y.; Wang, S.; Song, Y.; Jiang, L., Bioinspired Colloidal Photonic Crystals with Controllable Wettability. *Accounts of Chemical Research* **2011**, *44* (6), 405-415.
20. Sato, O.; Kubo, S.; Gu, Z.-Z., Structural Color Films with Lotus Effects, Superhydrophilicity, and Tunable Stop-Bands. *Accounts of Chemical Research* **2009**, *42* (1), 1-10.
21. Samaha, M. A.; Tafreshi, H. V.; Gad-el-Hak, M., Superhydrophobic surfaces: From the lotus leaf to the submarine. *Comptes Rendus Mécanique* **2012**, *340* (1), 18-34.
22. Didari, A.; Mengüç, M. P., A biomimicry design for nanoscale radiative cooling applications inspired by Morpho didius butterfly. *Scientific Reports* **2018**, *8* (1), 16891.
23. Saito, A., Material design and structural color inspired by biomimetic approach. *Science and Technology of Advanced Materials* **2011**, *12* (6), 064709.
24. Latthe, S.; Terashima, C.; Nakata, K.; Fujishima, A., Superhydrophobic Surfaces Developed by Mimicking Hierarchical Surface Morphology of Lotus Leaf. *Molecules (Basel, Switzerland)* **2014**, *19*, 4256-83.
25. Ensikat, H. J.; Ditsche-Kuru, P.; Neinhuis, C.; Barthlott, W., Superhydrophobicity in perfection: the outstanding properties of the lotus leaf. *Beilstein Journal of Nanotechnology* **2011**, *2*, 152 - 161.
26. Zi, J.; Yu, X.; Li, Y.; Hu, X.; Xu, C.; Wang, X.; Liu, X.; Fu, R., Coloration strategies in peacock feathers. *Proceedings of the National Academy of Sciences* **2003**, *100* (22), 12576.
27. Liu, F.; Dong, B. Q.; Liu, X. H.; Zheng, Y. M.; Zi, J., Structural color change in longhorn beetles *Tmesisternus isabellae*. *Opt. Express* **2009**, *17* (18), 16183-16191.
28. Martin, E.; Gaillou, E., Insight on gem opal formation in volcanic ash deposits from a supereruption: A case study through oxygen and hydrogen isotopic composition of opals from Lake Tecopa, California, U.S.A. *American Mineralogist* **2018**, *103* (5), 803-811.
29. Gaillou, E. s.; Fritsch, E.; Aguilar-Reyes, B.; Rondeau, B.; Post, J.; Barreau, A.; Ostroumov, M., Common gem opal: An investigation of micro- to nano-structure. *American Mineralogist* **2008**, *93* (11-12), 1865-1873.
30. McPhedran, R. C.; Nicorovici, N. A.; McKenzie, D. R.; Botten, L. C.; Parker, A. R.; Rouse, G. W., The Sea Mouse and the Photonic Crystal. *Australian Journal of Chemistry* **2001**, *54* (4), 241-244.

31. McPhedran, R. C.; Nicorovici, N. A.; McKenzie, D. R.; Rouse, G. W.; Botten, L. C.; Welch, V.; Parker, A. R.; Wohlgennant, M.; Vardeny, V., Structural colours through photonic crystals. *Physica B: Condensed Matter* **2003**, *338* (1), 182-185.
32. Jacobs, M.; Lopez-Garcia, M.; Phrathep, O. P.; Lawson, T.; Oulton, R.; Whitney, H. M., Photonic multilayer structure of Begonia chloroplasts enhances photosynthetic efficiency. *Nature Plants* **2016**, *2* (11), 16162.
33. Bhushan, B., Biomimetics: lessons from nature—an overview. *Philosophical Transactions of the Royal Society A: Mathematical, Physical and Engineering Sciences* **2009**, *367* (1893), 1445-1486.
34. Tamerler, C.; Sarikaya, M., Molecular biomimetics: Utilizing nature's molecular ways in practical engineering. *Acta Biomaterialia* **2007**, *3* (3), 289-299.
35. Parker, A. R.; Townley, H. E., Biomimetics of photonic nanostructures. *Nature Nanotechnology* **2007**, *2* (6), 347-353.
36. Koch, K.; Bhushan, B.; Barthlott, W., Multifunctional surface structures of plants: An inspiration for biomimetics. *Progress in Materials Science* **2009**, *54* (2), 137-178.
37. Porter, J. R.; Ruckh, T. T.; Popat, K. C., Bone tissue engineering: A review in bone biomimetics and drug delivery strategies. *Biotechnology Progress* **2009**, *25* (6), 1539-1560.
38. Barthelat, F., Biomimetics for next generation materials. *Philosophical Transactions of the Royal Society A: Mathematical, Physical and Engineering Sciences* **2007**, *365* (1861), 2907-2919.
39. Mayer, G.; Sarikaya, M., Rigid biological composite materials: Structural examples for biomimetic design. *Experimental Mechanics* **2002**, *42* (4), 395-403.
40. Luz, G. M.; Mano, J. F., Biomimetic design of materials and biomaterials inspired by the structure of nacre. *Philosophical Transactions of the Royal Society A: Mathematical, Physical and Engineering Sciences* **2009**, *367* (1893), 1587-1605.
41. Lin, J.; Cai, Y.; Wang, X.; Ding, B.; Yu, J.; Wang, M., Fabrication of biomimetic superhydrophobic surfaces inspired by lotus leaf and silver ragwort leaf. *Nanoscale* **2011**, *3* (3), 1258-1262.
42. Xu, Q.; Zhang, W.; Dong, C.; Sreepasad, T. S.; Xia, Z., Biomimetic self-cleaning surfaces: synthesis, mechanism and applications. *Journal of The Royal Society Interface* **2016**, *13* (122), 20160300.
43. Clapham, P. B.; Hutley, M. C., Reduction of Lens Reflexion by the "Moth Eye" Principle. *Nature* **1973**, *244*, 281.
44. Raut, H. K.; Ganesh, V. A.; Nair, A. S.; Ramakrishna, S., Anti-reflective coatings: A critical, in-depth review. *Energy & Environmental Science* **2011**, *4* (10), 3779-3804.
45. Nam, S.-H.; Boo, J.-H., Fabrication of moth-eye patterned TiO₂ active layers for high energy efficiency and current density of dye-sensitized solar cells. *Energy Reports* **2022**, *8*, 98-105.
46. Barthelat, F.; Tang, H.; Zavattieri, P. D.; Li, C. M.; Espinosa, H. D., On the mechanics of mother-of-pearl: A key feature in the material hierarchical structure. *Journal of the Mechanics and Physics of Solids* **2007**, *55* (2), 306-337.
47. Li, X.; Chang, W.-C.; Chao, Y. J.; Wang, R.; Chang, M., Nanoscale Structural and Mechanical Characterization of a Natural Nanocomposite Material: The Shell of Red Abalone. *Nano Letters* **2004**, *4* (4), 613-617.
48. Atlan, G.; Delattre, O.; Berland, S.; LeFaou, A.; Nabias, G.; Cot, D.; Lopez, E., Interface between bone and nacre implants in sheep. *Biomaterials* **1999**, *20* (11), 1017-1022.
49. Berland, S.; Delattre, O.; Borzeix, S.; Catonné, Y.; Lopez, E., Nacre/bone interface changes in durable nacre endosseous implants in sheep. *Biomaterials* **2005**, *26* (15), 2767-2773.
50. Robert, B.; Arnaud, D.; Michael, H.; Matthias, B.; Theobald, L.; Joachim, P. S. In *Product piracy from nature: biomimetic microstructures and interfaces for high-performance optics*, Proc.SPIE, 2008.
51. Sun, J.; Wang, X.; Wu, J.; Jiang, C.; Shen, J.; Cooper, M. A.; Zheng, X.; Liu, Y.; Yang, Z.; Wu, D., Biomimetic moth-eye nanofabrication: enhanced antireflection with superior self-cleaning characteristic. *Scientific Reports* **2018**, *8* (1), 5438.
52. Navarro-Baena, I.; Jacobo-Martín, A.; Hernández, J. J.; Castro Smirnov, J. R.; Viela, F.; Monclús, M. A.; Osorio, M. R.; Molina-Aldareguia, J. M.; Rodríguez, I., Single-imprint moth-eye anti-reflective and self-cleaning film with enhanced resistance. *Nanoscale* **2018**, *10* (33), 15496-15504.
53. Yablonovitch, E., Inhibited Spontaneous Emission in Solid-State Physics and Electronics. *Physical Review Letters* **1987**, *58* (20), 2059-2062.

54. John, S., Strong localization of photons in certain disordered dielectric superlattices. *Physical Review Letters* **1987**, *58* (23), 2486-2489.
55. Johnson, S. G.; Joannopoulos, J. D., Three-dimensionally periodic dielectric layered structure with omnidirectional photonic band gap. *Applied Physics Letters* **2000**, *77* (22), 3490-3492.
56. Vlasov, Y. A.; Astratov, V. N.; Karimov, O. Z.; Kaplyanskiy, A. A.; Bogomolov, V. N.; Prokofiev, A. V., Existence of a photonic pseudogap for visible light in synthetic opals. *Physical Review B* **1997**, *55* (20), R13357-R13360.
57. Biswas, R.; Sigalas, M. M.; Subramania, G.; Soukoulis, C. M.; Ho, K. M., Photonic band gaps of porous solids. *Physical Review B* **2000**, *61* (7), 4549-4553.
58. Joannopoulos, J. D.; Villeneuve, P. R.; Fan, S., Photonic crystals: putting a new twist on light. *Nature* **1997**, *386* (6621), 143-149.
59. Armstrong, E.; O'Dwyer, C., Artificial opal photonic crystals and inverse opal structures – fundamentals and applications from optics to energy storage. *Journal of Materials Chemistry C* **2015**, *3* (24), 6109-6143.
60. Shen, H.; Wang, Z.; Wu, Y.; Yang, B., One-dimensional photonic crystals: fabrication, responsiveness and emerging applications in 3D construction. *RSC Advances* **2016**, *6* (6), 4505-4520.
61. De Dood, M. J. A.; Snoeks, E.; Moroz, A.; Polman, A., Design and optimization of 2D photonic crystal waveguides based on silicon. *Optical and Quantum Electronics* **2002**, *34* (1), 145-159.
62. Kalra, Y.; Sinha, R. K., Photonic band gap engineering in 2D photonic crystals. *Pramana* **2006**, *67* (6), 1155-1164.
63. Philipse, A. P., Solid opaline packings of colloidal silica spheres. *Journal of Materials Science Letters* **1989**, *8* (12), 1371-1373.
64. Zakhidov, A. A.; Baughman, R. H.; Iqbal, Z.; Cui, C.; Khayrullin, I.; Dantas, S. O.; Marti, J.; Ralchenko, V. G., Carbon Structures with Three-Dimensional Periodicity at Optical Wavelengths. *Science* **1998**, *282* (5390), 897.
65. Yablonovitch, E.; Gmitter, T. J.; Leung, K. M., Photonic band structure: The face-centered-cubic case employing nonspherical atoms. *Physical Review Letters* **1991**, *67* (17), 2295-2298.
66. Ho, K. M.; Chan, C. T.; Soukoulis, C. M.; Biswas, R.; Sigalas, M., Photonic band gaps in three dimensions: New layer-by-layer periodic structures. *Solid State Communications* **1994**, *89* (5), 413-416.
67. Choi, S. Y.; Mamak, M.; von Freymann, G.; Chopra, N.; Ozin, G. A., Mesoporous Bragg Stack Color Tunable Sensors. *Nano Letters* **2006**, *6* (11), 2456-2461.
68. Hung, Y., Jr.; Lee, S.-L.; Coldren, L. A., Deep and tapered silicon photonic crystals for achieving anti-reflection and enhanced absorption. *Opt. Express* **2010**, *18* (7), 6841-6852.
69. Rakich, P. T.; Dahlem, M. S.; Tandon, S.; Ibanescu, M.; Soljačić, M.; Petrich, G. S.; Joannopoulos, J. D.; Kolodziejski, L. A.; Ippen, E. P., Achieving centimetre-scale supercollimation in a large-area two-dimensional photonic crystal. *Nature Materials* **2006**, *5* (2), 93-96.
70. Gratson, G. M.; García-Santamaría, F.; Lousse, V.; Xu, M.; Fan, S.; Lewis, J. A.; Braun, P. V., Direct-Write Assembly of Three-Dimensional Photonic Crystals: Conversion of Polymer Scaffolds to Silicon Hollow-Woodpile Structures. *Advanced Materials* **2006**, *18* (4), 461-465.
71. Shishkin, I. I.; Samusev, K. B.; Rybin, M. V.; Limonov, M. F.; Kivshar, Y. S.; Gaidukeviciute, A.; Kiyan, R. V.; Chichkov, B. N., Inverted yablonovite fabricated by the direct laser writing method and its photonic structure. *JETP Letters* **2012**, *95* (9), 457-461.
72. Gu, Z.-Z.; Kubo, S.; Qian, W.; Einaga, Y.; Tryk, D. A.; Fujishima, A.; Sato, O., Varying the Optical Stop Band of a Three-Dimensional Photonic Crystal by Refractive Index Control. *Langmuir* **2001**, *17* (22), 6751-6753.
73. Schroden, R. C.; Al-Daous, M.; Blanford, C. F.; Stein, A., Optical Properties of Inverse Opal Photonic Crystals. *Chemistry of Materials* **2002**, *14* (8), 3305-3315.
74. Ge, J.; Hu, Y.; Yin, Y., Highly Tunable Superparamagnetic Colloidal Photonic Crystals. *Angewandte Chemie International Edition* **2007**, *46* (39), 7428-7431.
75. Han, M. G.; Shin, C. G.; Jeon, S.-J.; Shim, H.; Heo, C.-J.; Jin, H.; Kim, J. W.; Lee, S., Full Color Tunable Photonic Crystal from Crystalline Colloidal Arrays with an Engineered Photonic Stop-Band. *Advanced Materials* **2012**, *24* (48), 6438-6444.

76. Nair, R. V.; Vijaya, R., Photonic crystal sensors: An overview. *Progress in Quantum Electronics* **2010**, *34* (3), 89-134.
77. Wang, H.; Zhang, K.-Q., Photonic Crystal Structures with Tunable Structure Color as Colorimetric Sensors. *Sensors* **2013**, *13* (4).
78. Kawamura, A.; Kohri, M.; Morimoto, G.; Nannichi, Y.; Taniguchi, T.; Kishikawa, K., Full-Color Biomimetic Photonic Materials with Iridescent and Non-Iridescent Structural Colors. *Scientific Reports* **2016**, *6* (1), 33984.
79. Rashid, I.; Hassan, M. U.; Nazim, M.; Elsharif, M.; Dou, Q.; Hu, D.; Kamran, M.; Dai, Q.; Butt, H., Structural colouration in the Himalayan monal, hydrophobicity and refractive index modulated sensing. *Nanoscale* **2020**, *12* (41), 21409-21419.
80. Sato, O.; Kubo, S.; Gu, Z., Structural color films with lotus effects, superhydrophilicity, and tunable stop-bands. *Accounts of Chemical Research* **2009**, *42* 1, 1-10.
81. Waterhouse, G. I. N.; Chen, W.-T.; Chan, A.; Sun-Waterhouse, D., Achieving Color and Function with Structure: Optical and Catalytic Support Properties of ZrO₂ Inverse Opal Thin Films. *ACS Omega* **2018**, *3* (8), 9658-9674.
82. Stein, A.; Schroden, R. C., Colloidal crystal templating of three-dimensionally ordered macroporous solids: materials for photonics and beyond. *Current Opinion in Solid State and Materials Science* **2001**, *5* (6), 553-564.
83. Stein, A.; Li, F.; Denny, N. R., Morphological Control in Colloidal Crystal Templating of Inverse Opals, Hierarchical Structures, and Shaped Particles. *Chemistry of Materials* **2008**, *20* (3), 649-666.
84. Sumioka, K.; Kayashima, H.; Tsutsui, T., Tuning the Optical Properties of Inverse Opal Photonic Crystals by Deformation. *Advanced Materials* **2002**, *14* (18), 1284-1286.
85. Aguirre, C. I.; Reguera, E.; Stein, A., Tunable Colors in Opals and Inverse Opal Photonic Crystals. *Advanced Functional Materials* **2010**, *20* (16), 2565-2578.
86. Arsenault, A. C.; Puzzo, D. P.; Manners, I.; Ozin, G. A., Photonic-crystal full-colour displays. *Nature Photonics* **2007**, *1* (8), 468-472.
87. Arsenault, A. C.; Míguez, H.; Kitaev, V.; Ozin, G. A.; Manners, I., A Polychromic, Fast Response Metallopolymer Gel Photonic Crystal with Solvent and Redox Tunability: A Step Towards Photonic Ink (P-Ink). *Advanced Materials* **2003**, *15* (6), 503-507.
88. Hu, H.; Chen, Q.-W.; Tang, J.; Hu, X.-Y.; Zhou, X.-H., Photonic anti-counterfeiting using structural colors derived from magnetic-responsive photonic crystals with double photonic bandgap heterostructures. *Journal of Materials Chemistry* **2012**, *22* (22), 11048-11053.
89. Hu, H.; Zhong, H.; Chen, C.; Chen, Q., Magnetically responsive photonic watermarks on banknotes. *Journal of Materials Chemistry C* **2014**, *2* (19), 3695-3702.
90. Huang, H.; Li, H.; Shen, X.; Gu, K.; Guo, J.; Wang, C., Gecko-inspired smart photonic crystal films with versatile color and brightness variation for smart windows. *Chemical Engineering Journal* **2022**, *429*, 132437.
91. Kim, J. B.; Chae, C.; Han, S. H.; Lee, S. Y.; Kim, S.-H., Direct writing of customized structural-color graphics with colloidal photonic inks. *Science Advances* **2021**, *7* (48), eabj8780.
92. Wang, C.; Lin, X.; Schäfer, C. G.; Hirsemann, S.; Ge, J., Spray Synthesis of Photonic Crystal Based Automotive Coatings with Bright and Angular-Dependent Structural Colors. *Advanced Functional Materials* **2021**, *31* (9), 2008601.
93. Kim, T.; Lee, J. W.; Park, C.; Lee, K.; Lee, C. E.; Lee, S.; Kim, Y.; Kim, S.; Jeon, S.; Ryu, D. Y.; Koh, W.-G.; Park, C., Self-powered finger motion-sensing structural color display enabled by block copolymer photonic crystal. *Nano Energy* **2022**, *92*, 106688.
94. Shi, X.; He, J.; Xie, X.; Dou, R.; Lu, X., Photonic crystals with vivid structure color and robust mechanical strength. *Dyes and Pigments* **2019**, *165*, 137-143.
95. Li, S.; Jia, L.; Dong, P.; Shan, G.; Liu, R., Construction of photonic crystal structural colors on white polyester fabrics. *Optical Materials* **2021**, *116*, 111115.
96. Wang, X.; Li, Y.; Zhao, Q.; Liu, G.; Chai, L.; Zhou, L.; Fan, Q.; Shao, J., High Structural Stability of Photonic Crystals on Textile Substrates, Prepared via a Surface-Supported Curing Strategy. *ACS Applied Materials & Interfaces* **2021**, *13* (16), 19221-19229.

97. Fu, G.; Zhang, X.; Chu, X.; Zhou, Y.; Peng, X.; Chen, Y.; Su, M.; Kuang, M.; Song, Y., Rapid fabrication of photonic crystal patterns with iridescent structural colors on textiles by spray coating. *Dyes and Pigments* **2021**, *195*, 109747.
98. Topçu, G.; Güner, T.; Demir, M. M., Non-iridescent structural colors from uniform-sized SiO₂ colloids. *Photonics and Nanostructures - Fundamentals and Applications* **2018**, *29*, 22-29.
99. Feng, Y.; Sun, J.; Xu, L.; Hong, W., Angle-Independent Structurally Colored Materials with Superhydrophobicity and Self-Healing Capability. *Advanced Materials Interfaces* **2021**, *8* (7), 2001950.
100. Shang, G.; Eich, M.; Petrov, A., Photonic glass based structural color. *APL Photonics* **2020**, *5* (6), 060901.
101. Núñez-Montenegro, A.; Crista, D. M. A.; da Silva, J. C. G. E., Structural coloration based on photonic crystals for coating applications on wood. *European Journal of Wood and Wood Products* **2020**, *78* (2), 293-300.
102. Liu, Y.; Hu, J., Investigation of Polystyrene-Based Microspheres from Different Copolymers and Their Structural Color Coatings on Wood Surface. *Coatings* **2021**, *11* (1).
103. Burgess, I. B.; Mishchenko, L.; Hatton, B. D.; Kolle, M.; Lončar, M.; Aizenberg, J., Encoding Complex Wettability Patterns in Chemically Functionalized 3D Photonic Crystals. *Journal of the American Chemical Society* **2011**, *133* (32), 12430-12432.
104. Chen, J.; Liu, P.; Du, X.; Xie, Z., Clickable Colloidal Photonic Crystals for Structural Color Pattern. *Langmuir* **2018**, *34* (44), 13219-13224.
105. Qi, Y.; Niu, W.; Zhang, S.; Wu, S.; Chu, L.; Ma, W.; Tang, B., Encoding and Decoding of Invisible Complex Information in a Dual-Response Bilayer Photonic Crystal with Tunable Wettability. *Advanced Functional Materials* **2019**, *29* (48), 1906799.
106. Xiao, X.; Yang, Z.; Yu, Q.; Shi, D.; Dong, W.; Zhang, H.; Chen, M., Multiple Response Colors of Invisible Hollow Silica Photonic Crystals Patterns for Information Encoding. *Advanced Materials Interfaces* **2021**, *8* (16), 2100814.
107. Wu, S.; Liu, T.; Tang, B.; Li, L.; Zhang, S., Different Structural Colors or Patterns on the Front and Back Sides of a Multilayer Photonic Structure. *ACS Applied Materials & Interfaces* **2019**, *11* (30), 27210-27215.
108. Wu, S.; Liu, T.; Tang, B.; Li, L.; Zhang, S., Structural Color Circulation in a Bilayer Photonic Crystal by Increasing the Incident Angle. *ACS Applied Materials & Interfaces* **2019**, *11* (10), 10171-10177.
109. Zhang, Y.; Qi, Y.; Wang, R.; Cao, T.; Ma, W.; Zhang, S., Nonintrusively Adjusting Structural Colors of Sealed Two-Dimensional Photonic Crystals: Immediate Transformation between Transparency and Intense Iridescence and Their Applications. *ACS Applied Materials & Interfaces* **2021**, *13* (11), 13861-13871.
110. Vu, A.; Qian, Y.; Stein, A., Porous Electrode Materials for Lithium-Ion Batteries – How to Prepare Them and What Makes Them Special. *Advanced Energy Materials* **2012**, *2* (9), 1056-1085.
111. McNulty, D.; Carroll, E.; O'Dwyer, C., Rutile TiO₂ Inverse Opal Anodes for Li-Ion Batteries with Long Cycle Life, High-Rate Capability, and High Structural Stability. *Advanced Energy Materials* **2017**, *7* (12), 1602291.
112. Curti, M.; Schneider, J.; Bahnemann, D. W.; Mendive, C. B., Inverse Opal Photonic Crystals as a Strategy to Improve Photocatalysis: Underexplored Questions. *The Journal of Physical Chemistry Letters* **2015**, *6* (19), 3903-3910.
113. Tan, T.; Xie, W.; Zhu, G.; Shan, J.; Xu, P.; Li, L.; Wang, J., Fabrication and photocatalysis of BiFeO₃ with inverse opal structure. *Journal of Porous Materials* **2015**, *22* (3), 659-663.
114. Zhang, Y. S.; Choi, S.-W.; Xia, Y., Inverse opal scaffolds for applications in regenerative medicine. *Soft Matter* **2013**, *9* (41), 9747-9754.
115. Zhang, Y. S.; Zhu, C.; Xia, Y., Inverse Opal Scaffolds and Their Biomedical Applications. *Advanced Materials* **2017**, *29* (33), 1701115.
116. Blanford, C. F.; Schroden, R. C.; Al-Daous, M.; Stein, A., Tuning Solvent-Dependent Color Changes of Three-Dimensionally Ordered Macroporous (3DOM) Materials Through Compositional and Geometric Modifications. *Advanced Materials* **2001**, *13* (1), 26-29.
117. Waterhouse, G. I. N.; Chen, W.-T.; Chan, A.; Jin, H.; Sun-Waterhouse, D.; Cowie, B. C. C., Structural, Optical, and Catalytic Support Properties of γ -Al₂O₃ Inverse Opals. *The Journal of Physical Chemistry C* **2015**, *119* (12), 6647-6659.

118. Johnson, N. P.; McComb, D. W.; Richel, A.; Treble, B. M.; De La Rue, R. M., Synthesis and optical properties of opal and inverse opal photonic crystals. *Synthetic Metals* **2001**, *116* (1), 469-473.
119. Chiappini, A.; Armellini, C.; Chiasera, A.; Ferrari, M.; Jestin, Y.; Mattarelli, M.; Montagna, M.; Moser, E.; Nunzi Conti, G.; Pelli, S.; Righini, G. C.; Clara Gonçalves, M.; Almeida, R. M., Design of photonic structures by sol-gel-derived silica nanospheres. *Journal of Non-Crystalline Solids* **2007**, *353* (5), 674-678.
120. Cheng, B.; Ni, P.; Jin, C.; Li, Z.; Zhang, D.; Dong, P.; Guo, X., More direct evidence of the fcc arrangement for artificial opal. *Optics Communications* **1999**, *170* (1), 41-46.
121. Ni, P.; Dong, P.; Cheng, B.; Li, X.; Zhang, D., Synthetic SiO₂ Opals. *Advanced Materials* **2001**, *13* (6), 437-441.
122. Lonergan, A.; McNulty, D.; O'Dwyer, C., Tetrahedral framework of inverse opal photonic crystals defines the optical response and photonic band gap. *Journal of Applied Physics* **2018**, *124* (9), 095106.
123. Phillips, K. R.; Vogel, N.; Hu, Y.; Kolle, M.; Perry, C. C.; Aizenberg, J., Tunable Anisotropy in Inverse Opals and Emerging Optical Properties. *Chemistry of Materials* **2014**, *26* (4), 1622-1628.
124. Hwang, D.-K.; Noh, H.; Cao, H.; Chang, R. P. H., Photonic bandgap engineering with inverse opal multistacks of different refractive index contrasts. *Applied Physics Letters* **2009**, *95* (9), 091101.
125. Cao, Y.; Wang, Y.; Zhu, Y.; Chen, H.; Li, Z.; Ding, J.; Chi, Y., Fabrication of anatase titania inverse opal films using polystyrene templates. *Superlattices and Microstructures* **2006**, *40* (3), 155-160.
126. Lee, H. S.; Kubrin, R.; Zierold, R.; Petrov, A. Y.; Nielsch, K.; Schneider, G. A.; Eich, M., Photonic properties of titania inverse opal heterostructures. *Opt. Mater. Express* **2013**, *3* (8), 1007-1019.
127. Zhou, Z.; Zhao, X. S., Opal and Inverse Opal Fabricated with a Flow-Controlled Vertical Deposition Method. *Langmuir* **2005**, *21* (10), 4717-4723.
128. Phillips, K. R.; Shirman, T.; Aizenberg, M.; England, G. T.; Vogel, N.; Aizenberg, J., Silica-titania hybrids for structurally robust inverse opals with controllable refractive index. *Journal of Materials Chemistry C* **2020**, *8* (1), 109-116.
129. Lonergan, A.; Hu, C.; O'Dwyer, C., Filling in the gaps: The nature of light transmission through solvent-filled inverse opal photonic crystals. *Physical Review Materials* **2020**, *4* (6), 065201.
130. Waterhouse, G. I. N.; Metson, J. B.; Idriss, H.; Sun-Waterhouse, D., Physical and Optical Properties of Inverse Opal CeO₂ Photonic Crystals. *Chemistry of Materials* **2008**, *20* (3), 1183-1190.
131. Kuo, W.-K.; Weng, H.-P.; Hsu, J.-J.; Yu, H. H., Photonic Crystal-Based Sensors for Detecting Alcohol Concentration. *Applied Sciences* **2016**, *6* (3).
132. Kuo, C.-Y.; Lu, S.-Y.; Chen, S.; Bernards, M.; Jiang, S., Stop band shift based chemical sensing with three-dimensional opal and inverse opal structures. *Sensors and Actuators B: Chemical* **2007**, *124* (2), 452-458.
133. Amrehn, S.; Wu, X.; Schumacher, C.; Wagner, T., Photonic crystal-based fluid sensors: Toward practical application. *physica status solidi (a)* **2015**, *212* (6), 1266-1272.
134. Ashurov, M. S.; Ikrami, S. A.; Klimonsky, S. O., Photonic Crystal Sensors for the Composition of Liquids Based on Films with the Structure of Inverse Opal. *Inorganic Materials: Applied Research* **2021**, *12* (4), 915-921.
135. Ashurov, M.; Gorelik, V.; Napolskii, K.; Klimonsky, S., Anodic Alumina Photonic Crystals as Refractive Index Sensors for Controlling the Composition of Liquid Mixtures. *Photonic Sensors* **2020**, *10* (2), 147-154.
136. Yu, Y.; Brandt, S.; Nicolas, N. J.; Aizenberg, J., Colorimetric Ethanol Indicator Based on Instantaneous, Localized Wetting of a Photonic Crystal. *ACS Applied Materials & Interfaces* **2020**, *12* (1), 1924-1929.
137. Heshmat, M.; Li, P. C. H., Construction of an Array of Photonic Crystal Films for Visual Differentiation of Water/Ethanol Mixtures. *ACS Omega* **2019**, *4* (22), 19991-19999.
138. Hongbo, X.; Dan, L.; Suli, W.; Shuai, F.; Chao, M.; Bin, D., H₂O- and ethanol concentration-responsive polymer/gel inverse opal photonic crystal. *Journal of Colloid and Interface Science* **2022**, *605*, 803-812.
139. Rashidi, M.-R.; Ahmadi-Kandjani, S.; Chaghmirzaei, P.; Shirforoush Sattari, M.; Fathi, F., Investigation of optical images in inverse opal photonic crystal films for sensing applications; a non-destructive method. *Optical Materials* **2022**, *125*, 112072.

140. Li, H.; Chang, L.; Wang, J.; Yang, L.; Song, Y., A colorful oil-sensitive carbon inverse opal. *Journal of Materials Chemistry* **2008**, *18* (42), 5098-5103.
141. Sedighi, A.; Qiu, S.; Wong, M. C. K.; Li, P. C. H., Dip-in Indicators for Visual Differentiation of Fuel Mixtures Based on Wettability of Fluoroalkylchlorosilane-Coated Inverse Opal Films. *ACS Applied Materials & Interfaces* **2015**, *7* (51), 28387-28392.
142. Kou, D.; Zhang, Y.; Zhang, S.; Wu, S.; Ma, W., High-sensitive and stable photonic crystal sensors for visual detection and discrimination of volatile aromatic hydrocarbon vapors. *Chemical Engineering Journal* **2019**, *375*, 121987.
143. Yang, H.; Pan, L.; Han, Y.; Ma, L.; Li, Y.; Xu, H.; Zhao, J., A visual water vapor photonic crystal sensor with PVA/SiO₂ opal structure. *Applied Surface Science* **2017**, *423*, 421-425.
144. Zhang, Y.; Qiu, J.; Hu, R.; Li, P.; Gao, L.; Heng, L.; Tang, B. Z.; Jiang, L., A visual and organic vapor sensitive photonic crystal sensor consisting of polymer-infiltrated SiO₂ inverse opal. *Physical Chemistry Chemical Physics* **2015**, *17* (15), 9651-9658.
145. Zhang, Y.; Sun, Y.; Liu, J.; Guo, P.; Cai, Z.; Wang, J.-J., Polymer-infiltrated SiO₂ inverse opal photonic crystals for colorimetrically selective detection of xylene vapors. *Sensors and Actuators B: Chemical* **2019**, *291*, 67-73.
146. Liu, Y.; Salemink, H. W. M., Photonic crystal-based all-optical on-chip sensor. *Opt. Express* **2012**, *20* (18), 19912-19920.
147. Vigneswaran, D.; Ayyanar, N.; Sharma, M.; Sumathi, M.; M.S, M. R.; Porsezian, K., Salinity sensor using photonic crystal fiber. *Sensors and Actuators A: Physical* **2018**, *269*, 22-28.
148. Zlatanovic, S.; Mirkarimi, L. W.; Sigalas, M. M.; Bynum, M. A.; Chow, E.; Robotti, K. M.; Burr, G. W.; Esener, S.; Grot, A., Photonic crystal microcavity sensor for ultracompact monitoring of reaction kinetics and protein concentration. *Sensors and Actuators B: Chemical* **2009**, *141* (1), 13-19.
149. Scullion, M. G.; Di Falco, A.; Krauss, T. F., Slotted photonic crystal cavities with integrated microfluidics for biosensing applications. *Biosensors and Bioelectronics* **2011**, *27* (1), 101-105.
150. Pinto, A. M. R.; Lopez-Amo, M., Photonic Crystal Fibers for Sensing Applications. *Journal of Sensors* **2012**, *2012*, 598178.
151. De, M.; Gangopadhyay, T. K.; Singh, V. K., Prospects of Photonic Crystal Fiber as Physical Sensor: An Overview. *Sensors* **2019**, *19* (3).
152. Muscatello, M. M. W.; Asher, S. A., Poly(vinyl alcohol) Rehydratable Photonic Crystal Sensor Materials. *Advanced Functional Materials* **2008**, *18* (8), 1186-1193.
153. Lee, K.; Asher, S. A., Photonic Crystal Chemical Sensors: pH and Ionic Strength. *Journal of the American Chemical Society* **2000**, *122* (39), 9534-9537.
154. Sharma, A. C.; Jana, T.; Kesavamoorthy, R.; Shi, L.; Virji, M. A.; Finegold, D. N.; Asher, S. A., A general photonic crystal sensing motif: creatinine in bodily fluids. *Journal of the American Chemical Society* **2004**, *126* (9), 2971-2977.
155. Arunbabu, D.; Sannigrahi, A.; Jana, T., Photonic crystal hydrogel material for the sensing of toxic mercury ions (Hg²⁺) in water. *Soft Matter* **2011**, *7* (6), 2592-2599.
156. Cai, Z.; Kwak, D. H.; Punihaole, D.; Hong, Z.; Velankar, S. S.; Liu, X.; Asher, S. A., A Photonic Crystal Protein Hydrogel Sensor for *Candida albicans*. *Angewandte Chemie International Edition* **2015**, *54* (44), 13036-13040.
157. Walker, J. P.; Asher, S. A., Acetylcholinesterase-Based Organophosphate Nerve Agent Sensing Photonic Crystal. *Analytical Chemistry* **2005**, *77* (6), 1596-1600.
158. Alexeev, V. L.; Das, S.; Finegold, D. N.; Asher, S. A., Photonic Crystal Glucose-Sensing Material for Noninvasive Monitoring of Glucose in Tear Fluid. *Clinical Chemistry* **2004**, *50* (12), 2353-2360.
159. Holtz, J. H.; Asher, S. A., Polymerized colloidal crystal hydrogel films as intelligent chemical sensing materials. *Nature* **1997**, *389* (6653), 829-832.
160. Qin, J.; Dong, B.; Cao, L.; Wang, W., Photonic hydrogels for the ultratrace sensing of divalent beryllium in seawater. *Journal of Materials Chemistry C* **2018**, *6* (15), 4234-4242.
161. Alexeev, V. L.; Sharma, A. C.; Goponenko, A. V.; Das, S.; Lednev, I. K.; Wilcox, C. S.; Finegold, D. N.; Asher, S. A., High Ionic Strength Glucose-Sensing Photonic Crystal. *Analytical Chemistry* **2003**, *75* (10), 2316-2323.

162. Chen, C.; Dong, Z.-Q.; Shen, J.-H.; Chen, H.-W.; Zhu, Y.-H.; Zhu, Z.-G., 2D Photonic Crystal Hydrogel Sensor for Tear Glucose Monitoring. *ACS Omega* **2018**, *3* (3), 3211-3217.
163. Lan, Y.; Xue, M.; Qiu, L.; Meng, Z., Clinical Evaluation of a Photonic Crystal Sensor for Glucose Monitoring in Urine. *ChemistrySelect* **2019**, *4* (21), 6547-6551.
164. Chen, Q.; Wei, Z.; Wang, S.; Zhou, J.; Wu, Z., A self-healing smart photonic crystal hydrogel sensor for glucose and related saccharides. *Microchimica Acta* **2021**, *188* (6), 210.
165. Zeng, Y.; Wang, J.; Wang, Z.; Chen, G.; Yu, J.; Li, S.; Li, Q.; Li, H.; Wen, D.; Gu, Z.; Gu, Z., Colloidal crystal microneedle patch for glucose monitoring. *Nano Today* **2020**, *35*, 100984.
166. Zhang, P.-P.; Zhu, J.-C.; Zhao, B.-J.; Xu, S.-H.; Wang, L.; Luo, X.-L., Wearable transdermal microneedle patch based on photonic crystal hydrogel for glucose monitoring. *Chinese Journal of Analytical Chemistry* **2022**, *50* (4), 100054.
167. Chen, J.; Xu, L.; Yang, M.; Chen, X.; Chen, X.; Hong, W., Highly Stretchable Photonic Crystal Hydrogels for a Sensitive Mechanochromic Sensor and Direct Ink Writing. *Chemistry of Materials* **2019**, *31* (21), 8918-8926.
168. Li, Q.; Liu, S.; Wang, J.; Mondele Mbola, N.; Meng, Z.; Wang, X.; Xue, M., A biocompatible, self-adhesive, and stretchable photonic crystal sensor for underwater motion detection. *Journal of Materials Chemistry C* **2022**, *10* (23), 9025-9034.
169. Liu, R.; Cai, Z.; Zhang, Q.; Yuan, H.; Zhang, G.; Yang, D. a., Colorimetric two-dimensional photonic crystal biosensors for label-free detection of hydrogen peroxide. *Sensors and Actuators B: Chemical* **2022**, *354*, 131236.
170. Jia, X.; Zhang, T.; Wang, J.; Wang, K.; Tan, H.; Hu, Y.; Zhang, L.; Zhu, J., Responsive Photonic Hydrogel-Based Colorimetric Sensors for Detection of Aldehydes in Aqueous Solution. *Langmuir* **2018**, *34* (13), 3987-3992.
171. Tsuchiya, M.; Kurashina, Y.; Onoe, H., Eye-recognizable and repeatable biochemical flexible sensors using low angle-dependent photonic colloidal crystal hydrogel microbeads. *Scientific Reports* **2019**, *9* (1), 17059.
172. Shen, H.; Lin, Q.; Tang, H.; Tian, Y.; Zhang, X., Fabrication of Temperature- and Alcohol-Responsive Photonic Crystal Hydrogel and Its Application for Sustained Drug Release. *Langmuir* **2022**, *38* (12), 3785-3794.
173. Jia, X.; Xiao, T.; Hou, Z.; Xiao, L.; Qi, Y.; Hou, Z.; Zhu, J., Chemically Responsive Photonic Crystal Hydrogels for Selective and Visual Sensing of Thiol-Containing Biomolecules. *ACS Omega* **2019**, *4* (7), 12043-12048.
174. Jang, K.; Westbay, J. H.; Asher, S. A., DNA-Crosslinked 2D Photonic Crystal Hydrogels for Detection of Adenosine Actuated by an Adenosine-Binding Aptamer. *ACS Sensors* **2022**, *7* (6), 1648-1656.
175. Wang, Y.; Xie, T.; Yang, J.; Lei, M.; Fan, J.; Meng, Z.; Xue, M.; Qiu, L.; Qi, F.; Wang, Z., Fast screening of antibiotics in milk using a molecularly imprinted two-dimensional photonic crystal hydrogel sensor. *Analytica Chimica Acta* **2019**, *1070*, 97-103.
176. Murtaza, G.; Rizvi, A. S.; Irfan, M.; Yan, D.; Khan, R. U.; Rafique, B.; Xue, M.; Meng, Z. H.; Qu, F., Glycated albumin based photonic crystal sensors for detection of lipopolysaccharides and discrimination of Gram-negative bacteria. *Analytica Chimica Acta* **2020**, *1117*, 1-8.
177. Gao, Y.; Chen, Y.; Li, M.; Jia, L.; Zhang, L.; Zhu, J., Gelatin-based photonic hydrogels for visual detection of pathogenic *Pseudomonas aeruginosa*. *Sensors and Actuators B: Chemical* **2021**, *329*, 129137.
178. Wang, Y.; Zhang, D.; Zhang, H.; Shang, L.; Zhao, Y., Responsive photonic alginate hydrogel particles for the quantitative detection of alkaline phosphatase. *NPG Asia Materials* **2022**, *14* (1), 54.
179. Rizvi, A. S.; Murtaza, G.; Yan, D.; Irfan, M.; Xue, M.; Meng, Z. H.; Qu, F., Development of Molecularly Imprinted 2D Photonic Crystal Hydrogel Sensor for Detection of L-Kynurenine in Human Serum. *Talanta* **2020**, *208*, 120403.
180. Nishimura, S.; Abrams, N.; Lewis, B. A.; Halaoui, L. I.; Mallouk, T. E.; Benkstein, K. D.; van de Lagemaat, J.; Frank, A. J., Standing Wave Enhancement of Red Absorbance and Photocurrent in Dye-Sensitized Titanium Dioxide Photoelectrodes Coupled to Photonic Crystals. *Journal of the American Chemical Society* **2003**, *125* (20), 6306-6310.
181. Guo, S.; Albin, S., Simple plane wave implementation for photonic crystal calculations. *Opt. Express* **2003**, *11* (2), 167-175.

182. Lavrinenko, A.; Borel, P. I.; Frandsen, L. H.; Thorhauge, M.; Harpøth, A.; Kristensen, M.; Niemi, T.; Chong, H. M. H., Comprehensive FDTD modelling of photonic crystal waveguide components. *Opt. Express* **2004**, *12* (2), 234-248.
183. Sánchez, A.; Porta, A. V.; Orozco, S., Photonic band-gap and defect modes of a one-dimensional photonic crystal under localized compression. *Journal of Applied Physics* **2017**, *121* (17), 173101.
184. von Freymann, G.; Kitaev, V.; Lotsch, B. V.; Ozin, G. A., Bottom-up assembly of photonic crystals. *Chemical Society Reviews* **2013**, *42* (7), 2528-2554.
185. Likodimos, V., Photonic crystal-assisted visible light activated TiO₂ photocatalysis. *Applied Catalysis B: Environmental* **2018**, *230*, 269-303.
186. Chen, J. I. L.; von Freymann, G.; Choi, S. Y.; Kitaev, V.; Ozin, G. A., Slow photons in the fast lane in chemistry. *Journal of Materials Chemistry* **2008**, *18* (4), 369-373.
187. Mills, A.; Le Hunte, S., An overview of semiconductor photocatalysis. *Journal of Photochemistry and Photobiology A: Chemistry* **1997**, *108* (1), 1-35.
188. Ochiai, T.; Fujishima, A., Photoelectrochemical properties of TiO₂ photocatalyst and its applications for environmental purification. *Journal of Photochemistry and Photobiology C: Photochemistry Reviews* **2012**, *13* (4), 247-262.
189. Mo, J.; Zhang, Y.; Xu, Q.; Lamson, J. J.; Zhao, R., Photocatalytic purification of volatile organic compounds in indoor air: A literature review. *Atmospheric Environment* **2009**, *43* (14), 2229-2246.
190. Lee, S.-Y.; Park, S.-J., TiO₂ photocatalyst for water treatment applications. *Journal of Industrial and Engineering Chemistry* **2013**, *19* (6), 1761-1769.
191. Chong, M. N.; Jin, B.; Chow, C. W. K.; Saint, C., Recent developments in photocatalytic water treatment technology: A review. *Water Research* **2010**, *44* (10), 2997-3027.
192. Reddy, P. A. K.; Reddy, P. V. L.; Kwon, E.; Kim, K.-H.; Akter, T.; Kalagara, S., Recent advances in photocatalytic treatment of pollutants in aqueous media. *Environment International* **2016**, *91*, 94-103.
193. Lonnen, J.; Kilvington, S.; Kehoe, S. C.; Al-Touati, F.; McGuigan, K. G., Solar and photocatalytic disinfection of protozoan, fungal and bacterial microbes in drinking water. *Water Research* **2005**, *39* (5), 877-883.
194. Gamage, J.; Zhang, Z., Applications of Photocatalytic Disinfection. *International Journal of Photoenergy* **2010**, *2010*, 764870.
195. Wang, W.; Huang, G.; Yu, J. C.; Wong, P. K., Advances in photocatalytic disinfection of bacteria: Development of photocatalysts and mechanisms. *Journal of Environmental Sciences* **2015**, *34*, 232-247.
196. Li, J.; Wu, N., Semiconductor-based photocatalysts and photoelectrochemical cells for solar fuel generation: a review. *Catalysis Science & Technology* **2015**, *5* (3), 1360-1384.
197. Xiang, Q.; Cheng, B.; Yu, J., Graphene-Based Photocatalysts for Solar-Fuel Generation. *Angewandte Chemie International Edition* **2015**, *54* (39), 11350-11366.
198. Low, J.; Yu, J.; Ho, W., Graphene-Based Photocatalysts for CO₂ Reduction to Solar Fuel. *The Journal of Physical Chemistry Letters* **2015**, *6* (21), 4244-4251.
199. Liu, G.; Hoivik, N.; Wang, K.; Jakobsen, H., Engineering TiO₂ nanomaterials for CO₂ conversion/solar fuels. *Solar Energy Materials and Solar Cells* **2012**, *105*, 53-68.
200. Ge, M.; Li, Q.; Cao, C.; Huang, J.; Li, S.; Zhang, S.; Chen, Z.; Zhang, K.; Al-Deyab, S. S.; Lai, Y., One-dimensional TiO₂ Nanotube Photocatalysts for Solar Water Splitting. *Advanced Science* **2017**, *4* (1), 1600152.
201. Kumar, S. G.; Devi, L. G., Review on Modified TiO₂ Photocatalysis under UV/Visible Light: Selected Results and Related Mechanisms on Interfacial Charge Carrier Transfer Dynamics. *The Journal of Physical Chemistry A* **2011**, *115* (46), 13211-13241.
202. Banerjee, S.; Pillai, S. C.; Falaras, P.; O'Shea, K. E.; Byrne, J. A.; Dionysiou, D. D., New Insights into the Mechanism of Visible Light Photocatalysis. *The Journal of Physical Chemistry Letters* **2014**, *5* (15), 2543-2554.
203. Pelaez, M.; Nolan, N. T.; Pillai, S. C.; Seery, M. K.; Falaras, P.; Kontos, A. G.; Dunlop, P. S. M.; Hamilton, J. W. J.; Byrne, J. A.; O'Shea, K.; Entezari, M. H.; Dionysiou, D. D., A review on the visible light active titanium dioxide photocatalysts for environmental applications. *Applied Catalysis B: Environmental* **2012**, *125*, 331-349.

204. Han, F.; Kambala, V. S. R.; Srinivasan, M.; Rajarathnam, D.; Naidu, R., Tailored titanium dioxide photocatalysts for the degradation of organic dyes in wastewater treatment: A review. *Applied Catalysis A: General* **2009**, *359* (1), 25-40.
205. Chatterjee, D.; Dasgupta, S., Visible light induced photocatalytic degradation of organic pollutants. *Journal of Photochemistry and Photobiology C: Photochemistry Reviews* **2005**, *6* (2), 186-205.
206. Wang, H.; Zhang, L.; Chen, Z.; Hu, J.; Li, S.; Wang, Z.; Liu, J.; Wang, X., Semiconductor heterojunction photocatalysts: design, construction, and photocatalytic performances. *Chemical Society Reviews* **2014**, *43* (15), 5234-5244.
207. Wang, C.; Shao, C.; Zhang, X.; Liu, Y., SnO₂ Nanostructures-TiO₂ Nanofibers Heterostructures: Controlled Fabrication and High Photocatalytic Properties. *Inorganic Chemistry* **2009**, *48* (15), 7261-7268.
208. Zhou, W.; Liu, H.; Wang, J.; Liu, D.; Du, G.; Cui, J., Ag₂O/TiO₂ Nanobelts Heterostructure with Enhanced Ultraviolet and Visible Photocatalytic Activity. *ACS Applied Materials & Interfaces* **2010**, *2* (8), 2385-2392.
209. Bian, Z.; Tachikawa, T.; Zhang, P.; Fujitsuka, M.; Majima, T., Au/TiO₂ Superstructure-Based Plasmonic Photocatalysts Exhibiting Efficient Charge Separation and Unprecedented Activity. *Journal of the American Chemical Society* **2014**, *136* (1), 458-465.
210. Chai, B.; Peng, T.; Mao, J.; Li, K.; Zan, L., Graphitic carbon nitride (g-C₃N₄)-Pt-TiO₂ nanocomposite as an efficient photocatalyst for hydrogen production under visible light irradiation. *Physical Chemistry Chemical Physics* **2012**, *14* (48), 16745-16752.
211. Lu, Y.; Yu, H.; Chen, S.; Quan, X.; Zhao, H., Integrating Plasmonic Nanoparticles with TiO₂ Photonic Crystal for Enhancement of Visible-Light-Driven Photocatalysis. *Environmental Science & Technology* **2012**, *46* (3), 1724-1730.
212. Asahi, R.; Morikawa, T.; Ohwaki, T.; Aoki, K.; Taga, Y., Visible-Light Photocatalysis in Nitrogen-Doped Titanium Oxides. *Science* **2001**, *293* (5528), 269.
213. Ohno, T.; Akiyoshi, M.; Umebayashi, T.; Asai, K.; Mitsui, T.; Matsumura, M., Preparation of S-doped TiO₂ photocatalysts and their photocatalytic activities under visible light. *Applied Catalysis A: General* **2004**, *265* (1), 115-121.
214. Irie, H.; Watanabe, Y.; Hashimoto, K., Carbon-doped Anatase TiO₂ Powders as a Visible-light Sensitive Photocatalyst. *Chemistry Letters* **2003**, *32* (8), 772-773.
215. Li, R.; Li, T.; Zhou, Q., Impact of Titanium Dioxide (TiO₂) Modification on Its Application to Pollution Treatment—A Review. *Catalysts* **2020**, *10* (7).
216. Collins, G.; Lonergan, A.; McNulty, D.; Glynn, C.; Buckley, D.; Hu, C.; O'Dwyer, C., Semiconducting Metal Oxide Photonic Crystal Plasmonic Photocatalysts. *Advanced Materials Interfaces* **2020**, *7* (8), 1901805.
217. Fiorenza, R.; Bellardita, M.; Barakat, T.; Scirè, S.; Palmisano, L., Visible light photocatalytic activity of macro-mesoporous TiO₂-CeO₂ inverse opals. *Journal of Photochemistry and Photobiology A: Chemistry* **2018**, *352*, 25-34.
218. Chen, J. I. L.; Loso, E.; Ebrahim, N.; Ozin, G. A., Synergy of Slow Photon and Chemically Amplified Photochemistry in Platinum Nanocluster-Loaded Inverse Titania Opals. *Journal of the American Chemical Society* **2008**, *130* (16), 5420-5421.
219. Meng, S.; Li, D.; Fu, X.; Fu, X., Integrating photonic bandgaps with surface plasmon resonance for the enhancement of visible-light photocatalytic performance. *Journal of Materials Chemistry A* **2015**, *3* (46), 23501-23511.
220. Cai, J.; Wu, M.; Wang, Y.; Zhang, H.; Meng, M.; Tian, Y.; Li, X.; Zhang, J.; Zheng, L.; Gong, J., Synergetic Enhancement of Light Harvesting and Charge Separation over Surface-Disorder-Engineered TiO₂ Photonic Crystals. *Chem* **2017**, *2* (6), 877-892.
221. Chen, J. I. L.; von Freymann, G.; Choi, S. Y.; Kitaev, V.; Ozin, G. A., Amplified Photochemistry with Slow Photons. *Advanced Materials* **2006**, *18* (14), 1915-1919.
222. Zheng, X.; Meng, S.; Chen, J.; Wang, J.; Xian, J.; Shao, Y.; Fu, X.; Li, D., Titanium Dioxide Photonic Crystals with Enhanced Photocatalytic Activity: Matching Photonic Band Gaps of TiO₂ to the Absorption Peaks of Dyes. *The Journal of Physical Chemistry C* **2013**, *117* (41), 21263-21273.
223. Liu, J.; Jin, J.; Li, Y.; Huang, H.-W.; Wang, C.; Wu, M.; Chen, L.-H.; Su, B.-L., Tracing the slow photon effect in a ZnO inverse opal film for photocatalytic activity enhancement. *Journal of Materials Chemistry A* **2014**, *2* (14), 5051-5059.

224. Chen, S.-L.; Wang, A.-J.; Dai, C.; Benziger, J. B.; Liu, X.-C., The effect of photonic band gap on the photo-catalytic activity of nc-TiO₂/SnO₂ photonic crystal composite membranes. *Chemical Engineering Journal* **2014**, *249*, 48-53.
225. Geng, Z.; Zhang, Y.; Yuan, X.; Huo, M.; Zhao, Y.; Lu, Y.; Qiu, Y., Incorporation of Cu₂O nanocrystals into TiO₂ photonic crystal for enhanced UV–visible light driven photocatalysis. *Journal of Alloys and Compounds* **2015**, *644*, 734-741.
226. Guo, S.; Li, D.; Zhang, Y.; Zhang, Y.; Zhou, X., Fabrication of a Novel SnO₂ Photonic Crystal Sensitized by CdS Quantum Dots and Its Enhanced Photocatalysis under Visible Light Irradiation. *Electrochimica Acta* **2014**, *121*, 352-360.
227. Zheng, X.; Zhang, Z.; Meng, S.; Wang, Y.; Li, D., Regulating charge transfer over 3D Au/ZnO hybrid inverse opal toward efficiently photocatalytic degradation of bisphenol A and photoelectrochemical water splitting. *Chemical Engineering Journal* **2020**, *393*, 124676.
228. Raja-Mogan, T.; Lehoux, A.; Takashima, M.; Kowalska, E.; Ohtani, B., Slow Photon-induced Enhancement of Photocatalytic Activity of Gold Nanoparticle-incorporated Titania Inverse Opal. *Chemistry Letters* **2021**, *50* (4), 711-713.
229. Ye, J.; Xu, J.; Tian, D.; Zhao, X.; Wang, Q.; Wang, J.; Li, Y.; Zhao, C.; Liu, Z.; Fu, Y., Efficient photocatalytic reduction of CO₂ by a rhenium-doped TiO₂-x/SnO₂ inverse opal S-scheme heterostructure assisted by the slow-phonon effect. *Separation and Purification Technology* **2021**, *277*, 119431.
230. Jiao, J.; Wei, Y.; Zhao, Z.; Liu, J.; Li, J.; Duan, A.; Jiang, G., Photocatalysts of 3D Ordered Macroporous TiO₂-Supported CeO₂ Nanolayers: Design, Preparation, and Their Catalytic Performances for the Reduction of CO₂ with H₂O under Simulated Solar Irradiation. *Industrial & Engineering Chemistry Research* **2014**, *53* (44), 17345-17354.
231. Lei, J.; Chen, B.; Lv, W.; Zhou, L.; Wang, L.; Liu, Y.; Zhang, J., An inverse opal TiO₂/g-C₃N₄ composite with a heterojunction for enhanced visible light-driven photocatalytic activity. *Dalton Transactions* **2019**, *48* (10), 3486-3495.
232. Zhou, Q.; Song, Y.; Li, N.; Chen, D.; Xu, Q.; Li, H.; He, J.; Lu, J., Direct Dual Z-Scheme Bi₂WO₆/GQDs/WO₃ Inverse Opals for Enhanced Photocatalytic Activities under Visible Light. *ACS Sustainable Chemistry & Engineering* **2020**, *8* (21), 7921-7927.
233. Zulfiqar, A.; Temerov, F.; Saarinen, J. J., Multilayer TiO₂ Inverse Opal with Gold Nanoparticles for Enhanced Photocatalytic Activity. *ACS Omega* **2020**, *5* (20), 11595-11604.
234. Zhang, X.; John, S., Enhanced photocatalysis by light-trapping optimization in inverse opals. *Journal of Materials Chemistry A* **2020**, *8* (36), 18974-18986.
235. Chen, Y.; Li, L.; Xu, Q.; Chen, W.; Dong, Y.; Fan, J.; Ma, D., Recent Advances in Opal/Inverted Opal Photonic Crystal Photocatalysts. *Solar RRL* **2021**, *5* (6), 2000541.
236. Han, J. H.; Shneidman, A. V.; Kim, D. Y.; Nicolas, N. J.; van der Hoeven, J. E. S.; Aizenberg, M.; Aizenberg, J., Highly Ordered Inverse Opal Structures Synthesized from Shape-Controlled Nanocrystal Building Blocks. *Angewandte Chemie International Edition* **2022**, *61* (3), e202111048.
237. Fonash, S. J., Chapter 1 - Introduction. In *Solar Cell Device Physics (Second Edition)*, Fonash, S. J., Ed. Academic Press: Boston, 2010; pp 1-8.
238. Shah, A. V.; Platz, R.; Keppner, H., Thin-film silicon solar cells: A review and selected trends. *Solar Energy Materials and Solar Cells* **1995**, *38* (1), 501-520.
239. Wenham, S. R.; Green, M. A., Silicon solar cells. *Progress in Photovoltaics: Research and Applications* **1996**, *4* (1), 3-33.
240. Alsema, E. A.; Nieuwlaar, E., Energy viability of photovoltaic systems. *Energy Policy* **2000**, *28* (14), 999-1010.
241. Becker, C.; Amkreutz, D.; Sontheimer, T.; Preidel, V.; Lockau, D.; Haschke, J.; Jogschies, L.; Klimm, C.; Merkel, J. J.; Plocica, P.; Steffens, S.; Rech, B., Polycrystalline silicon thin-film solar cells: Status and perspectives. *Solar Energy Materials and Solar Cells* **2013**, *119*, 112-123.
242. Green, M. A., Thin-film solar cells: review of materials, technologies and commercial status. *Journal of Materials Science: Materials in Electronics* **2007**, *18* (1), 15-19.
243. Ameri, T.; Khoram, P.; Min, J.; Brabec, C. J., Organic Ternary Solar Cells: A Review. *Advanced Materials* **2013**, *25* (31), 4245-4266.

244. Petrus, M. L.; Schlipf, J.; Li, C.; Gujar, T. P.; Giesbrecht, N.; Müller-Buschbaum, P.; Thelakkat, M.; Bein, T.; Hüttner, S.; Docampo, P., Capturing the Sun: A Review of the Challenges and Perspectives of Perovskite Solar Cells. *Advanced Energy Materials* **2017**, *7* (16), 1700264.
245. Gong, J.; Sumathy, K.; Qiao, Q.; Zhou, Z., Review on dye-sensitized solar cells (DSSCs): Advanced techniques and research trends. *Renewable and Sustainable Energy Reviews* **2017**, *68*, 234-246.
246. Ragoussi, M.-E.; Torres, T., New generation solar cells: concepts, trends and perspectives. *Chemical Communications* **2015**, *51* (19), 3957-3972.
247. Uddin, A.; Upama, M. B.; Yi, H.; Duan, L., Encapsulation of Organic and Perovskite Solar Cells: A Review. *Coatings* **2019**, *9* (2).
248. Milichko, V. A.; Shalin, A. S.; Mukhin, I. S.; Kovrov, A. E.; Krasilin, A. A.; Vinogradov, A. V.; Belov, P. A.; Simovski, C. R., Solar photovoltaics: current state and trends. *Physics-Uspekhi* **2016**, *59* (8), 727-772.
249. Pattnaik, S.; Chakravarty, N.; Biswas, R.; Dalal, V.; Slafer, D., Nano-phonic and nano-plasmonic enhancements in thin film silicon solar cells. *Solar Energy Materials and Solar Cells* **2014**, *129*, 115-123.
250. Wu, Y.; Zhu, W., Organic sensitizers from D- π -A to D-A- π -A: effect of the internal electron-withdrawing units on molecular absorption, energy levels and photovoltaic performances. *Chemical Society Reviews* **2013**, *42* (5), 2039-2058.
251. Shah, A. V.; Schade, H.; Vanecek, M.; Meier, J.; Vallat-Sauvain, E.; Wyrsh, N.; Kroll, U.; Droz, C.; Bailat, J., Thin-film silicon solar cell technology. *Progress in Photovoltaics: Research and Applications* **2004**, *12* (2-3), 113-142.
252. Lee, T. D.; Ebong, A. U., A review of thin film solar cell technologies and challenges. *Renewable and Sustainable Energy Reviews* **2017**, *70*, 1286-1297.
253. Shah, A.; Torres, P.; Tscharnner, R.; Wyrsh, N.; Keppner, H., Photovoltaic Technology: The Case for Thin-Film Solar Cells. *Science* **1999**, *285* (5428), 692.
254. Schropp, R. E. I.; Carius, R.; Beaucarne, G., Amorphous Silicon, Microcrystalline Silicon, and Thin-Film Polycrystalline Silicon Solar Cells. *MRS Bulletin* **2007**, *32* (3), 219-224.
255. Keppner, H.; Meier, J.; Torres, P.; Fischer, D.; Shah, A., Microcrystalline silicon and micromorph tandem solar cells. *Applied Physics A* **1999**, *69* (2), 169-177.
256. Müller, J.; Rech, B.; Springer, J.; Vanecek, M., TCO and light trapping in silicon thin film solar cells. *Solar Energy* **2004**, *77* (6), 917-930.
257. Dewan, R.; Marinkovic, M.; Noriega, R.; Phadke, S.; Salleo, A.; Knipp, D., Light trapping in thin-film silicon solar cells with submicron surface texture. *Opt. Express* **2009**, *17* (25), 23058-23065.
258. Baker-Finch, S. C.; McIntosh, K. R., Reflection of normally incident light from silicon solar cells with pyramidal texture. *Progress in Photovoltaics: Research and Applications* **2011**, *19* (4), 406-416.
259. Moulin, E.; Paetzold, U. W.; Siekmann, H.; Worbs, J.; Bauer, A.; Carius, R., Study of thin-film silicon solar cell back reflectors and potential of detached reflectors. *Energy Procedia* **2011**, *10*, 106-110.
260. Yang, Y.; O'Brien, P. G.; Ozin, G. A.; Kherani, N. P., See-through amorphous silicon solar cells with selectively transparent and conducting photonic crystal back reflectors for building integrated photovoltaics. *Applied Physics Letters* **2013**, *103* (22), 221109.
261. Soman, A.; Antony, A., Colored solar cells with spectrally selective photonic crystal reflectors for application in building integrated photovoltaics. *Solar Energy* **2019**, *181*, 1-8.
262. Varghese, L. T.; Xuan, Y.; Niu, B.; Fan, L.; Bermel, P.; Qi, M., Enhanced Photon Management of Thin-Film Silicon Solar Cells Using Inverse Opal Photonic Crystals with 3D Photonic Bandgaps. *Advanced Optical Materials* **2013**, *1* (10), 692-698.
263. Bielawny, A.; Üpping, J.; Miclea, P. T.; Wehrspohn, R. B.; Rockstuhl, C.; Lederer, F.; Peters, M.; Steidl, L.; Zentel, R.; Lee, S.-M.; Knez, M.; Lambert, A.; Carius, R., 3D photonic crystal intermediate reflector for micromorph thin-film tandem solar cell. *physica status solidi (a)* **2008**, *205* (12), 2796-2810.
264. Üpping, J.; Bielawny, A.; Wehrspohn, R. B.; Beckers, T.; Carius, R.; Rau, U.; Fahr, S.; Rockstuhl, C.; Lederer, F.; Kroll, M.; Pertsch, T.; Steidl, L.; Zentel, R., Three-Dimensional Photonic Crystal Intermediate Reflectors for Enhanced Light-Trapping in Tandem Solar Cells. *Advanced Materials* **2011**, *23* (34), 3896-3900.
265. Jung, H. S.; Lee, J.-K., Dye Sensitized Solar Cells for Economically Viable Photovoltaic Systems. *The Journal of Physical Chemistry Letters* **2013**, *4* (10), 1682-1693.

266. Shalini, S.; Balasundara prabhu, R.; Prasanna, S.; Mallick, T. K.; Senthilarasu, S., Review on natural dye sensitized solar cells: Operation, materials and methods. *Renewable and Sustainable Energy Reviews* **2015**, *51*, 1306-1325.
267. Shalini, S.; Balasundaraprabhu, R.; Kumar, T. S.; Prabavathy, N.; Senthilarasu, S.; Prasanna, S., Status and outlook of sensitizers/dyes used in dye sensitized solar cells (DSSC): a review. *International Journal of Energy Research* **2016**, *40* (10), 1303-1320.
268. Richhariya, G.; Kumar, A.; Tekasakul, P.; Gupta, B., Natural dyes for dye sensitized solar cell: A review. *Renewable and Sustainable Energy Reviews* **2017**, *69*, 705-718.
269. Sugathan, V.; John, E.; Sudhakar, K., Recent improvements in dye sensitized solar cells: A review. *Renewable and Sustainable Energy Reviews* **2015**, *52*, 54-64.
270. Shakeel Ahmad, M.; Pandey, A. K.; Abd Rahim, N., Advancements in the development of TiO₂ photoanodes and its fabrication methods for dye sensitized solar cell (DSSC) applications. A review. *Renewable and Sustainable Energy Reviews* **2017**, *77*, 89-108.
271. Colodrero, S.; Mihi, A.; Häggman, L.; Ocaña, M.; Boschloo, G.; Hagfeldt, A.; Míguez, H., Porous One-Dimensional Photonic Crystals Improve the Power-Conversion Efficiency of Dye-Sensitized Solar Cells. *Advanced Materials* **2009**, *21* (7), 764-770.
272. Guo, M.; Xie, K.; Lin, J.; Yong, Z.; Yip, C. T.; Zhou, L.; Wang, Y.; Huang, H., Design and coupling of multifunctional TiO₂ nanotube photonic crystal to nanocrystalline titania layer as semi-transparent photoanode for dye-sensitized solar cell. *Energy & Environmental Science* **2012**, *5* (12), 9881-9888.
273. Mihi, A.; Zhang, C.; Braun, P. V., Transfer of Preformed Three-Dimensional Photonic Crystals onto Dye-Sensitized Solar Cells. *Angewandte Chemie International Edition* **2011**, *50* (25), 5712-5715.
274. Liu, L.; Karuturi, S. K.; Su, L. T.; Tok, A. I. Y., TiO₂ inverse-opal electrode fabricated by atomic layer deposition for dye-sensitized solar cell applications. *Energy & Environmental Science* **2011**, *4* (1), 209-215.
275. Guldin, S.; Hüttner, S.; Kolle, M.; Welland, M. E.; Müller-Buschbaum, P.; Friend, R. H.; Steiner, U.; Tétreault, N., Dye-Sensitized Solar Cell Based on a Three-Dimensional Photonic Crystal. *Nano Letters* **2010**, *10* (7), 2303-2309.
276. Mihi, A.; Calvo, M. E.; Anta, J. A.; Míguez, H., Spectral Response of Opal-Based Dye-Sensitized Solar Cells. *The Journal of Physical Chemistry C* **2008**, *112* (1), 13-17.
277. Mihi, A.; López-Alcaraz, F. J.; Míguez, H., Full spectrum enhancement of the light harvesting efficiency of dye sensitized solar cells by including colloidal photonic crystal multilayers. *Applied Physics Letters* **2006**, *88* (19), 193110.
278. Suezaki, T.; Yano, H.; Hatayama, T.; Ozin, G. A.; Fuyuki, T., Photoconductivity in inverse silicon opals enhanced by slow photon effect: Yet another step towards optically amplified silicon photonic crystal solar cells. *Applied Physics Letters* **2011**, *98* (7), 072106.
279. Beydoun, N.; Farhat, R.; Halaoui, L. I., Enhanced Solar Light Harvesting with Q-CdTe/Se Sensitized Inverse Opal TiO₂. *ACS Applied Energy Materials* **2020**, *3* (3), 3104-3119.
280. Chen, X.; Ye, J.; Ouyang, S.; Kako, T.; Li, Z.; Zou, Z., Enhanced Incident Photon-to-Electron Conversion Efficiency of Tungsten Trioxide Photoanodes Based on 3D-Photonic Crystal Design. *ACS Nano* **2011**, *5* (6), 4310-4318.
281. Bayram, S.; Halaoui, L., Amplification of Solar Energy Conversion in Quantum-Confined CdSe-Sensitized TiO₂ Photonic Crystals by Trapping Light. *Particle & Particle Systems Characterization* **2013**, *30* (8), 706-714.
282. Delgado-Sanchez, J. M.; Lillo-Bravo, I., Angular Dependence of Photonic Crystal Coupled to Photovoltaic Solar Cell. *Applied Sciences* **2020**, *10* (5).
283. Ke, X.; Yang, M.; Wang, W.; Luo, D.; Zhang, M., Incidence Dependency of Photonic Crystal Substrate and Its Application on Solar Energy Conversion: Ag₂S Sensitized WO₃ in FTO Photonic Crystal Film. *Materials* **2019**, *12* (16).
284. Wang, K.; Ke, X.; Wang, W.; Tu, C.; Luo, D.; Zhang, M., The Impacts of Fluorine-Doped Tin Oxide Photonic Crystals on a Cadmium Sulfide-Based Photoelectrode for Improved Solar Energy Conversion under Lower Incidence. *Catalysts* **2020**, *10* (11).
285. Zhang, W.; Anaya, M.; Lozano, G.; Calvo, M. E.; Johnston, M. B.; Míguez, H.; Snaith, H. J., Highly Efficient Perovskite Solar Cells with Tunable Structural Color. *Nano Letters* **2015**, *15* (3), 1698-1702.

286. Jo, S.; Woo, J. Y.; Oh, J. H.; Shim, H. C.; Seo, S.; Jeon, E.-S.; Kim, M.; Han, C.-S., Angle-Insensitive Transmission and Reflection of Nanopatterned Dielectric Multilayer Films for Colorful Solar Cells. *ACS Applied Materials & Interfaces* **2020**, *12* (26), 29979-29985.
287. Liu, Z.; Wu, L.; Wang, X.; Xu, Q.; Hu, Y.; Meng, K.; Chen, G., Improving efficiency and stability of colorful perovskite solar cells with two-dimensional photonic crystals. *Nanoscale* **2020**, *12* (15), 8425-8431.
288. Golabi, P.; Keshavarzi, R.; Mirkhani, V.; Moghadam, M.; Tangestaninejad, S.; Mohammadpoor-Baltork, I.; Abrams, N. M., Efficient colorful perovskite solar cells designed by 2D and 3D ordered titania inverse opals. *Journal of Power Sources* **2021**, *512*, 230488.
289. Ke, Y.; Balin, I.; Wang, N.; Lu, Q.; Tok, A. I. Y.; White, T. J.; Magdassi, S.; Abdulhalim, I.; Long, Y., Two-Dimensional SiO₂/VO₂ Photonic Crystals with Statically Visible and Dynamically Infrared Modulated for Smart Window Deployment. *ACS Applied Materials & Interfaces* **2016**, *8* (48), 33112-33120.
290. Zaky, Z. A.; Aly, A. H., Novel smart window using photonic crystal for energy saving. *Scientific Reports* **2022**, *12* (1), 10104.
291. Snyder, A. W.; Love, J. D., Chapter 1 - Bound rays of planar waveguides. In *Optical Waveguide Theory*, Snyder, A. W.; Love, J. D., Eds. Springer US: Boston, MA, 1983; pp 6-25.
292. El Abdi, R.; Rujinski, A. D.; Poulain, M., Effects of immersion duration and temperature on mechanical properties of optical fibers aged in CTAC aqueous solution. *Engineering Science and Technology, an International Journal* **2015**, *18* (1), 52-58.
293. Yun, S. H.; Tearney, G. J.; Vakoc, B. J.; Shishkov, M.; Oh, W. Y.; Desjardins, A. E.; Suter, M. J.; Chan, R. C.; Evans, J. A.; Jang, I.-K.; Nishioka, N. S.; de Boer, J. F.; Bouma, B. E., Comprehensive volumetric optical microscopy in vivo. *Nature Medicine* **2006**, *12* (12), 1429-1433.
294. Gerd, K.; Fei, X.; Ying, C.; Perry Ping, S., Review of diverse optical fibers used in biomedical research and clinical practice. *Journal of Biomedical Optics* **2014**, *19* (8), 1-29.
295. Addanki, S.; Amiri, I. S.; Yupapin, P., Review of optical fibers-introduction and applications in fiber lasers. *Results in Physics* **2018**, *10*, 743-750.
296. Dragic, P. D.; Cavillon, M.; Ballato, J., Materials for optical fiber lasers: A review. *Applied Physics Reviews* **2018**, *5* (4), 041301.
297. Ballato, J.; Dragic, P., Glass: The Carrier of Light - A Brief History of Optical Fiber. *International Journal of Applied Glass Science* **2016**, *7* (4), 413-422.
298. Yu, F.; Cann, M.; Brunton, A.; Wadsworth, W.; Knight, J., Single-mode solarization-free hollow-core fiber for ultraviolet pulse delivery. *Opt. Express* **2018**, *26* (8), 10879-10887.
299. Knight, J. C.; Russell, P. S. J., New Ways to Guide Light. *Science* **2002**, *296* (5566), 276.
300. Knight, J. C., Photonic crystal fibres. *Nature* **2003**, *424* (6950), 847-851.
301. Knight, J. C.; Birks, T. A.; Russell, P. S. J.; Atkin, D. M., All-silica single-mode optical fiber with photonic crystal cladding. *Opt. Lett.* **1996**, *21* (19), 1547-1549.
302. Russell, P., Photonic Crystal Fibers. *Science* **2003**, *299* (5605), 358.
303. Chugh, S.; Gulistan, A.; Ghosh, S.; Rahman, B. M. A., Machine learning approach for computing optical properties of a photonic crystal fiber. *Opt. Express* **2019**, *27* (25), 36414-36425.
304. Haakestad, M. W.; Engan, H. E., Acoustooptic properties of a weakly multimode solid core photonic crystal fiber. *Journal of Lightwave Technology* **2006**, *24* (2), 838-845.
305. Ranka, J. K.; Windeler, R. S.; Stentz, A. J., Visible continuum generation in air-silica microstructure optical fibers with anomalous dispersion at 800 nm. *Opt. Lett.* **2000**, *25* (1), 25-27.
306. Reeves, W. H.; Knight, J. C.; Russell, P. S. J.; Roberts, P. J., Demonstration of ultra-flattened dispersion in photonic crystal fibers. *Opt. Express* **2002**, *10* (14), 609-613.
307. Ortigosa-Blanch, A.; Knight, J. C.; Wadsworth, W. J.; Arriaga, J.; Mangan, B. J.; Birks, T. A.; Russell, P. S. J., Highly birefringent photonic crystal fibers. *Opt. Lett.* **2000**, *25* (18), 1325-1327.
308. Knight, J. C.; Birks, T. A.; Cregan, R. F.; Russell, P. S. J.; Sandro, J.-P. d., Large mode area photonic crystal fibre. *Electronics Letters* **1998**, *34* (13), 1347-1348.
309. Broderick, N. G. R.; Offerhaus, H. L.; Richardson, D. J.; Sammut, R. A.; Caplen, J.; Dong, L., Large Mode Area Fibers for High Power Applications. *Optical Fiber Technology* **1999**, *5* (2), 185-196.
310. Demir, H.; Ozsoy, S., Comparative study of large-solid-core photonic crystal fibers: Dispersion and effective mode area. *Optik* **2012**, *123* (8), 739-743.

311. Humbert, G.; Wadsworth, W. J.; Leon-Saval, S. G.; Knight, J. C.; Birks, T. A.; Russell, P. S. J.; Lederer, M. J.; Kopf, D.; Wiesauer, K.; Breuer, E. I.; Stifter, D., Supercontinuum generation system for optical coherence tomography based on tapered photonic crystal fibre. *Opt. Express* **2006**, *14* (4), 1596-1603.
312. Omenetto, F. G.; Wolchover, N. A.; Wehner, M. R.; Ross, M.; Efimov, A.; Taylor, A. J.; Kumar, V. V. R. K.; George, A. K.; Knight, J. C.; Joly, N. Y.; Russell, P. S. J., Spectrally smooth supercontinuum from 350 nm to 3 μ m in sub-centimeter lengths of soft-glass photonic crystal fibers. *Opt. Express* **2006**, *14* (11), 4928-4934.
313. Udem, T.; Holzwarth, R.; Hänsch, T. W., Optical frequency metrology. *Nature* **2002**, *416* (6877), 233-237.
314. Cregan, R. F.; Mangan, B. J.; Knight, J. C.; Birks, T. A.; Russell, P. S. J.; Roberts, P. J.; Allan, D. C., Single-Mode Photonic Band Gap Guidance of Light in Air. *Science* **1999**, *285* (5433), 1537.
315. Mangan, B. J.; Farr, L.; Langford, A.; Roberts, P. J.; Williams, D. P.; Couny, F.; Lawman, M.; Mason, M.; Coupland, S.; Flea, R.; Sabert, H.; Birks, T. A.; Knight, J. C.; Russell, P. S. J. In *Low loss (1.7 dB/km) hollow core photonic bandgap fiber*, Optical Fiber Communication Conference, 2004. OFC 2004, 23-27 Feb. 2004; 2004; p 3 pp. vol.2.
316. Roberts, P. J.; Couny, F.; Sabert, H.; Mangan, B. J.; Williams, D. P.; Farr, L.; Mason, M. W.; Tomlinson, A.; Birks, T. A.; Knight, J. C.; Russell, P. S. J., Ultimate low loss of hollow-core photonic crystal fibres. *Opt. Express* **2005**, *13* (1), 236-244.
317. Shephard, J. D.; Jones, J. D. C.; Hand, D. P.; Bouwmans, G.; Knight, J. C.; Russell, P. S. J.; Mangan, B. J., High energy nanosecond laser pulses delivered single-mode through hollow-core PBG fibers. *Opt. Express* **2004**, *12* (4), 717-723.
318. Shephard, J. D.; MacPherson, W. N.; Maier, R. R. J.; Jones, J. D. C.; Hand, D. P.; Mohebbi, M.; George, A. K.; Roberts, P. J.; Knight, J. C., Single-mode mid-IR guidance in a hollow-core photonic crystal fiber. *Opt. Express* **2005**, *13* (18), 7139-7144.
319. Hensley, C. J.; Ouzounov, D. G.; Gaeta, A. L.; Venkataraman, N.; Gallagher, M. T.; Koch, K. W., Silica-glass contribution to the effective nonlinearity of hollow-core photonic band-gap fibers. *Opt. Express* **2007**, *15* (6), 3507-3512.
320. Knight, J. C.; G er me, F.; Wadsworth, W. J., Hollow-core photonic crystal fibres for delivery and compression of ultrashort optical pulses. *Optical and Quantum Electronics* **2007**, *39* (12), 1047-1056.
321. Michieletto, M.; Lyngs , J. K.; Jakobsen, C.; Lægsgaard, J.; Bang, O.; Alkeskjold, T. T., Hollow-core fibers for high power pulse delivery. *Opt. Express* **2016**, *24* (7), 7103-7119.
322. Liu, X.; Du, D.; Mourou, G., Laser ablation and micromachining with ultrashort laser pulses. *IEEE Journal of Quantum Electronics* **1997**, *33* (10), 1706-1716.
323. Svanberg, S., Some applications of ultrashort laser pulses in biology and medicine. *Measurement Science and Technology* **2001**, *12* (11), 1777-1783.
324. Kim, B. M.; Feit, M. D.; Rubenchik, A. M.; Mammini, B. M.; Da Silva, L. B., Optical feedback signal for ultrashort laser pulse ablation of tissue Work performed at Lawrence Livermore National Laboratory under the auspices of the US Department of Energy under contract No. W-7405-ENG-48.1. *Applied Surface Science* **1998**, *127-129*, 857-862.
325. Yu, F.; Knight, J. C., Negative Curvature Hollow-Core Optical Fiber. *IEEE Journal of Selected Topics in Quantum Electronics* **2016**, *22* (2), 146-155.
326. Jason, M. K.; Nahum, G.; Bruce, E. B.; Rebecca, L. E.; Bret, D. C.; Tanya, L. M.; Carlos, M. B.; James, A. H. In *Hollow core fiber optics for mid-wave and long-wave infrared spectroscopy*, Proc.SPIE, 2011.
327. Dudley, J. M.; Taylor, J. R., Ten years of nonlinear optics in photonic crystal fibre. *Nature Photonics* **2009**, *3* (2), 85-90.
328. Travers, J. C.; Chang, W.; Nold, J.; Joly, N. Y.; St. J. Russell, P., Ultrafast nonlinear optics in gas-filled hollow-core photonic crystal fibers [Invited]. *J. Opt. Soc. Am. B* **2011**, *28* (12), A11-A26.
329. Joly, N. Y.; Nold, J.; Chang, W.; H lzer, P.; Nazarkin, A.; Wong, G. K. L.; Biancalana, F.; Russell, P. S. J., Bright Spatially Coherent Wavelength-Tunable Deep-UV Laser Source Using an Ar-Filled Photonic Crystal Fiber. *Physical Review Letters* **2011**, *106* (20), 203901.
330. Mak, K. F.; Travers, J. C.; H lzer, P.; Joly, N. Y.; Russell, P. S. J., Tunable vacuum-UV to visible ultrafast pulse source based on gas-filled Kagome-PCF. *Opt. Express* **2013**, *21* (9), 10942-10953.

331. Benabid, F.; Bouwmans, G.; Knight, J. C.; Russell, P. S. J.; Couny, F., Ultrahigh Efficiency Laser Wavelength Conversion in a Gas-Filled Hollow Core Photonic Crystal Fiber by Pure Stimulated Rotational Raman Scattering in Molecular Hydrogen. *Physical Review Letters* **2004**, *93* (12), 123903.
332. Benabid, F., Hollow-core photonic bandgap fibre: new light guidance for new science and technology. *Philosophical Transactions of the Royal Society A: Mathematical, Physical and Engineering Sciences* **2006**, *364* (1849), 3439-3462.
333. Monat, C.; de Sterke, M.; Eggleton, B. J., Slow light enhanced nonlinear optics in periodic structures. *Journal of Optics* **2010**, *12* (10), 104003.
334. Monat, C.; Corcoran, B.; Ebnali-Heidari, M.; Grillet, C.; Eggleton, B. J.; White, T. P.; O'Faolain, L.; Krauss, T. F., Slow light enhancement of nonlinear effects in silicon engineered photonic crystal waveguides. *Opt. Express* **2009**, *17* (4), 2944-2953.
335. Hamachi, Y.; Kubo, S.; Baba, T., Slow light with low dispersion and nonlinear enhancement in a lattice-shifted photonic crystal waveguide. *Opt. Lett.* **2009**, *34* (7), 1072-1074.
336. Sardar, M. R.; Faisal, M.; Ahmed, K., Design and characterization of rectangular slotted porous core photonic crystal fiber for sensing CO₂ gas. *Sensing and Bio-Sensing Research* **2020**, *30*, 100379.
337. Sardar, M. R.; Faisal, M.; Ahmed, K., Hybrid porous core photonic crystal fiber sensor for monitoring nitrous oxide gas. *Sensing and Bio-Sensing Research* **2020**, *30*, 100389.
338. Mishra, G. P.; Kumar, D.; Chaudhary, V. S.; Kumar, S., Design and Sensitivity Improvement of Microstructured-Core Photonic Crystal Fiber Based Sensor for Methane and Hydrogen Fluoride Detection. *IEEE Sensors Journal* **2022**, *22* (2), 1265-1272.
339. Kabir Yakasai, I.; Abas, P. E.; Begum, F., Proposal of novel photonic crystal fibre for sensing adulterated petrol and diesel with kerosene in terahertz frequencies. *IET Optoelectronics* **2020**, *14* (5), 319-326.
340. Rahman, A.; Khaleque, A.; Ali, M. Y.; Rahman, M. T., THz spectroscopic sensing of liquid chemicals using a photonic crystal fiber. *OSA Continuum* **2020**, *3* (11), 2982-2996.
341. Natesan, A.; Govindasamy, K. P.; Gopal, T. R.; Dhasarathan, V.; Aly, A. H., Tricore photonic crystal fibre based refractive index sensor for glucose detection. *IET Optoelectronics* **2019**, *13* (3), 118-123.
342. Rahman, M. M.; Mou, F. A.; Bhuiyan, M. I. H.; Islam, M. R., Photonic crystal fiber based terahertz sensor for cholesterol detection in human blood and liquid foodstuffs. *Sensing and Bio-Sensing Research* **2020**, *29*, 100356.
343. Ayyanar, N.; Raja, G. T.; Sharma, M.; Kumar, D. S., Photonic Crystal Fiber-Based Refractive Index Sensor for Early Detection of Cancer. *IEEE Sensors Journal* **2018**, *18* (17), 7093-7099.
344. Jabin, M. A.; Luo, Y.; Peng, G.-D.; Rana, M. J.; Ahmed, K.; Nguyen, T. K.; Paul, B. K.; Dhasarathan, V., Design and fabrication of amoeba faced photonic crystal fiber for biosensing application. *Sensors and Actuators A: Physical* **2020**, *313*, 112204.
345. Eid, M. M. A.; Rashed, A. N. Z.; Bulbul, A. A.-M.; Podder, E., Mono-Rectangular Core Photonic Crystal Fiber (MRC-PCF) for Skin and Blood Cancer Detection. *Plasmonics* **2021**, *16* (3), 717-727.
346. Hassani, A.; Skorobogatiy, M., Design of the Microstructured Optical Fiber-based Surface Plasmon Resonance sensors with enhanced microfluidics. *Opt. Express* **2006**, *14* (24), 11616-11621.
347. Chen, X.; Xia, L.; Li, C., Surface Plasmon Resonance Sensor Based on a Novel D-Shaped Photonic Crystal Fiber for Low Refractive Index Detection. *IEEE Photonics Journal* **2018**, *10* (1), 1-9.
348. Yasli, A.; Ademgil, H.; Haxha, S.; Aggoun, A., Multi-Channel Photonic Crystal Fiber Based Surface Plasmon Resonance Sensor for Multi-Analyte Sensing. *IEEE Photonics Journal* **2020**, *12* (1), 1-15.
349. Islam, M. S.; Cordeiro, C. M. B.; Nine, M. J.; Sultana, J.; Cruz, A. L. S.; Dinovitser, A.; Ng, B. W. H.; Ebendorff-Heidepriem, H.; Losic, D.; Abbott, D., Experimental Study on Glass and Polymers: Determining the Optimal Material for Potential Use in Terahertz Technology. *IEEE Access* **2020**, *8*, 97204-97214.
350. Abdullah-Al-Shafi, M.; Akter, N.; Sen, S.; Hossain, M. S., Design and performance analysis of background material of zeonex based high core power fraction and extremely low effective material loss of photonic crystal fiber in the terahertz (THz) wave pulse for many types of communication areas. *Optik* **2021**, *243*, 167519.
351. Dash, J. N.; Jha, R., Graphene-Based Birefringent Photonic Crystal Fiber Sensor Using Surface Plasmon Resonance. *IEEE Photonics Technology Letters* **2014**, *26* (11), 1092-1095.

352. Dash, J. N.; Jha, R., On the Performance of Graphene-Based D-Shaped Photonic Crystal Fibre Biosensor Using Surface Plasmon Resonance. *Plasmonics* **2015**, *10* (5), 1123-1131.
353. Yang, X.; Lu, Y.; Liu, B.; Yao, J., Analysis of Graphene-Based Photonic Crystal Fiber Sensor Using Birefringence and Surface Plasmon Resonance. *Plasmonics* **2017**, *12* (2), 489-496.
354. Yan, H.; Sokolov, S.; Lytle, J. C.; Stein, A.; Zhang, F.; Smyrl, W. H., Colloidal-Crystal-Templated Synthesis of Ordered Macroporous Electrode Materials for Lithium Secondary Batteries. *Journal of The Electrochemical Society* **2003**, *150* (8), A1102.
355. Zhang, J.; Jin, Y.; Li, C.; Shen, Y.; Han, L.; Hu, Z.; Di, X.; Liu, Z., Creation of three-dimensionally ordered macroporous Au/CeO₂ catalysts with controlled pore sizes and their enhanced catalytic performance for formaldehyde oxidation. *Applied Catalysis B: Environmental* **2009**, *91* (1), 11-20.
356. Stein, A.; Wilson, B. E.; Rudisill, S. G., Design and functionality of colloidal-crystal-templated materials—chemical applications of inverse opals. *Chemical Society Reviews* **2013**, *42* (7), 2763-2803.
357. Hoa, M. L. K.; Lu, M.; Zhang, Y., Preparation of porous materials with ordered hole structure. *Advances in Colloid and Interface Science* **2006**, *121* (1), 9-23.
358. Hollister, S. J., Porous scaffold design for tissue engineering. *Nature Materials* **2005**, *4* (7), 518-524.
359. Hutmacher, D. W., Scaffold design and fabrication technologies for engineering tissues — state of the art and future perspectives. *Journal of Biomaterials Science, Polymer Edition* **2001**, *12* (1), 107-124.
360. Choi, S.-W.; Zhang, Y.; Xia, Y., Three-Dimensional Scaffolds for Tissue Engineering: The Importance of Uniformity in Pore Size and Structure. *Langmuir* **2010**, *26* (24), 19001-19006.
361. Zhang, Y. S.; Regan, K. P.; Xia, Y., Controlling the Pore Sizes and Related Properties of Inverse Opal Scaffolds for Tissue Engineering Applications. *Macromolecular Rapid Communications* **2013**, *34* (6), 485-491.
362. Zhu, C.; Qiu, J.; Pongkitwitoon, S.; Thomopoulos, S.; Xia, Y., Inverse Opal Scaffolds with Gradations in Mineral Content for Spatial Control of Osteogenesis. *Advanced Materials* **2018**, *30* (29), 1706706.
363. Ma, P. X., Scaffolds for tissue fabrication. *Materials Today* **2004**, *7* (5), 30-40.
364. Choi, S.-W.; Xie, J.; Xia, Y., Chitosan-Based Inverse Opals: Three-Dimensional Scaffolds with Uniform Pore Structures for Cell Culture. *Advanced Materials* **2009**, *21* (29), 2997-3001.
365. Sommer, M. R.; Vetsch, J. R.; Leemann, J.; Müller, R.; Studart, A. R.; Hofmann, S., Silk fibroin scaffolds with inverse opal structure for bone tissue engineering. *Journal of Biomedical Materials Research Part B: Applied Biomaterials* **2017**, *105* (7), 2074-2084.
366. Wang, L.; Sun, L.; Bian, F.; Wang, Y.; Zhao, Y., Self-Bonded Hydrogel Inverse Opal Particles as Sprayed Flexible Patch for Wound Healing. *ACS Nano* **2022**, *16* (2), 2640-2650.
367. Wu, F.; Zu, Y.; Weng, W.; Yang, Y.; Hu, J.; Mao, Y.; Shao, C.; Xiao, J., Multifunctional inverse opal film as a responsive drug carrier for spinal cord injury repair. *Chemical Engineering Journal* **2022**, *436*, 135256.
368. Zhang, Z.; Wang, Y.; Chen, Z.; Xu, D.; Zhang, D.; Wang, F.; Zhao, Y., Tailoring conductive inverse opal films with anisotropic elliptical porous patterns for nerve cell orientation. *Journal of Nanobiotechnology* **2022**, *20* (1), 117.
369. Weng, W.; Chi, J.; Wang, X.; Shi, K.; Ye, F.; Zhao, Y., Ellipsoidal porous patch with anisotropic cell inducing ability for inhibiting skin scar formation. *Engineered Regeneration* **2022**, *3* (3), 262-269.
370. Wang, X.; Husson, S. M.; Qian, X.; Wickramasinghe, S. R., Inverse colloidal crystal microfiltration membranes. *Journal of Membrane Science* **2010**, *365* (1), 302-310.
371. Wang, X.; Husson, S. M.; Qian, X.; Wickramasinghe, S. R., Inverse colloidal crystal ultrafiltration membranes. *Separation and Purification Technology* **2012**, *93*, 33-41.
372. Yeo, S. J.; Choi, G. H.; Yoo, P. J., Multiscale-architected functional membranes utilizing inverse opal structures. *Journal of Materials Chemistry A* **2017**, *5* (33), 17111-17134.
373. Zydney, A. L.; Ho, C.-C., Effect of membrane morphology on system capacity during normal flow microfiltration. *Biotechnology and Bioengineering* **2003**, *83* (5), 537-543.
374. Kim, J.-H.; Kim, J.-H.; Choi, K.-H.; Yu, H. K.; Kim, J. H.; Lee, J. S.; Lee, S.-Y., Inverse Opal-Inspired, Nanoscaffold Battery Separators: A New Membrane Opportunity for High-Performance Energy Storage Systems. *Nano Letters* **2014**, *14* (8), 4438-4448.

375. Rhee, D. K.; Jung, B.; Kim, Y. H.; Yeo, S. J.; Choi, S.-J.; Rauf, A.; Han, S.; Yi, G.-R.; Lee, D.; Yoo, P. J., Particle-Nested Inverse Opal Structures as Hierarchically Structured Large-Scale Membranes with Tunable Separation Properties. *ACS Applied Materials & Interfaces* **2014**, *6* (13), 9950-9954.
376. Kim, Y. H.; Kang, H.; Park, S.; Park, A. R.; Lee, Y. M.; Rhee, D. K.; Han, S.; Chang, H.; Ryu, D. Y.; Yoo, P. J., Multiscale Porous Interconnected Nanocolander Network with Tunable Transport Properties. *Advanced Materials* **2014**, *26* (47), 7998-8003.
377. Umeda, G. A.; Chueh, W. C.; Noailles, L.; Haile, S. M.; Dunn, B. S., Inverse opal ceria–zirconia: architectural engineering for heterogeneous catalysis. *Energy & Environmental Science* **2008**, *1* (4), 484-486.
378. Collins, G.; Blömker, M.; Osiak, M.; Holmes, J. D.; Bredol, M.; O'Dwyer, C., Three-Dimensionally Ordered Hierarchically Porous Tin Dioxide Inverse Opals and Immobilization of Palladium Nanoparticles for Catalytic Applications. *Chemistry of Materials* **2013**, *25* (21), 4312-4320.
379. Lei, J.; Chen, B.; Lv, W.; Zhou, L.; Wang, L.; Liu, Y.; Zhang, J., Robust Photocatalytic H₂O₂ Production over Inverse Opal g-C₃N₄ with Carbon Vacancy under Visible Light. *ACS Sustainable Chemistry & Engineering* **2019**, *7* (19), 16467-16473.
380. Yiwen Chen, L. L., Quanlong Xu, Düren Tina, Jiajie Fan, Dekun Ma, Controllable Synthesis of g-C₃N₄ Inverse Opal Photocatalysts for Superior Hydrogen Evolution. *Acta Phys. -Chim. Sin.* **2021**, *37* (6), 2009080.
381. Temerov, F.; Ankudze, B.; Saarinen, J. J., TiO₂ inverse opal structures with facile decoration of precious metal nanoparticles for enhanced photocatalytic activity. *Materials Chemistry and Physics* **2020**, *242*, 122471.
382. Temerov, F.; Pham, K.; Juuti, P.; Mäkelä, J. M.; Grachova, E. V.; Kumar, S.; Eslava, S.; Saarinen, J. J., Silver-Decorated TiO₂ Inverse Opal Structure for Visible Light-Induced Photocatalytic Degradation of Organic Pollutants and Hydrogen Evolution. *ACS Applied Materials & Interfaces* **2020**, *12* (37), 41200-41210.
383. Yang, C.; Li, Q., ZnO inverse opals with deposited Ag nanoparticles: Fabrication, characterization and photocatalytic activity under visible light irradiation. *Journal of Photochemistry and Photobiology A: Chemistry* **2019**, *371*, 118-127.
384. Namigata, H.; Watanabe, K.; Okubo, S.; Hasegawa, M.; Suga, K.; Nagao, D., Double-Inverse-Opal-Structured Particle Assembly as a Novel Immobilized Photocatalytic Material. *Materials* **2021**, *14* (1).
385. Esmanski, A.; Ozin, G. A., Silicon Inverse-Opal-Based Macroporous Materials as Negative Electrodes for Lithium Ion Batteries. *Advanced Functional Materials* **2009**, *19* (12), 1999-2010.
386. Huang, X.; Chen, J.; Lu, Z.; Yu, H.; Yan, Q.; Hng, H. H., Carbon inverse opal entrapped with electrode active nanoparticles as high-performance anode for lithium-ion batteries. *Scientific Reports* **2013**, *3* (1), 2317.
387. Song, T.; Jeon, Y.; Samal, M.; Han, H.; Park, H.; Ha, J.; Yi, D. K.; Choi, J.-M.; Chang, H.; Choi, Y.-M.; Paik, U., A Ge inverse opal with porous walls as an anode for lithium ion batteries. *Energy & Environmental Science* **2012**, *5* (10), 9028-9033.
388. McNulty, D.; Geaney, H.; Buckley, D.; O'Dwyer, C., High capacity binder-free nanocrystalline GeO₂ inverse opal anodes for Li-ion batteries with long cycle life and stable cell voltage. *Nano Energy* **2018**, *43*, 11-21.
389. McNulty, D.; Geaney, H.; Carroll, E.; Garvey, S.; Lonergan, A.; O'Dwyer, C., The effect of particle size, morphology and C-rates on 3D structured Co₃O₄ inverse opal conversion mode anode materials. *Materials Research Express* **2017**, *4* (2), 025011.
390. Vu, A.; Stein, A., Multiconstituent Synthesis of LiFePO₄/C Composites with Hierarchical Porosity as Cathode Materials for Lithium Ion Batteries. *Chemistry of Materials* **2011**, *23* (13), 3237-3245.
391. Armstrong, E.; McNulty, D.; Geaney, H.; O'Dwyer, C., Electrodeposited Structurally Stable V₂O₅ Inverse Opal Networks as High Performance Thin Film Lithium Batteries. *ACS Applied Materials & Interfaces* **2015**, *7* (48), 27006-27015.
392. Jin, L.; Huang, X.; Zeng, G.; Wu, H.; Morbidelli, M., Conductive framework of inverse opal structure for sulfur cathode in lithium-sulfur batteries. *Scientific Reports* **2016**, *6* (1), 32800.
393. Sakamoto, J. S.; Dunn, B., Hierarchical battery electrodes based on inverted opal structures. *Journal of Materials Chemistry* **2002**, *12* (10), 2859-2861.
394. De Lauri, V.; Krumbein, L.; Hein, S.; Prifling, B.; Schmidt, V.; Danner, T.; Latz, A., Beneficial Effects of Three-Dimensional Structured Electrodes for the Fast Charging of Lithium-Ion Batteries. *ACS Applied Energy Materials* **2021**, *4* (12), 13847-13859.

395. Lui, G.; Li, G.; Wang, X.; Jiang, G.; Lin, E.; Fowler, M.; Yu, A.; Chen, Z., Flexible, three-dimensional ordered macroporous TiO₂ electrode with enhanced electrode–electrolyte interaction in high-power Li-ion batteries. *Nano Energy* **2016**, *24*, 72-77.
396. Zhou, M.; Xu, Y.; Wang, C.; Li, Q.; Xiang, J.; Liang, L.; Wu, M.; Zhao, H.; Lei, Y., Amorphous TiO₂ inverse opal anode for high-rate sodium ion batteries. *Nano Energy* **2017**, *31*, 514-524.
397. Kim, S.; Qu, S.; Zhang, R.; Braun, P. V., High Volumetric and Gravimetric Capacity Electrodeposited Mesoporous Sb₂O₃ Sodium Ion Battery Anodes. *Small* **2019**, *15* (23), 1900258.
398. Liu, Y.; Shi, J.; Su, M.; Gao, F.; Lu, Q., Constructing inverse opal antimony@carbon frameworks with multi-level porosity towards high performance sodium storage. *Journal of Alloys and Compounds* **2022**, *914*, 165335.
399. Lee, K. T.; Lytle, J. C.; Ergang, N. S.; Oh, S. M.; Stein, A., Synthesis and Rate Performance of Monolithic Macroporous Carbon Electrodes for Lithium-Ion Secondary Batteries. *Advanced Functional Materials* **2005**, *15* (4), 547-556.
400. Kang, D.-Y.; Kim, S.-O.; Chae, Y. J.; Lee, J. K.; Moon, J. H., Particulate Inverse Opal Carbon Electrodes for Lithium-Ion Batteries. *Langmuir* **2013**, *29* (4), 1192-1198.
401. McNulty, D.; Geaney, H.; Ramasse, Q.; O'Dwyer, C., Long Cycle Life, Highly Ordered SnO₂/GeO₂ Nanocomposite Inverse Opal Anode Materials for Li-Ion Batteries. *Advanced Functional Materials* **2020**, *30* (51), 2005073.
402. Ren, H.; Zhao, J.; Yang, L.; Liang, Q.; Madhavi, S.; Yan, Q., Inverse opal manganese dioxide constructed by few-layered ultrathin nanosheets as high-performance cathodes for aqueous zinc-ion batteries. *Nano Research* **2019**, *12* (6), 1347-1353.
403. Zhang, R.; Fang, T.; Ni, L.; Zhu, Y.; Shen, Y.; Xie, A.; Lao, L., SnO₂/Bi₂O₃/NF heterojunction with ordered macro/meso-pore structure as an advanced binder-free anode for lithium ion batteries. *Journal of Electroanalytical Chemistry* **2022**, *907*, 115894.
404. Li, D.; Zhang, W.; Sun, R.; Yong, H.-T.-H.; Chen, G.; Fan, X.; Gou, L.; Mao, Y.; Zhao, K.; Tian, M., Soft-template construction of three-dimensionally ordered inverse opal structure from Li₂FeSiO₄/C composite nanofibers for high-rate lithium-ion batteries. *Nanoscale* **2016**, *8* (24), 12202-12214.
405. Liu, H.; Cho, H.-M.; Meng, Y. S.; Li, Q., Engineering Three-Dimensionally Electrodeposited Si-on-Ni Inverse Opal Structure for High Volumetric Capacity Li-Ion Microbattery Anode. *ACS Applied Materials & Interfaces* **2014**, *6* (12), 9842-9849.
406. McNulty, D.; Geaney, H.; O'Dwyer, C., Carbon-Coated Honeycomb Ni-Mn-Co-O Inverse Opal: A High Capacity Ternary Transition Metal Oxide Anode for Li-ion Batteries. *Scientific Reports* **2017**, *7* (1), 42263.
407. Liang, Z.; Zheng, G.; Li, W.; Seh, Z. W.; Yao, H.; Yan, K.; Kong, D.; Cui, Y., Sulfur Cathodes with Hydrogen Reduced Titanium Dioxide Inverse Opal Structure. *ACS Nano* **2014**, *8* (5), 5249-5256.
408. Li, Z.; Xiao, M.; Liu, Y.-F.; Gao, H.-H.; Braun, P. V., Three-dimensional mesoporous binder-free nickel-based TiO₂/RGO lithium-ion battery negative electrodes with enhanced volumetric capacity. *Ceramics International* **2021**, *47* (15), 21381-21387.
409. Jeong, J.-H.; Kim, K.-H.; Jung, D.-W.; Kim, K.; Lee, S.-M.; Oh, E.-S., High-performance characteristics of silicon inverse opal synthesized by the simple magnesium reduction as anodes for lithium-ion batteries. *Journal of Power Sources* **2015**, *300*, 182-189.
410. McNulty, D.; Landgraf, V.; Trabesinger, S., The importance of sulfur host structural preservation for lithium–sulfur battery performance. *Journal of Materials Chemistry A* **2020**, *8* (48), 26085-26097.
411. Zhang, Y.; Qiu, W.; Zhao, Y.; Wang, Y.; Bakenov, Z.; Wang, X., Ultra-fine zinc oxide nanocrystals decorated three-dimensional macroporous polypyrrole inverse opal as efficient sulfur hosts for lithium/sulfur batteries. *Chemical Engineering Journal* **2019**, *375*, 122055.
412. Yang, Y.; Ohnouteck, L.; Ajmal, S.; Zheng, X.; Feng, Y.; Li, K.; Wang, T.; Deng, Y.; Liu, Y.; Xu, D.; Valev, V. K.; Zhang, L., “Hot edges” in an inverse opal structure enable efficient CO₂ electrochemical reduction and sensitive in situ Raman characterization. *Journal of Materials Chemistry A* **2019**, *7* (19), 11836-11846.
413. Glazer, M. P. B.; Cho, J.; Almer, J.; Okasinski, J.; Braun, P. V.; Dunand, D. C., In Operando Strain Measurement of Bicontinuous Silicon-Coated Nickel Inverse Opal Anodes for Li-Ion Batteries. *Advanced Energy Materials* **2015**, *5* (14), 1500466.

414. Glazer, M. P. B.; Wang, J.; Cho, J.; Almer, J. D.; Okasinski, J. S.; Braun, P. V.; Dunand, D. C., In operando X-ray diffraction strain measurement in Ni₃Sn₂ – Coated inverse opal nanoscaffold anodes for Li-ion batteries. *Journal of Power Sources* **2017**, *367*, 80-89.
415. Xu, H.; Lu, Y. F.; Xiang, J. X.; Zhang, M. K.; Zhao, Y. J.; Xie, Z. Y.; Gu, Z. Z., A multifunctional wearable sensor based on a graphene/inverse opal cellulose film for simultaneous, in situ monitoring of human motion and sweat. *Nanoscale* **2018**, *10* (4), 2090-2098.
416. Harks, P. P. R. M. L.; Mulder, F. M.; Notten, P. H. L., In situ methods for Li-ion battery research: A review of recent developments. *Journal of Power Sources* **2015**, *288*, 92-105.
417. Liu, D.; Shadik, Z.; Lin, R.; Qian, K.; Li, H.; Li, K.; Wang, S.; Yu, Q.; Liu, M.; Ganapathy, S.; Qin, X.; Yang, Q.-H.; Wagemaker, M.; Kang, F.; Yang, X.-Q.; Li, B., Review of Recent Development of In Situ/Operando Characterization Techniques for Lithium Battery Research. *Advanced Materials* **2019**, *31* (28), 1806620.
418. Phillips, K. R.; Shirman, T.; Shirman, E.; Shneidman, A. V.; Kay, T. M.; Aizenberg, J., Nanocrystalline Precursors for the Co-Assembly of Crack-Free Metal Oxide Inverse Opals. *Advanced Materials* **2018**, *30* (19), 1706329.
419. Jiang, Z.; Pikul, J. H., Centimetre-scale crack-free self-assembly for ultra-high tensile strength metallic nanolattices. *Nature Materials* **2021**, *20* (11), 1512-1518.
420. Zhou, C.; Qi, Y.; Zhang, S.; Niu, W.; Wu, S.; Ma, W.; Tang, B., Fast water-response double-inverse opal films with brilliant structural color. *Chemical Engineering Journal* **2021**, *426*, 131213.
421. Zhou, C.; Qi, Y.; Zhang, S.; Niu, W.; Wu, S.; Ma, W.; Tang, B., Lotus Seedpod Inspiration: Particle-Nested Double-Inverse Opal Films with Fast and Reversible Structural Color Switching for Information Security. *ACS Applied Materials & Interfaces* **2021**, *13* (22), 26384-26393.
422. Kubrin, R.; Lee, H. S.; Zierold, R.; Yu. Petrov, A.; Janssen, R.; Nielsch, K.; Eich, M.; Schneider, G. A., Stacking of Ceramic Inverse Opals with Different Lattice Constants. *Journal of the American Ceramic Society* **2012**, *95* (7), 2226-2235.
423. Eftekhari, E.; Broisson, P.; Aravindakshan, N.; Wu, Z.; Cole, I. S.; Li, X.; Zhao, D.; Li, Q., Sandwich-structured TiO₂ inverse opal circulates slow photons for tremendous improvement in solar energy conversion efficiency. *Journal of Materials Chemistry A* **2017**, *5* (25), 12803-12810.
424. Cai, Z.; Liu, Y. J.; Teng, J.; Lu, X., Fabrication of Large Domain Crack-Free Colloidal Crystal Heterostructures with Superposition Bandgaps Using Hydrophobic Polystyrene Spheres. *ACS Applied Materials & Interfaces* **2012**, *4* (10), 5562-5569.
425. Zhou, C.; Qi, Y.; Zhang, S.; Niu, W.; Wu, S.; Ma, W.; Tang, B., Bilayer Heterostructure Photonic Crystal Composed of Hollow Silica and Silica Sphere Arrays for Information Encryption. *Langmuir* **2020**, *36* (5), 1379-1385.